https://doi.org/10.15388/vu.thesis.903
https://orcid.org/0000-0002-5349-4679

VILNIUS UNIVERSITY
CENTER FOR PHYSICAL SCIENCES AND TECHNOLOGY

Matas Plūkys

Microchip Lasers with Spatial- and Polarization-Filtering Metamirrors

DOCTORAL DISSERTATION

Natural Sciences,
Physics (N 002)

VILNIUS 2026

The dissertation was prepared between 2020 and 2026 at Vilnius University. The research was supported by Research Council of Lithuania.

Academic supervisor:
Prof. Dr. Kęstutis Staliūnas (Vilnius University and Polytechnic University of Catalonia, Natural Sciences, Physics – N 002).

Consultant:
Dr. Darius Gailevičius (Vilnius University, Natural Sciences, Physics – N 002).

Dissertation Defence Panel:
Chair – **Prof. Dr. Audrius Dubietis** (Vilnius University, Natural Sciences, Physics – N 002).
Members:
Dr. Vygandas Jarutis (Vilnius University, Natural Sciences, Physics – N 002).
Dr. Andrejus Michailovas (Center for Physical Sciences and Technology, Natural Sciences, Physics – N 002).
Dr. Gediminas Račiukaitis (Center for Physical Sciences and Technology, Natural Sciences, Physics – N 002).
Dr. Ramon Herrero Simon (Polytechnic University of Catalonia, Spain, Natural Sciences, Physics – N 002).

The dissertation shall be defended at a public meeting of the Dissertation Defence Panel at 3:00 p.m. on the 17th of April 2026, in Auditorium No. 306, Laser Research Center, Faculty of Physics, Vilnius University. Address: Sauletekio ave. 10, LT-10223 Vilnius, Lithuania. tel: +370 5 236 6050 ; e-mail: ff@ff.vu.lt

https://doi.org/10.15388/vu.thesis.903
https://orcid.org/0000-0002-5349-4679

VILNIAUS UNIVERSITETAS
FIZINIŲ IR TECHNOLOGIJOS MOKSLŲ CENTRAS

Matas Plūkys

Mikrolustiniai lazeriai su erdvinio ir poliarizacinio filtravimo meta-veidrodžiais

DAKTARO DISERTACIJA

Gamtos mokslai,
Fizika (N 002)

VILNIUS 2026

Disertacija rengta 2020–2026 metais Vilniaus universitete. Mokslinius tyrimus rėmė Lietuvos mokslo taryba.

Mokslinis vadovas:
Prof. dr. Kęstutis Staliūnas (Vilniaus universitetas ir Katalonijos politechnikos universitetas, gamtos mokslai, fizika – N 002).

Mokslinis konsultantas:
Dr. Darius Gailevičius (Vilniaus universitetas, gamtos mokslai, fizika – N 002).

Gynimo taryba:
Pirmininkas – **Prof. dr. Audrius Dubietis** (Vilniaus universitetas, gamtos mokslai, fizika – N 002).
Nariai:
Dr. Vygandas Jarutis (Vilniaus universitetas, gamtos mokslai, fizika – N 002).
Dr. Andrejus Michailovas (Fizinių ir technologijos mokslų centras, gamtos mokslai, fizika – N 002).
Dr. Gediminas Račiukaitis (Fizinių ir technologijos mokslų centras, gamtos mokslai, fizika – N 002).
Dr. Ramon Herrero Simon (Katalonijos politechnikos universitetas, Ispanija, gamtos mokslai, fizika – N 002).

Disertacija ginama viešame gynimo tarybos posėdyje 2026 m. balandžio 17 d. 15:00 val. Vilniaus universiteto, Fizikos fakulteto, Lazerinių tyrimų centro auditorijoje Nr. 306. Addresas: saulėtekio al. 10, LT-10223 Vilnius, Lietuva. tel: +370 5 236 6050; el. paštas: ff@ff.vu.lt

Dedication

To my wife Marta and my daughter Mara, I am grateful for their love, patience, and the daily teamwork with which we faced every challenge.

Acknowledgment

I would like to thank my academic supervisor, Prof. Kęstutis Staliūnas, for his constant support throughout this five-year journey.

This work would not have been possible without the photonic crystals fabricated by Lina Grinevičiūtė and Julijanija Nikitina. I wish them both success as they continue advancing the technology.

I would like to thank my advisor, Darius Gailevičius, for his openness and willingness to engage in a wide range of discussions.

I would like to thank my colleagues Aurimas and Tadas for giving me the opportunity to work with a flexible schedule at Optogama while simultaneously pursuing my scientific research.

I would like to thank Justinas Girskis and Rokas Steponavičius for their assistance with mechanical component production. I am also grateful to Rytis Šalaševičius for partially substituting me in the office. Finally, I sincerely thank the entire Optogama team for their support and for maintaining a positive working atmosphere.

Abbreviations

AFM	Angular Filtering Mirror
AM	Active Material
AOI	Angle of Incidence
AR	Anti-Reflective
BAP	Brewster Angle Polarizer
BPA	Beam Propagation Analyzer
BW	Beam Width
CCD	Charge-Coupled Device
CL	Collimating Lens
CMOS	Complementary Metal–Oxide–Semiconductor
CW	Continuous Wave
FL	Focusing Lens
FO	Focusing Optics
HR	High Reflective
HT	High Transmissive
HWWP	Half Wavelength Wave Plate
IT	Initial Transmission
LADAR	Laser Detection and Ranging
LiDAR	Light Detection and Ranging
LM	Longitudinal Mode
MBE	Maxwell–Bloch Equations
McL	Microchip Laser
MeM	Metal Mirror
MM	Meta-Mirror
Nd:YAG	Neodymium-doped Yttrium Aluminum Garnet
OC	Output Coupler
PD	Pumping Diode
PhC	Photonic Crystal
PM	Power Meter
PRF	Pump Rejection Filter
Q	Quality Factor
SVEA	Slowly Varying Amplitude Approximation
TM	Transverse Mode
M^2	Beam Quality Factor

Contents

1 Introduction **10**
Background . . . 12
Dissertation Objective . . . 12
Scientific Novelty and Practical Value . . . 13
Defensive Statements . . . 14
Approbation . . . 14
Author's Personal and Co-authors' Contribution . . . 16

2 Literature review **17**
2.1 Origin and Context of Microchip Lasers . . . 17
2.1.1 Pulsed Operation . . . 19
2.1.2 Material Properties and Pumping . . . 20
2.1.3 Applications . . . 26
2.2 Transverse Modes in McLs . . . 28
2.3 Laser Beam Quality Factor M^2 . . . 31
2.4 Spatial Filtering in McLs . . . 33
2.5 Polarization Filtering in McLs . . . 35

3 Results **36**
3.1 Transverse Modes and Beam Quality in McLs . . . 36
3.1.1 Linear field equation in 2D . . . 37
3.1.2 Eigenfrequencies of Linear field Equation in 2D . . . 41
3.1.3 Mode shapes and beam quality factors M^2 . . . 44
3.1.4 Composite beam quality factor M^2 . . . 46
3.1.5 Summary . . . 49
3.2 Spatial Filtering in Photonic Crystal McL . . . 49
3.2.1 Angular filtering mirror . . . 51
3.2.2 Experiment . . . 53
3.2.3 Output beam profile Dynamics in Far and Near Field . . . 58
3.2.4 Numerical Simulations . . . 61
3.2.5 Summary . . . 63

3.3 Polarization Filtering in Nd:YAG Microchip Laser 64
3.3.1 Polarizing Meta-Mirror 66
3.3.2 Laser Parameter Experimental Investigation 68
3.3.3 Discussion 73
3.3.4 Summary 76

4 Research Methodology **78**
4.1 Experimental methods 78
4.1.1 Pumping Configurations 78
4.1.2 Active Medium Investigation 83
4.1.3 Laser power measurement 85
4.1.4 Masurement of Beam Quality Factor M^2 86
4.1.5 Laser Beam Brightness Evaluation 90
4.1.6 Laser beam profile estimation in near and far fields 91
4.1.7 Laser Polarization Extinction Ratio Estimation . . 92
4.1.8 Estimation of Cavity Losses 94
4.1.9 Estimation of the Optimal Output Coupler Reflectivity 96
4.1.10 Thermal Lens Estimation 99
4.1.11 Angular Filtering Mirror Investigation 101
4.2 Analytical methods 102
4.2.1 Paraxial Approximation 103
4.2.2 Thermal Lens Shapes in Longitudinally Pumped McL Crystal 104
4.2.3 Gaussian-Laguerre Beams 105
4.2.4 Macroscopic Maxwell–Bloch equations for McL with AFM 107
4.2.5 Linear field equation 108
4.3 Numerical methods 109
4.3.1 Evaluation of Transverse Mode Eigenfrequencies . 109
4.3.2 Beam quality M^2 of single modes calculation in McL 111

Main Results **112**

Conclusions **114**

Appendix **116**

Bibliography **133**

Santrauka **154**

Cirriculum Vitae **169**

Chapter 1

Introduction

Lasers occupy a unique position among light sources due to their ability to generate coherent radiation through stimulated emission. Photons may occupy the same quantum state, enabling the buildup of intense, phase-synchronized electromagnetic fields. Although the electromagnetic field consists of photons, the laser device itself is built from matter whose thermal, mechanical, and optical properties impose practical limits on achievable lasing power, peak intensity, beam quality, brightness, polarization contrast. These constraints become particularly important in compact solid-state resonators, where optical fields are confined within millimeter-scale media.

Among compact systems, *microchip lasers* represent one of the most successful realizations of laser miniaturization. Introduced in 1989 by Zayhowski and Mooradian [1], the microchip laser is defined by a monolithic flat–flat cavity in which both mirrors are deposited directly onto the gain medium. This configuration provides excellent mechanical stability, low threshold, and compatibility with mass production. As a result, microchip lasers have become widely used across industrial, communication, sensing, medical, and instrumentation applications [2, 3].

Despite these advantages, the miniature geometry introduces specific challenges. The transverse mode structure and beam quality factor M^2 are shaped by the interplay of gain guiding, thermally induced refractive-index gradients, birefringence and stress. These factors frequently lead to multimode operation and limit brightness and polarization contrast ratio,

particularly at elevated pump powers. Conventional methods for improving spatial or polarization performance—intracavity apertures, curved mirrors, or bulk polarizers—often compromise compactness, alignment stability, or manufacturability.

Recent advances in *photonic crystals* and *metasurfaces* provide an alternative approach for intracavity mode control. Sub-wavelength periodic structures can be engineered to exhibit angle-selective, polarization-selective, or spatially selective reflectance. When implemented as cavity mirrors, such elements introduce novel intracavity filtering mechanisms without enlarging the resonator footprint. These concepts have only recently begun to be explored in solid-state microchip resonators, and their integration opens new opportunities for tailoring mode selection and improving beam quality in ultra-compact lasers.

The present dissertation explores microchip lasers incorporating *photonic-crystal-based cavity mirrors* and investigates how spatial and polarization filtering within the resonator can improve beam characteristics. The research is based on two components:

1. **Experimental demonstrations** of brightness enhancement, improved beam quality, and increased polarization contrast through intracavity spatial and polarization filtering, as reported in the author's publications [4, 5].

2. **Development of a practical theoretical model** based on two-dimensional linear field equations, enabling the estimation of modal content and beam-quality factors M^2, together with **experimental validation of the model** [6].

Integrating metamirrors into microchip laser cavities reveals new regimes of intracavity spatial and polarization control, enabling improvements unattainable in traditional flat–flat monolithic designs. The results presented in this thesis contribute to understanding mode formation in microchip geometries and support the development of next-generation compact laser sources with enhanced brightness, beam quality, and

polarization performance for applications in sensing, metrology, communications, integrated photonics and others.

Background

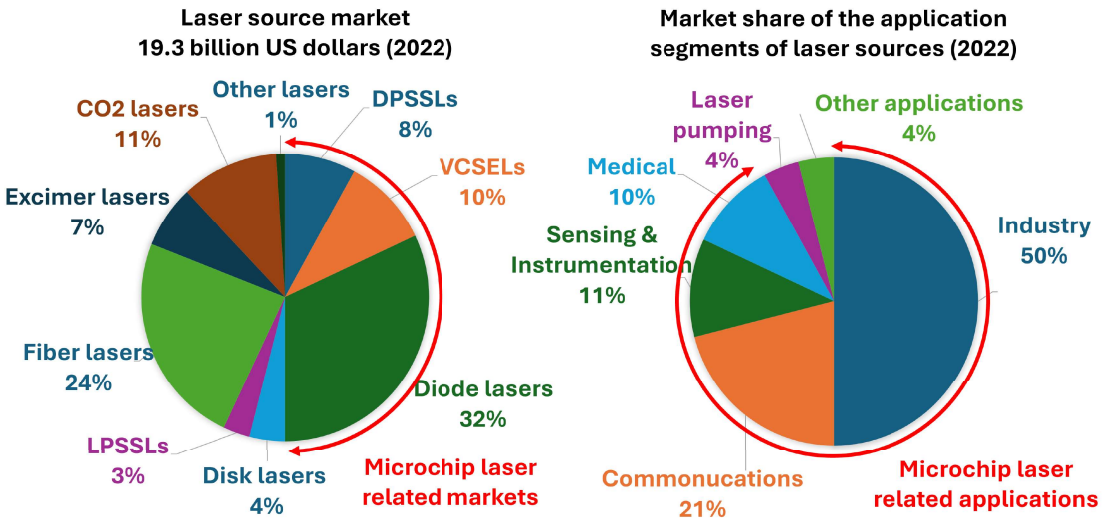


Figure 1.1: Laser source market size and market share of the application segments in 2022 year [3].

Microchip lasers first emerged in 1989 [1]. That same year, the global laser source market was valued at approximately 720 million US dollars [7]. Now, more than three decades later, the market has expanded to 19.3 billion US dollars [3]. Half of this market belongs to diode pumped solid state lasers (DPSSL), diode lasers (DL) and vertical cavity surface emitting lasers (VCSEL). As originally defined, microchip lasers belong to the subcategory of DPSSL [1]. Diode lasers (DLs) and vertical-cavity surface-emitting lasers (VCSELs) share similar cavity geometries and are closely related to microchip laser physics—often even referred to as microlasers or microchip lasers. Microchip lasers are applied in areas of industry, communication, sensing, instrumentation and medicine, whereas these applications comprise the biggest part of the today's laser source market (see Fig. 1.1).

Dissertation Objective

Enhance the capabilities and broaden the application scope of microchip lasers by integrating advanced photonic crystal designs into the laser cavity. This approach aims to improve key output parameters, including brightness, beam quality factor (M^2), and polarization contrast ratio. Furthermore, develop a practical theoretical model for estimating the beam quality factor (M^2) of output beam and for analyzing its modal composition.

Dissertation Scientific Tasks

1. Experimentally demonstrate the enhancement of brightness and beam quality in the output beam of a microchip laser through the incorporation of a photonic crystal within the laser cavity.

2. Demonstrate experimentally the enhancement of the polarization contrast in the output beam of a microchip laser achieved through the integration of a photonic crystal within the laser cavity.

3. Develop a practical theoretical model for estimating the beam quality factor (M^2) and modal composition in microchip lasers, and validate the model through experimental measurements.

Scientific Novelty and Practical Value

The research conducted in this thesis introduces novel design of microchip laser cavity with photonic crystals, which leads to improved output beam spatial and polarization properties. This improvement can be directly applied to microchip lasers used in very important areas such as military, medical, industry, space , etc. Additionally, the novel laser design contains novel physical dynamics, which are investigated experimentally and theoretically. The scientific novelty and practical value can be summarized in following statements:

- First time investigated microchip laser cavity with photonic crystal working as output coupler and spatially filtering the laser beam leading to improved beam quality and brightness.
- First time investigated microchip laser cavity with photonic crystal working as output coupler and filtering the polarization at high pump powers leading to improved polarization contrast, beam quality and brightness while comparing with polarization enhancement technique using linearly polarized incident pump.
- Developed novel theoretical practical approach to estimate the beam quality factor M^2 and modal content of microchip laser output beam.

Defensive Statements

1. I claim that replacing a conventional plane-mirror outcoupler with an Angular-Filtering Mirror (AFM) in a 2.1 mm-long Nd:YAG microchip laser cavity operating in the CW regime leads to enhanced beam quality and brightness in the investigated 1.5–11.7 W pump-power range. These changes represent a beneficial improvement of microchip laser performance.
2. I claim that replacing a conventional plane-mirror outcoupler with a Polarizing Meta-Mirror (MM) in a 5 mm-long Nd:YAG microchip laser cavity operating in the CW regime leads to enhanced polarization contrast across the investigated 1–3.5 W absorbed pump-power range. These changes represent a beneficial improvement of microchip laser performance.
3. I claim that the developed two-dimensional linear-field model enables quantitative prediction of the beam-quality factor M^2 in the experimentally investigated Nd:YAG microchip lasers with 5 mm and 15 mm-long cavities operating in the CW regime, as confirmed by agreement between theory and experiment.

Approbation

Scientific publications directly related to Dissertation subject:

1. **Matas Plukys**, Eugenijus Gaizauskas, Darius Gailevicius, and Kestutis Staliunas, "Transverse modes and beam spatial quality in microchip lasers," *Physical Review A*, vol.107, p. 043505, 2023,

   https://link.aps.org/doi/10.1103/PhysRevA.107.043505

2. **Matas Plukys**, Lina Grineviciute, Julianija Nikitina, Darius Gailevicius, and Kestutis Staliunas, "Enhancement of brightness in microchip laser with angular filtering mirrors," *Optics & Laser Technology*, vol.181, Part C, p. 111904, 2025,

   https://doi.org/10.1016/j.optlastec.2024.111904

3. **Matas Plukys**, Lina Grineviciute, Julianija Nikitina, Darius Gailevicius, and Kestutis Staliunas, "Polarization enhancement in Nd:YAG microchip laser with Meta-Mirror output coupler," *Optics Letters*, vol. 50, pp. 4666–4669, 2025.
   https://doi.org/10.1364/OL.566958
   *(Selected as an **Editor's Pick**)*

Conference presentations:

1. **Matas Plukys**, Darius Gailevicius, Lina Grineviciute, Julianija Nikitina, and Kestutis Staliunas, *"Fano-structure as output coupling mirror of microchip laser doubles its brightness,"* SPIE Photonics Europe, Strasbourg, France, 2024 (Oral presentation),

   https://doi.org/10.1117/12.3016701

2. **Matas Plukys**, Eugenijus Gaizauskas, Darius Gailevicius, and Kestutis Staliunas, *"Modes in microchip lasers,"* SPIE Photonics Europe, Strasbourg, France, 2022 (Oral presentation),

   https://doi.org/10.1117/12.2621111

3. **Matas Plukys**, Eugenijus Gaizauskas, Darius Gailevicius, and Kestutis Staliunas, *"Modos mikrolustiniame lazeryje,"* Nacionalinė fizikos konferencija, Vilnius, Lietuva, 2021 (Oral presentation)

4. **Matas Plukys**, Eugenijus Gaizauskas, Darius Gailevicius, and Kestutis Staliunas, *"Transverse Modes and Beam Spatial Quality in Microchip Lasers,"* Humboldt Kolleg on Synthetic Quantum Matter, Vilnius, Lithuania, 2023 (Poster)

Author's Personal and Co-authors' Contribution

Author designed and constructed the experiment setup, planned and performed the experiments, processed experimental data, made the experimental data analysis and took participation in theoretical simulations and conceptualization.

Dissertation academic supervisor Prof. Dr. Kestutis Staliunas suggested the thesis concept, constantly participated in experimental data analysis, suggested innovative ideas, methods, insights and supported by numerical calculations. Also, constantly motivated author for consistent work.

Dr. Lina Grineviciute and Julianija Nikitina manufactured the photonic crystals used in authors experiments.

Advisor Dr. Darius Gailevicius actively participated in experimental data analysis and suggested insights.

All publication coauthors participated with notes and insights.

Chapter 2

Literature review

2.1 Origin and Context of Microchip Lasers

The concept of the microchip laser (McL) was first introduced by Zayhowski and Mooradian in 1989 [1], nearly three decades after the demonstration of the first laser [8]. The original idea was to realize a miniature, monolithic, flat–flat solid-state resonator, in which both cavity mirrors are planar and directly coated onto the active laser medium, forming a compact monolithic resonator. The original McL designs operating in the continuous-wave (CW) and pulsed regimes [1, 9] are illustrated in Fig. 2.1(a, b) accordingly.

This flat–flat monolithic concept opened a new field of technological innovation. Firstly, no additional space is required for curved mirrors, enabling the realization of laser micro-cavities [2]. Secondly, the fabrication cost is significantly reduced, as multiple McLs can be cut from a single wafer with planar surfaces [2, 9]. Thirdly, several flat-surface optical elements—such as passive Q-switch absorbers [10, 11], second-harmonic (SH) generation crystals [12–15], and end-caps [16, p.411], [17]—can be integrated into a single compact monolithic cavity [2, 9]. Finally, the monolithic design is highly resistant to optical misalignment [2]. An illustration of such a combined monolithic cavity incorporating a saturable absorber is presented in Fig. 2.1(b).

The short cavity of a McL allows single-longitudinal-mode oper-

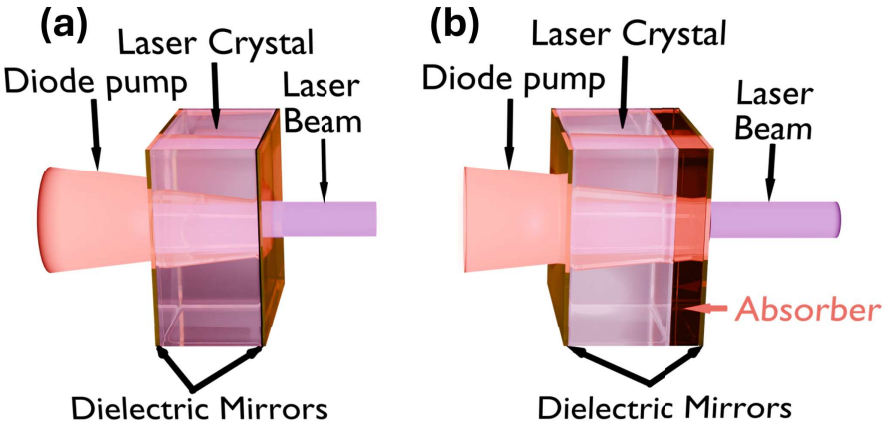


Figure 2.1: (a) Schematic of the McL operating in the continuous-wave (CW) regime, as introduced in [1, 9]. (b) Monolithic cavity configuration incorporating a saturable absorber for passively Q-switched operation, following the designs reported in [11, 18].

ation [1]. Depending on the resonator length—and consequently on the separation between longitudinal modes—frequency tuning can be achieved in the gigahertz (GHz) range [16, p.274], [9], or even extended to the terahertz (THz) range using frequency-doubling techniques [19]. Short McL resonators support relatively wide tuning ranges because their longitudinal modes are widely spaced. The frequency separation between adjacent longitudinal modes is given by

$$\Delta\nu = \frac{c}{2\,n\,L}, \tag{2.1}$$

where c is the speed of light, n is the refractive index, and L is the cavity length [16, p. 256]. For example, a 2 mm long monolithic Nd:YAG resonator exhibits a mode spacing of approximately 41.2 GHz. In McLs, frequency tuning can be achieved through thermal expansion or by applying mechanical stress to the crystal [16, p. 274]. Additional tuning methods include inserting an electro-optic modulator inside the cavity [9] or mechanically adjusting the cavity length.

2.1.1 Pulsed Operation

McLs can serve as compact sources of short optical pulses in the passively Q-switched regime [18], typically achieving sub-nanosecond pulse durations [11, 20–27]. The shortest reported pulse durations reach the range of several tens of picoseconds [28–31]. In such configurations, a saturable absorber is integrated within the microchip cavity, often directly bonded to the gain medium by diffusion [18] or by liquid-phase epitaxy [2], thereby preserving the monolithic and compact nature of the resonator. Typical pulse energies range from a few nanojoules [28, 29] at megahertz-level repetition rates to several tens or hundreds of microjoules [20, 22, 32, 33] at kilohertz-level repetition rates. Pulse energies reaching the millijoule range have been demonstrated primarily at low repetition rates [34]. The corresponding peak powers span from several kilowatts [29, 32, 33, 35] up to tens of megawatts [34].

In a passively Q-switched regime, the pulse duration scales approximately linearly with the cavity round-trip time [16, p. 491], such that shorter cavities produce correspondingly shorter pulses [36]. The temporal evolution and shape of a Q-switched laser pulse can be quantitatively described by a system of three coupled rate equations [36], governing the population inversion density in the gain medium, the photon density within the resonator, and the ground-state population of the saturable absorber [37]. The key parameters determining the pulse duration and pulse energy include the emission cross-section of the active material, the cavity photon lifetime, and the absorption cross-section of the saturable absorber [38]. Theoretical models for pulse duration and energy [13] have been extensively validated by experimental data [36].

A well-known limitation of passively Q-switched operation is the relatively large pulse-to-pulse timing jitter. In passively Q-switched McLs, this jitter is typically below 0.5% of the inter-pulse period [11] and ranges from hundreds of nanoseconds [39] to several microseconds [40]. The pulse-to-pulse timing jitter in McLs can be reduced using an external bleaching technique [39], in which the saturable absorber is bleached

by an additional diode pulse applied from the side. Alternatively, the timing jitter can be reduced by employing a narrow-linewidth, fiber Bragg grating (FBG)-stabilized laser diode as the pump source [41].

It should be noted that pulsed operation can also be achieved *without* a saturable absorber, relying solely on the three-level laser medium, where intrinsic reabsorption leads to self-Q-switching behavior [42–46]. Such lasers are capable of generating nanosecond pulses at gigahertz-level repetition rates with microjoule-level energies [42].

2.1.2 Material Properties and Pumping

Most commonly used active materials in McLs include Nd:YAG [22, 32, 34, 35, 47], Nd:YVO_4 [21, 28, 29], Nd:YLF [48], Yb:YAG [20, 33, 49–51], Yb:YLF [52], Yb:KGW [42, 53], Pr:YLF [54], Er:Yb:glass [23], Tm:YLF [44, 55], Tm:YAP [56, 57], and Tm:YAG [58]. The key gain-medium parameters relevant to McL design include the emission and absorption cross-sections and spectral linewidths, fluorescence lifetime, thermal conductivity, and birefringence [16, pp. 38–97],[59, pp. 286–291]. These properties are summarized in Table 2.1.

A larger emission cross section, as in Nd:YVO_4 or Nd:YAG, reduces the population inversion required to reach the lasing threshold, leading to shorter pumping times in the passively Q-switched regime. It also results in faster inversion depletion and, consequently, shorter pulse durations [36]. However, materials with high emission cross-sections generally possess reduced energy-storage capability and may exhibit increased beam quality factors M^2 due to the correspondingly stronger gain [6].

A larger absorption cross-section (e.g. in Nd:YVO_4 or Nd:YLF) reduces the population required to absorb a given amount of pump power, providing stronger absorption per unit length and enabling the use of shorter or less doped crystals [60], [16, p. 71]. This is particularly advantageous in longitudinally pumped microchip geometries, where a shorter crystal directly enables a shorter cavity. In many materials, however, the maximum practical dopant concentration is limited (e.g. crystalline Nd:YAG is typically restricted to $< 1\%$ [60]) because excessive

Table 2.1: Laser material properties [16, pp. 38–97]. The table summarizes the emission and absorption cross-sections (σ_e, σ_a), fluorescence lifetime (τ_f), thermal conductivity (κ) and other parameters for commonly used solid-state laser gain media in McL.

Laser material	σ_e ($\times 10^{-20}$ cm^2)	σ_a ($\times 10^{-20}$ cm^2)	τ_f (µs)	Pump band (nm)	Emission band (nm)	Number of levels	κ (W m^{-1} K^{-1})	Birefringence
Nd:YAG	28	1.0	230	808	1064	4	14.0	isotropic
Nd:YVO_4	250	30	90	808	1064	4	5.0	uniaxial
Nd:YLF	12	5.0	480	808	1047/1053	4	5.0	uniaxial
Yb:YAG	2.0	1.0	1200	940/970	1030	3	14.0	isotropic
Yb:YLF	0.8	0.5	1000	940–980	1020–1050	3	5.0	uniaxial
Yb:KGW	1.0	0.5	1000	980	1020–1040	3	2.5	biaxial
Pr:YLF	0.5	0.5	100	444	520/605/639	3	5.0	uniaxial
Er:Yb:glass	0.5	0.1	7000	975–980	1530–1560	3	1.0	amorphous
Tm:YLF	1.0	1.0	800	790	1860–2010	3	5.0	uniaxial
Tm:YAP	1.0	1.0	800	790	1900–2010	3	10.5	biaxial
Tm:YAG	0.8	1.0	800	790–800	2010	3	14.0	isotropic

doping can induce lattice distortion and additional losses. Although Nd:YAG ceramics allow higher doping levels (2–4%) and higher absorption coefficients, this is accompanied by a shortened fluorescence lifetime and reduced quantum efficiency [61, 62], which limits the achievable stored energy in Q-switched operation. In such cases, the absorption cross-section becomes a determining factor for how much the cavity length can be reduced. Materials with larger absorption cross-sections often exhibit narrower absorption bandwidths, which may impose tighter requirements on the pump diode emission spectrum. Furthermore, when pump power is absorbed within a shorter distance, the resulting heat load becomes more localized, potentially increasing thermal gradients and the associated beam distortions [63].

A longer fluorescence lifetime (as in Er:Yb:glass, Yb:YAG, Yb:KGW, Tm:YLF) allows a larger amount of energy to be stored in the gain medium before stimulated emission depletes the inversion, which is particularly advantageous for pulsed lasers operating at low repetition rates and high pulse energies [16, p. 38]. An extended lifetime also reduces inversion losses due to spontaneous decay while the system approaches threshold, thereby lowering the lasing threshold and improving the overall energy-storage efficiency.

Efficient pumping requires that the central wavelength and spectral bandwidth of the laser material absorption cross-section be well matched to the central emission wavelength and spectral linewidth of available pump diodes [16, pp. 340–366]. The development of McLs has been closely linked to advances in AlGaAs and InGaAs laser-diode technology, whose emission wavelengths efficiently cover the dominant pump bands of Nd- and Yb-doped gain media. The available diode output power for McL pumping has increased from only a few hundred milliwatts in the early stages of development [64–68] to the kilowatt-level powers accessible today [34].

Such extreme pump powers are primarily applicable to longitudinally pumped unstable microchip resonators, which employ a large transverse mode area matched to a broad pump spot and are operated in quasi-CW regimes at low repetition rates under passive Q-switching. In these configurations, Nd:YAG ceramic McLs incorporating Cr:YAG saturable absorbers were pumped with 1.5 kW [69] and 700 W [70], generating pulse energies of 24 mJ and 18 mJ and peak powers of 50 MW and 27 MW, respectively.

High pump powers can also be employed in edge-pumped McL configurations, where the gain element is bonded to a heat sink in a geometry similar to the thin-disk concept. In such arrangements, Yb:YAG McLs were pumped with 946 W [71] and 997 W [72], delivering continuous-wave output powers of 300 W and 520 W, respectively.

In contrast, for stable CW end-pumped McLs employing smaller pump spots, the fracture limit of single-end-pumped Nd:YAG crystals becomes the dominant constraint. For a 1 % doped Nd:YAG crystal operating in the CW regime with a relatively large pump-spot diameter of approximately 2 mm, the maximum admissible pump power is estimated to be $\sim$50 W [73], limited by the tensile stress. The maximum tensile stress is directly proportional to the temperature difference between the crystal center and edge [74], which itself scales linearly with the absorption coefficient and decreases logarithmically with increasing pump-spot radius [75]. The critical temperature differences ΔT at which

fracture occurs were reported to be 241 K for Nd:YAG single crystals and 355 K for Nd:YAG ceramics [74].

For a pump-spot diameter of 380 μm, experimentally measured fracture pump powers were 14.9 W and 6.87 W for Nd:YAG ceramics doped with 2 % and 4 %, respectively [76]. By extrapolation, a 1 % doped Nd:YAG single crystal pumped with the same spot size is expected to withstand approximately 20 W of pump power, taking into account its roughly twofold lower absorption coefficient compared to 2 % doped ceramics and its approximately 1.5 times lower allowable temperature difference before fracture.

Further pump-power scaling has been demonstrated using cryogenic cooling in combination with composite monolithic YAG/Yb:YAG/Cr:YAG structures incorporating undoped YAG end caps to mitigate thermal stress at optical interfaces. Under these conditions, the pump power was increased up to 190 W [77] in quasi-CW operation with a large pump-spot diameter of 2 mm, yielding output pulse energies in the tens-of-millijoule range.

Pump radiation from a single emitter or an emitter array can be delivered to the microchip crystal either through free-space micro-optics or via optical fiber. Using fiber optics to deliver the diode output to the laser crystal has a number of advantages: the beam at the fiber output has a circular distribution and the ability to remove heat from the diode remote from the optical components of the laser is an attractive feature. Also the pump source can be replaced relatively easily without disturbing the alignment of the laser [16, p. 416]. Free-space coupling can be preferable in highly compact or mechanically rigid architectures.

McLs can be pumped either in pulsed mode [35] or in the continuous-wave (CW) regime [21, 28, 29, 32, 33], depending on the intended operating conditions and system architecture. Although several-millimeter-long crystals can still be pumped transversely, the much shorter cavities typical of McLs contain longitudinal pumping. Rosenkrantz [78] demonstrated the first end-pumped solid-state laser and showed that this configuration provides superior overlap between the pump radiation and the laser mode

Table 2.2: Passive Q-switch absorber properties commonly used in McLs. The table summarizes the absorption cross-section (σ_a), unsaturable absorption cross-section (σ_{ns}), recovery time (τ_{rec}), operating spectral band, thermal conductivity (κ), and material type.

Absorber material	σ_a ($\times 10^{-18}$ cm^2)	σ_{ns} ($\times 10^{-20}$ cm^2)	τ_{rec} (µs)	Oper. band (nm)	κ (W m^{-1}K^{-1})	Material type
Cr^{4+}:YAG	4–5	1–3	1–5	1030, 1064	14.0	crystal (cubic)
V^{3+}:YAG	1–3	≈ 2	2–6	1319	14.0	crystal (cubic)
Co^{2+}:Spinel	0.5–1.0	0.2–1	0.5–2	1200–1600	12.0	crystal (cubic)
Cr^{2+}:ZnSe	20–40	2–5	0.1–1	2000–2800	18.0	amorphous
SESAM [79–81]	nonlinear	nonlinear	10^{-6}–10^{-2} (engineered)	700–2000	≈ 40	GaAs/AlGaAs, InGaAs
Graphene [82, 83]	nonlinear	nonlinear	$\approx 10^{-7}$ (engineered)	600–3000	≈ 100	Graphene layer(s)

volume. The same principle underlies efficient pumping in McL.

The central emission wavelength and gain bandwidth of a laser material are closely linked to its suitability for specific applications. A broader gain bandwidth, as in Yb:KGW, enables wide-range wavelength tuning [53]. Similarly, the multi-wavelength visible emission of Pr:YLF is advantageous for applications in display technology, remote sensing, and high-density optical data storage [54, 84]. However, a wide emission bandwidth can be disadvantageous when single-longitudinal-mode operation is required, as the limited frequency spacing between cavity modes can lead to multi-mode oscillation [1].

Four-level laser materials, typically based on Nd ions, are advantageous in short McL cavities due to their low lasing threshold and negligible reabsorption [16, p. 126]. In contrast, quasi-three-level materials—commonly based on Yb, Pr, Er, Tm, or Ho ions—exhibit significant reabsorption [16, p. 126] enabling self-Q-switching operation [42–46]. Such lasers can generate nanosecond-scale pulses at gigahertz-level repetition rates with microjoule-level energies [42].

The thermal conductivity of the laser host matrix plays a critical role in dissipating heat, reducing thermally induced birefringence, preventing thermal fracture, and ensuring stable cavity performance [16, pp. 41, 43, 44, 70]. Isotropic (cubic) crystals such as YAG exhibit high thermal

conductivity and polarization-independent operation, making them thermally robust, though they do not provide intrinsic polarization selection. Uniaxial crystals such as YVO_4 and YLF, as well as biaxial crystals including KGW, KYW, and YAP, exhibit strong polarization-dependent gain that naturally supports single-polarization operation. In contrast to isotropic hosts such as YAG, the use of anisotropic crystals can significantly reduce thermally induced birefringence effects [16, p. 677]. However, many of these materials exhibit lower thermal conductivity [16, pp. 54–69], which can result in stronger thermal gradients and associated wavefront distortions under high pump powers. Laser glasses (e.g., Er:Yb:phosphate glass) possess some of the lowest thermal conductivities among solid-state hosts [85, 86] and are therefore primarily employed in low-power applications (e.g., low-repetition rate, high energy [87]).

The most widely used passive saturable absorbers in McL systems include Cr^{4+}:YAG [22, 32, 34, 49, 50], V^{3+}:YAG [33, 35], Co^{2+}:$MgAl_2O_4$ (spinel) [88, 89], semiconductor saturable absorber mirrors (SESAMs) [20, 21, 28], and graphene-based absorbers [82, 90, 91]. The cavity gain modulation depth and the amount of energy stored in the inversion are governed by the absorber's initial transmission T_0, which depends on the material absorption cross-section σ_a, the state density N_0, and the absorber thickness L according to

$$T_0 = \exp(-\sigma_\mathrm{a} N_0 L)\,. \tag{2.2}$$

The desired value of T_0 can therefore be achieved by choosing an absorber material (via σ_a), adjusting its doping level (N_0), and selecting an appropriate length L [16, p. 524]. A high absorption cross-section is advantageous when the maximum achievable doping is limited, and when a very short cavity is required to produce short pulses [36]. Furthermore, a larger σ_a results in a reduced saturation fluence,

$$E_\mathrm{s} = \frac{h\nu}{\sigma_\mathrm{a}}, \tag{2.3}$$

so that a low absorbed energy causes a large change in absorption. Ideally,

the saturation fluence of the gain medium should be much larger than that of the absorber [36] so that the inversion is efficiently depleted while only a small fraction of photons is lost in the absorber. For optimal passive Q-switching performance, the unsaturable absorption cross-section σ_{ns} (see Table 2.2) should be much smaller than the saturable part, i.e. $\sigma_{\mathrm{ns}} \ll \sigma_{\mathrm{a}}$, so that parasitic losses remain minimal [36, 37]. The absorber recovery time τ_{rec} sets the upper limit for the achievable repetition rate [36], approximately

$$f_{\mathrm{rep}} \approx \frac{1}{\tau_{\mathrm{rec}}}. \tag{2.4}$$

When the pumping rate exceeds this limit, the absorber does not fully recover between pulses and remains partially bleached, leading to quasi-CW operation with reduced pulse energy and incomplete inversion extraction [16, p. 496].

The Cr^{4+}:YAG absorber is predominantly used with Nd- and Yb-doped laser crystals [32, 49], due to its high absorption cross-section in the 1000–1070 nm spectral region. The V^{3+}:YAG absorber [35] is primarily employed for Q-switching at 1319 nm in Nd:YAG lasers. Co^{2+}:$MgAl_2O_4$ (spinel) is commonly used in Er:Yb:glass lasers operating near 1.5 μm [88], whereas Cr^{2+}:ZnSe is suitable for Q-switching in the 2 μm region, particularly with Tm:YLF. SESAM and graphene absorbers are preferred for high-repetition-rate operations due to their intrinsically short recovery times [20].

In certain designs, the laser gain medium can be co-doped with ions that simultaneously act as a passive Q-switch absorber [92–94], enabling further cavity miniaturization and highly compact microchip configurations.

2.1.3 Applications

McLs can serve as compact, single-longitudinal-mode, frequency-stable sources in optical-feedback measurement technologies [95–97], in which back-reflected light re-enters the cavity, interferes with the intracavity

field, and modulates the laser's output power and frequency. By analyzing these modulations, one can determine displacement, vibration, flow rate, birefringence or stress, refractive index, thermal expansion coefficients, lens thickness, and related parameters [95].

McL cavities can support two orthogonally polarized longitudinal modes with a stable frequency difference on the order of megahertz. This property is exploited in dual-frequency laser interferometry [98, 99] for measuring displacements, vibrations, stress, and related parameters.

McLs can act as compact and stable seed sources for coherent LiDAR (LADAR) systems [100–102]. For LADAR applications, precise frequency tuning in the kHz–MHz range can be achieved using either a piezoelectric transducer or an intracavity electro-optic modulator [9].

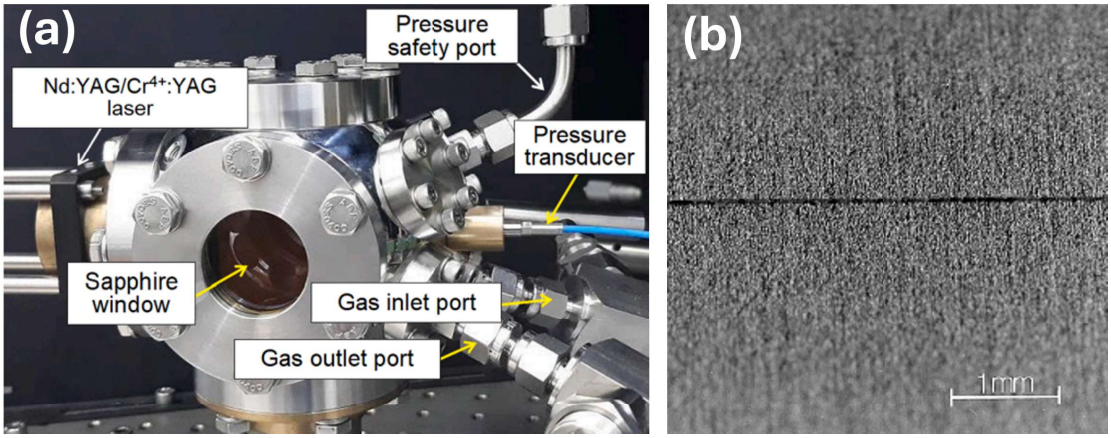


Figure 2.2: (a) McL with Nd:YAG crystal and Cr^{4+}:YAG absorber ignites air-methane mixture in combustion engine [103]. (b) Passively Q-switched McL mark on steel plate [2].

Passively Q-switched McLs can reach megawatt-level peak powers and are therefore well suited for applications such as laser range-finding [2] or laser-induced breakdown spectroscopy (LIBS) [104, 105], including quantitative analysis of the chemical composition of geological materials in space research [106, 107]. The relatively high peak powers generated by McLs also enable laser-assisted ignition of engine fuels [103, 108]; see Fig. 2.2(a). Moreover, their short and intense pulses are ideal for a variety of nonlinear-optical processes, including second-harmonic generation (SHG) [109], optical parametric oscillation (OPO) pumping [110, 111],

Raman conversion [112], and supercontinuum generation [113].

McLs are employed in a variety of industrial applications, including metal ablation [114], laser peening [115], micro-welding [116], micro-drilling [117], and steel or dental marking [2, 118]; see Fig. 2.2(b).

McLs can be used as simple, compact, and cost-effective seed sources for generating ultrashort picosecond pulses. McLs can serve as a potential substitute for mode-locked laser oscillators [119] for ultrashort pulse generation [28] and can be amplified in single-pass [120, 121] or double-pass [122] Nd:YVO_4 or Nd:YAG [123] amplifier stages. McL pulses can also be compressed from ∼100 ps to a few picoseconds—or even below 200 fs—using nonlinear pulse-compression techniques [124–126].

2.2 Transverse Modes in McLs

Since the first laser was generated [8], the laser transverse mode (TM) theory started to develop [127, 128], [59, Ch. 14.1].

In closed electromagnetic cavities with lossless boundaries, the wave equation is governed by a Hermitian operator, which guarantees the existence of a complete and orthogonal set of normal modes. In contrast, optical laser resonators are open systems, for which the round-trip propagation operator is generally non-Hermitian. Despite these mathematical difficulties, extensive experimental and empirical evidence has established that transverse modes in open optical resonators do exist and provide a physically meaningful and practically useful basis for describing laser oscillation in real laser systems [59, p. 568].

Transverse cavity modes in an optical resonator can be defined as self-reproducing transverse field distributions. After one complete round trip in the resonator, the transverse field pattern generally changes due to diffraction, reflection, and aperture losses. However, if a particular transverse field distribution returns to the same transverse form after a round trip—apart from an overall amplitude reduction and an arbitrary phase shift, then it can be considered as a transverse eigenmode of the resonator. Such self-consistent transverse modes maintain their spatial

profile upon repeated propagation through the resonator, even though their amplitude may decay due to losses. When optical gain compensates these losses, the resonator can sustain the transverse mode [59, p. 563].

The well established classical optical resonator theory [127] explicitly defines the transverse modes arising in resonators built from curved mirrors. In that case, the solutions satisfy paraxial approximation of the scalar wave equation, take the shape of the Gauss-Hermite or Gauss-Laguerre functions. The classical theory considers an idealized resonator operating close to the generation threshold without gain saturation and gain guiding effects. The transverse light dynamics in such resonators is analogous to the dynamics of wave-function in parabolic potential well (solution of the Schrödinger equation for a quantum harmonic oscillator) as described in textbooks of quantum mechanics [129].

In planar optical resonators formed by two perfectly aligned flat mirrors, transverse modes still exist. For plane-mirror resonators with circular aperture, the lowest-order transverse modes exhibit radial intensity variations resembling low- and higher-order Bessel functions [59, p. 564–565] (fig. 2.3).

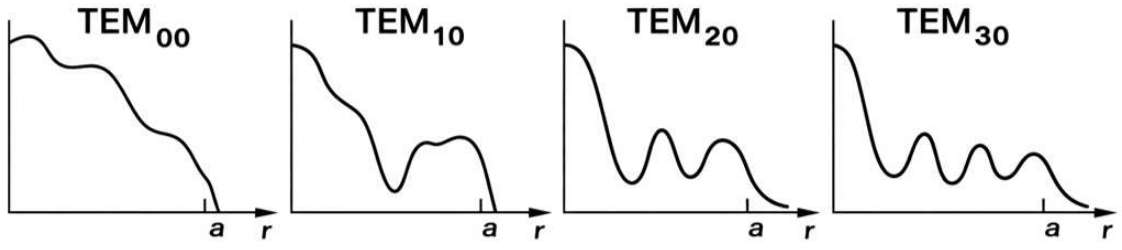


Figure 2.3: Approximate shapes of transverse modes supported by a planar cavity consisting of two perfectly aligned flat mirrors with aperture radius a [59, p. 564].

Early discussions of propagation through parabolic gain-guided or "complex parabolic" lensguides were given in [129–131], even before the concept of a McL was established [1]. A particularly important aspect of complex paraxial optics is that systems with positive gain or loss guiding can still support transversely confined and guided Gaussian modes even in the presence of divergent or unstable mirrors, as demonstrated by

Casperson and Yariv [130].

After the first demonstration of McL [1], which contains plano-plano mirror configuration (see Fig. 3.2), theoretical models investigating the microchip cavity dynamics appeared [132]. In order to facilitate the problem complexity, the transverse pumping profile was approximated as infinitive parabola, which author himself described as unphysical. Further investigations [133–136] consider transverse mode behaviour with localized gain profiles and treat the problem only in one-dimension. The significant works of [137, 138] combined the theoretical investigation with experiment, where the gain and refractive index profiles are approximated as gaussian and parabolic respectively. The latter approach does not help to find the solutions analytically, eigenstates have to be calculated purely numerically. Also the thermally induced lens modulates the phase logarithmically outside the pumping region [75] and the parabolical approximation is rather ideally suitable for resonator with curved output couplers.

It's worth mentioning that next to the solid-state microchip, also the vertical-cavity surface-emitting lasers (VCSELs) can contain plano-plano mirror configuration. The theoretical investigation of such lasers [139–141] calculates the gain profile numerically from the carrier diffusion equation. Then the transversal modes follow to be calculated numerically similar as in solid state microchip [137].

However, the most severe drawback of mentioned investigations [132–141] is the failure to provide a plausible picture of the multi-mode emission of such laser. Rigorous nonlinear calculations are very complicated even in single longitudinal mode case (so-called mean field approximation), see for instance [142], and hardly possible in full multi-transverse, multi-longitudinal mode description. Therefore the absence of a simple method to calculate the beam radiation profiles forces laser engineers to use some intuitive assumptions about the number of modes supported by the resonator, relating it to the Fresnel number [16, p. 223].

In many relevant cases, in particular for large pump powers, i.e. highly nonlinear regimes, the transverse mode investigation description

becomes very approximate or even ceases to work [142–144]. Transverse mode investigation in nonlinear regime is still the subject of current research [145, 146]. For some special lasers, like McLs, the classical mode theory is hardly applicable from the very beginning, as their resonators consist of plane mirrors. The parabolic trapping potential is then absent, and the electromagnetic radiation is confined in the transverse space of the resonator by other mechanisms, predominantly by the gain guiding. Thermal lensing also appears to play important role in confining the radiation in McL under strong pump power.

The approach provided in section 3.1 aims to fill the gap by providing analytical and numerical treatment of transverse modes in McLs in two dimensions. Using the cylindrical (flat-top) pumping profile approach, we provide a simple theory of the gain-guided and thermal-lens supported modes in such plane-plane mirror resonators. We rigorously calculate the transverse mode functions, their eigenfrequencies and generation threshold conditions, and its beam quality factor (M^2). All this allows us to estimate multi-mode beam (composite) M^2 dependence on pumping strength. This simple and intuitive approach leads to the beam quality estimations corresponding well with the experimental measurements performed and reported there.

2.3 Laser Beam Quality Factor M^2

The concept of the laser beam quality factor (M^2) was introduced by A. E. Siegman [147] in nearly the same year that the first McL was demonstrated [1]. The beam quality factor was formulated to be applicable to essentially any real laser beam.

The M^2 formulation accommodates non-Gaussian, non-diffraction-limited, and potentially multi-mode laser beams with a time-averaged intensity profile $I(x, y, z)$ and corresponding spatial-frequency distribution $I(s_x, s_y)$. Their variances, denoted $\sigma_x^2(z)$ and $\sigma_{s_x}^2$, are defined as:

$$\sigma_x^2(z) = \frac{\iint (x - x_0)^2 I(x, y, z)\, \mathrm{d}x\, \mathrm{d}y}{\iint I(x, y, z)\, \mathrm{d}x\, \mathrm{d}y}, \tag{2.5}$$

$$\sigma_{sx}^2 = \frac{\iint (s_x - s_{x0})^2 I(s_x, s_y)\, \mathrm{d}s_x\, \mathrm{d}s_y}{\iint I(s_x, s_y)\, \mathrm{d}s_x\, \mathrm{d}s_y}, \tag{2.6}$$

The key analytical result presented in [147] is that the variances of any real laser beam satisfy the following relationship:

$$\sigma_x^2(z) = \sigma_{x0}^2 + \lambda^2 \sigma_{sx}^2 \left(z - z_{0x}\right), \tag{2.7}$$

where any real beam contains a minimum variance σ_{x0} at a waist position $z = z_{0x}$. In addition, the variances of any real beam satisfy another fundamental relationship [147]:

$$\sigma_{x0}\sigma_{sx} = \frac{M_x^2}{4\pi}, \tag{2.8}$$

where M_x^2 is the beam quality factor in the x direction, as defined by this expression. For an ideal Gaussian beam, the space–beamwidth product is $\sigma_{x0}\sigma_{s_x} = \frac{1}{4\pi}$, and therefore the beam quality factor can be expressed as:

$$M_x^2 = \frac{\text{Real beam space—beamwidth product}}{\text{Ideal gaussian space—beamwidth product}} = 4\pi\sigma_{x0}\sigma_{sx}. \tag{2.9}$$

The term "beam quality" is generally understood as a measure of the relationship between a laser beam's near-field size σ_{x0} and its far-field divergence σ_{s_x}. In most applications, a beam with the smallest possible near-field size and the lowest possible divergence is desired—conditions that are most closely achieved by an ideal Gaussian beam.

The analytical framework based on the variances of the spatial and spatial-frequency intensity distributions has one notable limitation. If the beam possesses a discontinuous edge—such as an ideal single-slit pattern or a top-hat profile—then the spatial-frequency variance diverges, $\sigma_s \to \infty$, making this formalism invalid [147, 148].

In cases where the complex beam field distribution $A(x, y)$ is known only at a single plane outside the waist position ($z \neq z_{0x}$), and the beam quality factor M^2 must be determined from this single distribution, analytical methods have been developed for this purpose [149–151]. These approaches have been adapted and practically implemented for McLs in Section 4.3.2.

2.4 Spatial Filtering in McLs

The performance of McL is constrained due to the poor spatial quality of the emitted beam, particularly in high-power operation regimes. As a representative example, McLs operating in high-power continuous wave (CW) regimes, with pump power around 1 kW and output power between 200 and 500 W, emit a multi-mode beam with a quality factor (M^2) greater than 100 in an edge pumping configuration [71, 72]. To limit beam quality deterioration, the cavity length is typically 50 mm or longer. Compact, longitudinally pumped microchips balance output power and beam quality, with the beam quality factor (M^2) usually ranging from 1 to 10 [6, 152–155]. At the threshold, the beam is quasi-Gaussian with an M^2 close to 1, but higher-order modes surpass the threshold as the pumping power increases, causing beam quality to deteriorate. The heat generated by the pump radiation causes an axial expansion of the rod and leads to the stress [16, pp. 473–477] contributing to beam quality deterioration. Laser performance can be improved by using composite active material with undoped end caps [155, 156] or longitudinal doping gradient [157].

Passive Q-switching in McL [11] is achieved by adding the absorber inside the cavity. In addition to modulating resonator quality, the absorber acts as a soft aperture [108, 152], enhancing beam quality. However, it does not fully resolve the issue of deteriorating beam quality. Consequently, the beam quality factor (M^2) stays in the range of 4-8 when output energies are between 4 and 30 mJ [69, 70, 103, 158].

Brightness depends linearly on power and inversely on the square of

M^2 [148], making it more sensitive to M^2. In shorter cavities, M^2 has steeper dependence on pump power [6], reaching maximum brightness near the threshold. Further increasing pump power does not improve brightness [159]. Various attempts have been made to enhance brightness of McL radiation, such as optical injection [160], external feedback [161, 162], external gratings and beam manipulation techniques [163, 164], among others. However, these solutions affect negatively the compactness and simplicity of the design. A conventional intra-cavity spatial filter (consisting of two confocal lens configuration with the iris in focal plane) is impossible due to compact design of the McL resonator. An alternative approach was proposed by integration of a photonic crystal with spatial filtering functionality [165–167] inside the laser cavity . This helped to increase the brightness of laser emission by a factor of three [159] while maintaining the laser's compact and of straightforward design.

Angular filtering can be implemented in both transmission[168] and reflection [169, 170] modes, with reflection mode being more important to microchip cavities. Theoretical studies have shown that higher-order mode suppression can be achieved by replacing the rear mirror with a resonant grating mirror [169]. To achieve this, resonant gratings supplemented by an additional multi-layer sub-mirror were introduced, although they have not been tested in a laser cavity [170]. Similar to the filters mentioned in [171, 172], these filters are positioned in front of the plane mirror. A step forward to the real AFM was achieved recently in [173] by observation, that the Fano-like resonances in nanostructured thin films enabled a strong transmission sensitivity to the angle of incidence. Such an element is characterized by frequency and angular selectivity of light transmission through the structure. The performance of cavities employing such an angular-filtering mirror is discussed in Section 3.2, where both experimental results and numerical simulations are presented.

2.5 Polarization Filtering in McLs

Significant part of McL applications, such as nonlinear interactions, remote sensing, imaging, communication, and others, demand stable polarization with high contrast. This can be achieved either through polarized pumping–induced gain anisotropy [174–181] or by incorporating an intra-cavity polarizer, particularly one operating at zero angle of incidence (AOI=0) [153, 182–186].

The Nd:YAG mono-crystal exhibits slight birefringence as a result of mechanical stress imposed by the crystal holder [174–176]. Consequently, the orthogonal polarization states experience slightly different refractive indices, leading to a small difference in optical path lengths. This difference allows two orthogonal combs of longitudinal modes to coexist [174–176]. The orientation of the orthogonal polarization states is determined by the geometry of the crystal holder. Additionally, the gain in Nd:YAG is anisotropic and depends on the polarization direction of the pump. When the pump polarization aligns with one of the orthogonal polarization eigen-states, the gain for that state increases, resulting in linearly polarized laser output.

In Section 3.3, the meta-mirror [5] is introduced as a polarizing output coupler operating at normal incidence (AOI = 0). It exhibits high reflectance for the S-polarized component while transmitting the orthogonal P-polarized component, thereby increasing the lasing threshold for the P polarization and favoring oscillation in the S-polarized state. The meta-mirror is employed at various rotation angles such that the S and P polarization axes either align with or deviate from the intrinsic orthogonal polarization axes of the Nd:YAG laser crystal. Furthermore, the pump polarization direction is adjusted to either coincide with or differ from both the meta-mirror polarization axes and those of the Nd:YAG crystal. The experimental results examine these different configurations and provide insight into the dominant mechanisms responsible for polarization-contrast enhancement over a range of pump powers in the Nd:YAG microchip-laser cavity.

Chapter 3

Results

3.1 Transverse Modes and Beam Quality in McLs

Publication directly related to this dissertation section:

Matas Plukys, Eugenijus Gaizauskas, Darius Gailevicius, and Kestutis Staliunas, "Transverse modes and beam spatial quality in microchip lasers," *Physical Review A*, vol.107, p. 043505, 2023, https://link.aps.org/doi/10.1103/PhysRevA.107.043505

In this section, the transverse modes of flat–flat McL resonators (see Fig. 3.1) are analyzed, where the mode structure is determined by the combined effects of gain guiding and thermal lensing. The transverse mode profiles, their eigenfrequencies, generation thresholds, and corresponding beam-quality factors (M^2) are rigorously computed. These results enable prediction of the dependence of the composite (multi-mode) beam-quality factor on the pump strength.

A key element of the analysis is the assumption that, in the multi-transverse-mode regime, the relative amplitudes of the excited modes are proportional to their individual modal gains. This simple and practical model yields beam-quality estimates that show good agreement with experimental measurements presented in this section.

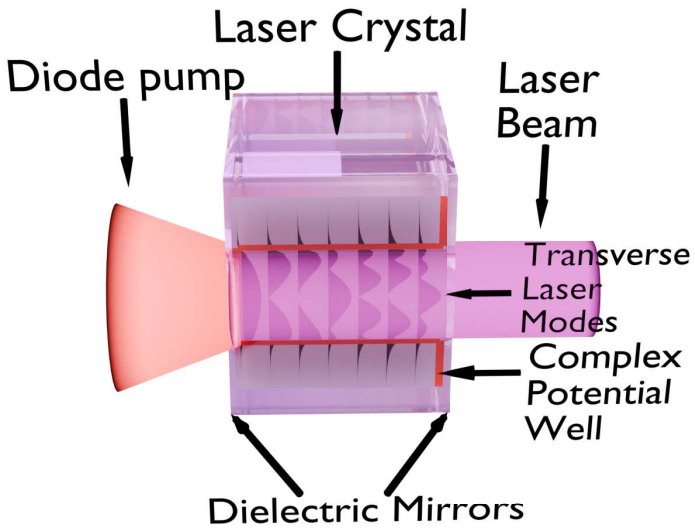


Figure 3.1: Schematic drawing of end-pumped McL with guiding section induced by pump beam.

It should be noted that most reported McLs employ very short resonators with plano–plano mirrors [1, 132–134, 187]. However, several studies refer to "microchip lasers" implemented using short crystals placed in cavities with curved output couplers [137, 138, 188], or employing side pumping and moderately long cavities [189]. In such configurations, the resonator behavior is dominated by classical phase modulation, and the pump distribution typically overlaps well with the standard Gaussian–Laguerre cavity modes. For these cases, gain guiding and thermal lensing act only as perturbations to classical resonator theory [59, 127], and the analytical framework developed in this section is not directly applicable.

3.1.1 Linear field equation in 2D

We consider a simplified model for the laser resonator, where the gain guiding and thermal lensing effects are uniformly distributed over the whole crystal length. In this case, the linear evolution equation for the slowly varying electric field envelope $A(r, \phi, t)$ in two transversal

dimensions reads very similar as described in [133, 135, 142]:

$$\frac{\partial A}{\partial t} = -\rho A + id\nabla A + i\sigma(r)A + \gamma(r)A. \tag{3.1}$$

Here time t is normalized to the cavity round-trip time. The coefficient ρ signifies the total losses per one resonator round-trip, diffraction coefficient $d = L/k$, where L and k are resonator length and wavenumber, respectively. We further consider the axisymmetric case, in which the thermally induced refractive-index distribution $\sigma(r)$ and the pump-induced gain profile $\gamma(r)$ depend solely on the radial coordinate r. The refractive-index distribution $\sigma(r)$ arises from heat deposition due to absorbed pump power, which leads to the formation of a thermal lens [75].

The (3.1) contains no gain saturation term, which would allow evaluating the nonlinear dynamics of laser radiation adequately [142]. With this term included, the problem becomes not universally solvable even in the simplest single-longitudinal-mode approximation. We consider the linear, simplified, non-saturated laser light dynamics (3.1), which allows us to calculate exponentially growing/decaying eigen-solutions, the transverse modes of the resonator. The calculated eigenvalues allow us to define the threshold and beam quality M^2 of the multi-mode beam, which consists of individual transverse modes with unequal weights, dependent on their growth rates.

We solve the equation (3.1) in polar coordinate system using usual separation of radial and angular variables in the following form:

$$A(r, \phi) = A_l e^{\lambda t} v(r) e^{i\phi l}, \tag{3.2}$$

where l stands for the orbital number $l = 0, \pm 1, \pm 2..$ and λ is the separation constant. Substituting (3.2) into the (3.1) we get:

$$r^2 \frac{\partial^2 v}{\partial r^2} + r\frac{\partial v}{\partial r} + r^2 v \left(\frac{i\sigma(r) + \gamma(r) - \lambda - \rho}{id} \right) - l^2 v = 0. \tag{3.3}$$

The solution $v(r)$ depends on thermal lens and gain functions $\sigma(r), \gamma(r)$. In order to get the analytical form of $v(r)$ we approximate $\sigma(r), \gamma(r)$ by

adequate functions. Specifically, for the end-pumped McL, due to strong localization and the multi-mode character of the laser diode pump, the gain profile is approximate to flat-top. The refractive index profile is a solution of heat equation and depends on pumping profile. In our case, the refractive index profile is parabolic inside the pumped region and logarithmic outside of it [75]. In order to facilitate the semi-analytical treatment, we go with the assumption, that the refractive index and gain profiles are flat-top functions:

$$\sigma(r) = \begin{cases} S_0 & \text{if } r < R; \\ 0 & \text{if } r > R; \end{cases} \quad , \; \gamma(r) = \begin{cases} G_0 & \text{if } r < R; \\ 0 & \text{if } r > R. \end{cases} \tag{3.4a,b}$$

The step-refractive-index profile may seem counter-intuitive because the ideal lens contains parabolic phase modulation. Indeed, the parabolic approximation is ideal for the internal pumping region but undergoes rising deviations moving away from it. The step-refractive-index approximation should be a reasonable compromise inside and outside the pumping region. The calculated modes and modal eigenvalues are similar to the ones with the parabolic approximation. However, due to the infinitive endings, the parabolic approximation predicts too many modes.

One should notice that after introducing the refractive index and gain cylindrical functions (4.115a,b) into the linear field equation (3.3), it becomes analogical to Schrödinger wave equation with finite and complex valued potential well. The separation constant λ also becomes a complex number, and the sign of its real part $\Re(\lambda)$ defines whether the appropriate solution of (3.2) will grow or decrease. The laser modes are above generation threshold if $\Re(\lambda) > 0$.

Normalizing the radial coordinate r to the radius of gain profile as $\xi = r/R$, from (4.115a,b) and (3.3) we get the two Bessel differential equations of the form:

$$\begin{cases} \xi^2 \frac{\partial^2 v}{\partial \xi^2} + \xi \frac{\partial v}{\partial \xi} + \xi^2 v\alpha^2 - l^2 v = 0 & \text{if} \quad \xi < 1, \\ \xi^2 \frac{\partial^2 v}{\partial \xi^2} + \xi \frac{\partial v}{\partial \xi} - \xi^2 v\beta^2 - l^2 v = 0 & \text{if} \quad \xi > 1, \end{cases}, \tag{3.5}$$

where complex coefficients α and β are given by:

$$\alpha^2 = R^2 \frac{iS_0 + G_0 - \lambda - \rho}{id} \quad , \quad \beta^2 = R^2 \frac{\lambda + \rho}{id}. \tag{3.6}$$

An additional complex valued coefficient ζ characterizes the complex potential well depth:

$$\zeta^2 = R^2 \frac{iS_0 + G_0}{id}. \tag{3.7}$$

The three coefficients are interrelated by equality:

$$\zeta^2 = \alpha^2 + \beta^2. \tag{3.8}$$

The potential-well depth ζ depends on the gain coefficient G_0 and the refractive-index modulation amplitude S_0, assuming that the pump-spot radius R and the diffraction coefficient d are fixed. The gain coefficient G_0 is proportional to the absorbed pump power [16, p. 119], while the strength of the refractive-index modulation S_0 also scales with the absorbed pump power [75]. Consequently, the absorbed pump power is the physical parameter that directly determines the potential-well depth ζ.

The solution of (3.5) should be finite inside the cylinder ($\xi < 1$) and tend to 0 if $\xi \to \infty$ outside the cylinder ($\xi > 1$). The proper solutions are Bessel function of the first kind $J_l(\alpha\xi)$ and modified Bessel function of the second kind $K_l(\beta\xi)$ accordingly. The both Bessel functions should be equal at $\xi = 1$:

$$\begin{cases} v(\xi) = J_l(\alpha\xi) & \text{if} \quad \xi < 1; \\ v(\xi) = \frac{J_l(\alpha)}{K_l(\beta)} K_l(\beta\xi) & \text{if} \quad \xi > 1. \end{cases} \tag{3.9}$$

The derivatives of $v(\xi)$ at $\xi = 1$ should be equal as well. We can use the recurrence relation [190] to calculate the derivatives:

$$\begin{cases} \dfrac{d}{d\xi} J_l(\alpha\xi) = \alpha J_{l-1}(\alpha\xi) - \dfrac{l}{\xi} J_l(\alpha\xi)\,, & \text{if } \xi < 1, \\ \dfrac{d}{d\xi} K_l(\beta\xi) = -\beta K_{l-1}(\beta\xi) - \dfrac{l}{\xi} K_l(\beta\xi)\,, & \text{if } \xi > 1. \end{cases} \tag{3.10}$$

Combining (3.9) and (3.10) we obtain the transcendental equation relating α and β eigenvalues:

$$\frac{\alpha J_{l-1}(\alpha)}{J_l(\alpha)} = -\frac{\beta K_{l-1}(\beta)}{K_l(\beta)}. \tag{3.11}$$

The eigenvalues α and β in (3.11) are complex valued and they could be found numerically.

3.1.2 Eigenfrequencies of Linear field Equation in 2D

We calculate the complex eigenvalue pairs (ζ,β) numerically from (3.11) transcendental equation, expressing α through β and ζ in (3.8). Due to orbital number l in (3.11), one eigenvalue of ζ can correspond to several eigenvalues of β. Furthermore, due to Bessel oscillatory behavior, each ζ can correspond to several β with the same l. Thus, each eigenvalue β is characterized by two mode numbers (l, m). The potential depth $|\zeta|$ physical meaning is related to pumping power. $\Re\left(i\beta^2\right)$ is proportional to growth factor of each single mode $\lambda_{re} + \rho$. On the other hand, $\Im\left(i\beta^2\right)$ is proportional to frequency of each single mode λ_{im}.

The modified Bessel function of the second kind $K_l(\xi\beta)$ tends to zero as $\xi \to \infty$ only if $|Arg(\beta)| < \frac{\pi}{2}$ [190]. On the other hand $\beta = R\sqrt{\frac{\lambda+\rho}{id}}$ where R, ρ, d are real and positive. Laser generates only if $\Re(\lambda) > 0$ therefore the β argument is restricted to $-\frac{\pi}{2} < Arg(\beta) < 0$ and $\frac{\pi}{2} < Arg(\beta) < \pi$. Combining with previous restriction one can finally state that β is only valid if $-\frac{\pi}{2} < Arg(\beta) < 0$.

The potential well depth $\zeta = R\sqrt{\frac{S_0}{d} - i\frac{G_0}{d}}$ depends on real-valued positive G_0 and the real-valued (but not necessary positive) S_0. Therefore the phase of ζ is restricted to areas of $-\frac{\pi}{2} < Arg(\zeta) < 0$ and $\frac{\pi}{2} < Arg(\zeta) < \pi$. However, only the area of $-\frac{\pi}{2} < Arg(\zeta) < 0$ is relevant

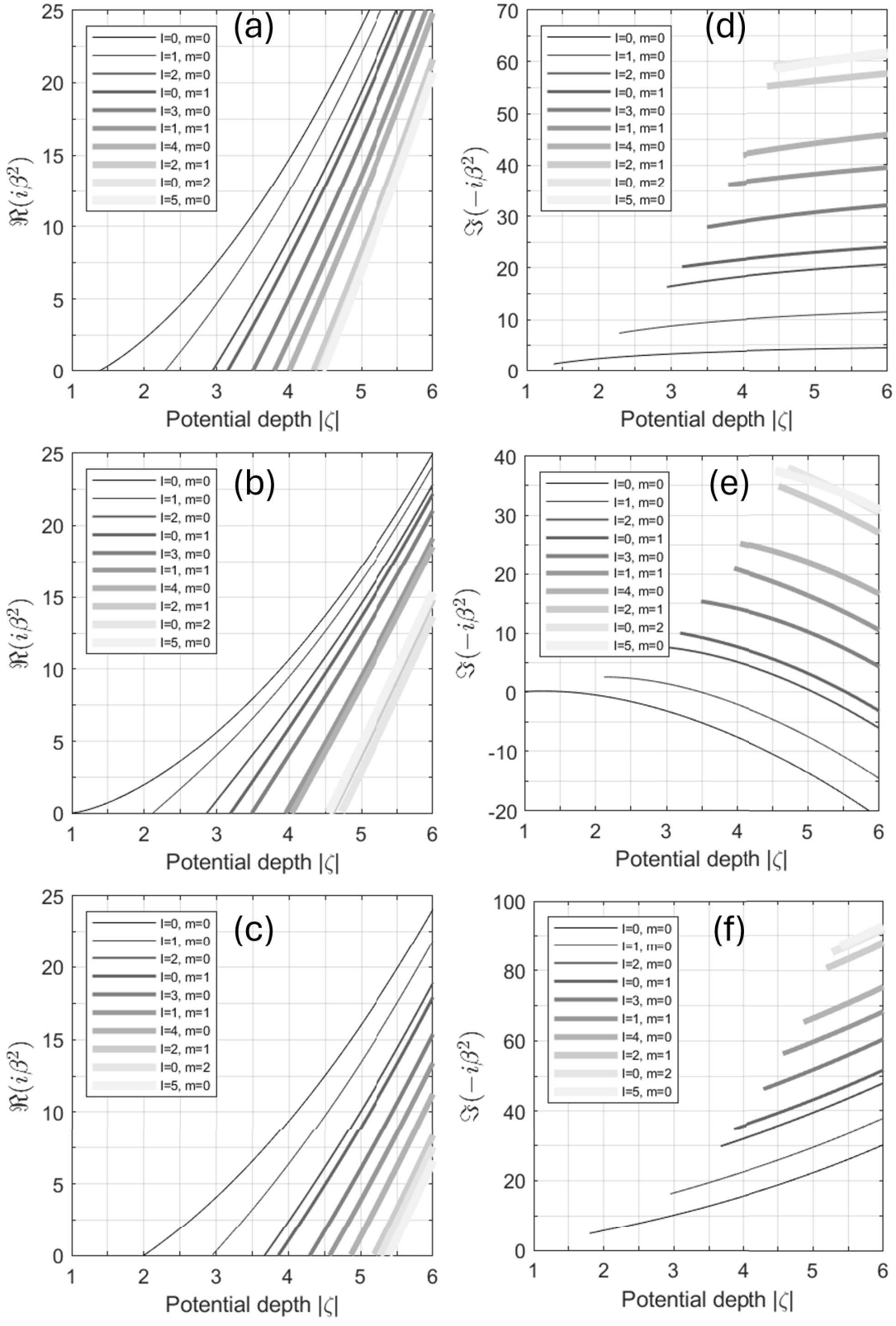


Figure 3.2: The gain $\Re\left(i\beta^2\right)$ and frequency $\Im\left(-i\beta^2\right)$ dependencies of the individual mods on the potential well depth $|\zeta|$. In the columns three cases are shown: (a,d) without a thermal lens $S_0 = 0$; (b,e) with a focusing lens $S_0 = G_0$; (c,f) with a defocusing lens $S_0 = -G_0$

.

because the both areas overlap using the square of ζ in equation (3.8). One can distinguish several important cases determined by the phase of potential depth ζ:

(I) If $S_0 = 0$, then $Arg(\zeta) = -\frac{\pi}{4}$ is a pure gain guiding case, where no phase modulation (lens) is present.

(II) If $S_0 > 0$, then $-\frac{\pi}{4} < Arg(\zeta) < 0$. This case is a mix of gain guiding and focusing lens (approximated as a cylinder). The focusing lens starts to dominate as the phase approaches zero.

(III) If $S_0 < 0$, then $-\frac{\pi}{2} < Arg(\zeta) < -\frac{\pi}{4}$. This case corresponds to a mix of a defocusing lens with gain guiding. The defocusing lens effect gets stronger as the phase approaches $-\frac{\pi}{2}$.

In order to grasp the dynamics, we treat special cases when $\arg(\zeta) = -\frac{\pi}{4}, -\frac{\pi}{8}, -\frac{3\pi}{8}$, corresponding pure gain guiding (I), the focusing thermal lens with gain guiding (II) and defocusing lens with gain guiding (III). The eigenvalues (ζ, β) for all three cases were calculated numerically, and dependencies of their real and imaginary parts (corresponding to the growth factor and frequency of every single mode) on the potential depth are shown in Fig 3.2. We have calculated the ten first modes (l,m) beyond the threshold. The first column in figure Fig 3.2 represents a pure gain guiding case, where no lens is present. Each mode starts to exist when $\Re\left(i\beta^2\right) > 0$. Increasing the potential depth (or pump power) from zero to $|\zeta| \approx 1,5$, the laser starts to generate fundamental mode $(0,0)$. Increasing the pump further, the growth rate $\Re\left(i\beta^2\right)$ increases and the frequency is decreasing in fundamental mode, while new modes $(1,0),(2,0),(0,1),(3,0),(1,1),(4,0),(2,1),(0,2),(5,0)$ start to emerge one after the other. More and more modes can potentially coexist together. Each new mode has lower growth ratio $\Re\left(i\beta^2\right)$ and higher frequency $\Im\left(-i\beta^2\right)$ than the one before. Similar to the first column in Fig. 3.2, the second and third columns represent cases where the thermal lens is focusing and defocusing ($G_0 = S_0$, $G_0 = -S_0$, accordingly). The tendencies are similar as in the pure gain guiding case. The focusing lens

reduces the generation threshold of the first mode, while the defocusing lens increases it ($|\zeta| \approx 1$ and $|\zeta| \approx 2$ accordingly). The frequency of every single mode tends to increase and decrease for focusing and defocusing cases while increasing the pumping.

3.1.3 Mode shapes and beam quality factors M^2

We depict the mode shape and its beam quality factor M^2 dependency on the potential well depth $|\zeta|$ in Fig 3.3. In the second row of Fig 3.3 we represent the potential well depth value $|\zeta|$ by a red dashed vertical line, and the ordinate axis scales only it. Meanwhile, the mode amplitudes are scaled to a fixed numerical value and are stacked vertically according to the sequence they come into existence deepening the potential value of $|\zeta|$. Each value of $|\zeta|$ supports a unique set of transverse modes, which differ by amplitude and phase distribution. Abscissa axis scale is valid for both potential well and mode amplitude, where the potential well radius coincides with the pumping cylinder radius. Here the corresponding eigenvalue pair (α, β) calculated from (3.11) represents radial mode shape in (4.46). The radial part should be inserted into the (3.2), so both angular and radial parts can be represented. Once we know the electrical field distribution, we can apply the methodology provided in appendix A and calculate the beam quality factor M^2.

In the first column of Fig 3.3, one can see the beam quality factor M^2 and mode shape dependency on potential depth $|\zeta|$ as no lens is present, only gain. The mode shape in (d) is represented by normalized electrical field absolute value $|A|$ and phase. The phase value is indicated by color in the radial part. We can identify that the higher potential depth $|\zeta|$ means a higher quantity of modes localized in the well. Increasing the pump up to $|\zeta| \approx 1,5$ the laser starts to generate fundamental mode $(0, 0)$. The mode is spread widely, and its beam quality factor M^2 is high. Further increasing the potential depth, the fundamental mode starts to localize better, and its beam quality factor M^2 reduces significantly while its endings become steep. The higher modes $(1, 0), (2, 0), (0, 1), (3, 0), (1, 1), (4, 0), (2, 1), (0, 2), (5, 0)$ follow the

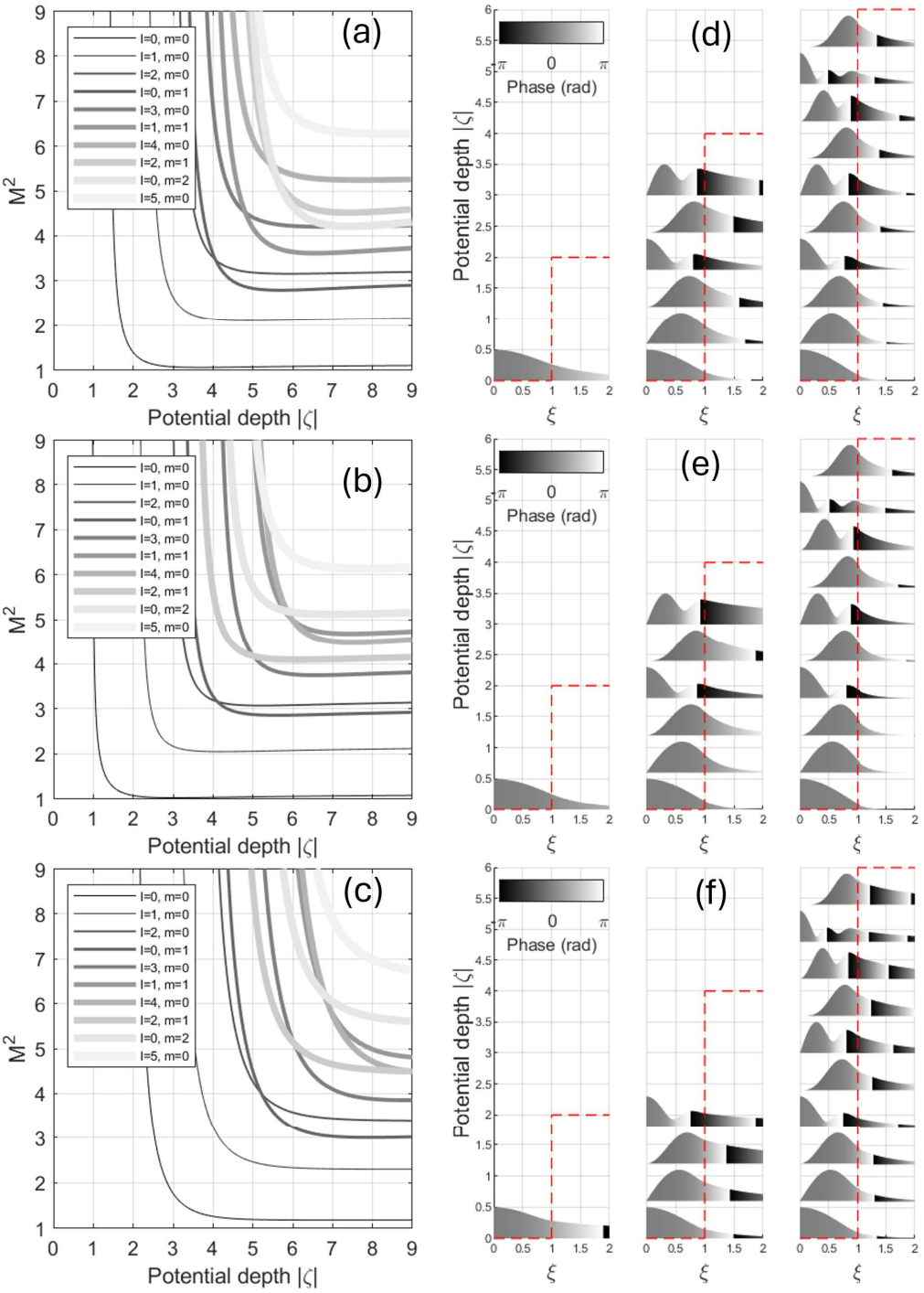


Figure 3.3: The beam quality factors and beam shapes of each individual modes depending on potential well depth $|\zeta|$. The mode shape is represented by normalized electrical field absolute value $|A|$ and phase, which is indicated by color in range $(-\pi;\pi)$. The red dashed lines in (d,e,f) signify potential well $|\zeta|$ in which the modes are localized, and the ordinate axis scales only it. Meanwhile, the mode amplitudes are scaled to a fixed numerical value and are stacked vertically according to the sequence they come into existence while deepening the potential $|\zeta|$. Abscissa axis scale is valid for both potential well and mode amplitude, where the potential well radius coincides with the pumping cylinder radius. The figures in three columns represent the same cases as in Fig 3.2.

same pattern; they localize from infinity with high M^2 and their endings become steep as the pump increases.

Very similar to the first column in Fig 3.3, the second and third columns represent cases where the thermal lens is focusing and defocusing ($G_0 = S_0$, $G_0 = -S_0$ accordingly). We see very similar tendencies as in the pure gain guiding case. In the case of the focusing lens, the mode endings are of weaker phase modulation than in the pure gain guiding case. Also, the modes are better localized at the same $|\zeta|$. The defocusing lens brings more phase modulation to endings. The focusing lens reduces the generation threshold of the first mode.

3.1.4 Composite beam quality factor M^2

In the previous section, we gave estimates of the beam quality factor M^2 dependencies on the possible depth of $|\zeta|$ for each transverse mode (l, m). Here we would like to calculate the beam composite beam quality factor M^2, consisting of multiple modes overlapping each other. We assume that our laser is of class B [142, p. 7] and modes compete very weakly with each other. This assumption is only empirical and should be verified with nonlinear analysis additionally, which is beyond the scope of this article. Following this assumption, we introduce an equation that could help preliminary estimate the composite beam quality factor:

$$M^2 = \frac{\sum_{l,m}^{\infty} M_{lm}^2 \left(\lambda_{re}\right)_{lm}}{\sum_{l,m}^{\infty} \left(\lambda_{re}\right)_{lm}}, \tag{3.12}$$

here only the modes with positive $(\lambda_{re})_{lm}$ are considered. We have summed up the beam quality factor of every single mode M_{lm}^2 multiplied by its growth ratio $(\lambda_{re})_{lm}$ and normalized the result to the sum of growth ratios. The equation (3.12) estimates the composite M^2 dependence on pumping for different resonator lengths and spots. Note, that the eigenvalues of $(\zeta, \Re\left(i\beta^2\right))$ (already calculated in previous section for three beam guiding cases) along with relations ((3.6)-(3.7)) can be used to find growing rates $(\lambda_{re})_{lm}$ and beam quality factors M_{lm}^2 for every single mode.

In our experiment, we use a McL of two different resonator round-trip lengths: $L_1 = 5mm$ and $L_2 = 15mm$. Other parameters are following: pumping spot radius $R = 140\mu m$; laser wavelength $1.064\mu m$; Nd:YAG crystal length 2,3 mm (the same crystal used in both cavities) , refractive index $n = 1.81$; losses per one round trip $\rho = 0.0825$; diffraction coefficient depends on resonator round trip length, so $d_1 = 4.67 \cdot 10^{-10} m^2$, $d_2 = 2.16 \cdot 10^{-9} m^2$. We estimate that in our experiments, the thermal lens-induced phase modulation is negligible compared with gain per round-trip ($S_0 << G_0$) and assume these as pure gain guiding cases. The calculated for this case λ_{re} and gain G_0 values are shown in the first column of the Fig 3.4 for both resonator lengths. The beam quality factor M^2 of every single mode is also recalculated analogically, and the results are shown in the middle column of the Fig 3.4. Here the dashed lines represent the states where no generation is present due to the negative growth factor $\lambda_{re} < 0$ of this particular transverse mode. The red squares represent the point, where the mode starts physically to exist.

Now, considering the pumping power P is directly proportional to gain G_0, we normalize both parameters to their threshold values. This assumption allows us to relate our experiment with theory. Calculated from (3.12), composite beam quality factor M^2 dependency on pump power is provided in the third column of Fig 3.4 as the grey curve for both resonator lengths. Measured according to ISO Standard 11146, the beam quality factor M^2 is depicted here as black stars with error bars. The shorter cavity experimental data finds better agreement with the theoretical curve than the longer one. One can recognize the slight vertical shift and undulations. In our understanding, the longer resonator generates modes of weaker localization and higher beam quality factors at the threshold. Weakly localized modes contain higher M^2 factors and bring rapid contribution to composite beam quality factor increasing the pump power. Accordingly, the major undulations are observed in the longer cavity theoretical and experimental curves. On the other hand, less localized modes are more sensitive to crystal aperture, which is not

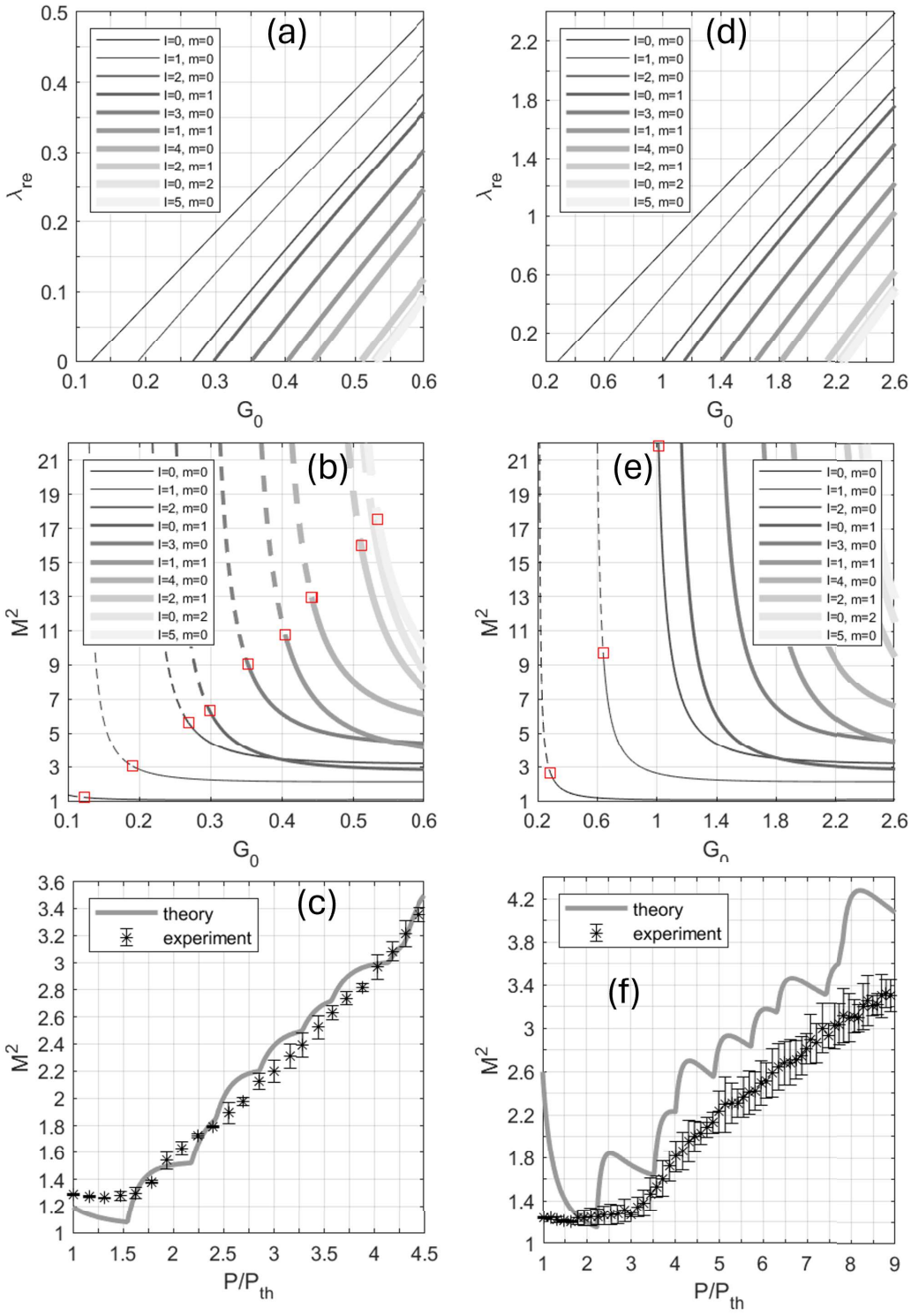


Figure 3.4: Growth ratio λ_{re} (a,d), single mode beam quality factor (b,e) and composite beam quality factor (c,f) dependencies on gain G_0 and pump power P/P_{th} over the generation threshold P_{th}. The first and second rows correspond to different resonator round-trip lengths $L = 5mm$ and $L = 15mm$, respectively. The grey curves in (c) and (f) represent the theoretically estimated M^2 while the black stars with error bars - experimentally measured values. The dashed lines in (b,e) represent the states where no generation is present due to the negative growth factor $\lambda_{re} < 0$ of this particular transverse mode. The red squares represent the point, where the mode starts physically to exist.

included in the theoretical model. That could contribute to the vertical offset. It is worth mentioning, that the mean-field approximation fits the shorter cavities better. Due to the big contribution of free space in longer cavity (4.6 mm Nd:YAG crystal and 10.4 mm free space), the gain is distributed very unevenly along the cavity axis, and this is not included in our theoretical model. Despite the discrepancies noted, the theoretical and experimental results overlap adequately and allow us to claim that the method is suitable for a rough estimation of laser beam quality factor M^2 at various pump powers in McL.

3.1.5 Summary

We have investigated the influence of several physical effects and parameters on the beam quality of the flat-flat mirrors McL analytically. For this reason, the 2D linear field equation was introduced using cylindric symmetry and mean field approximation. The physical effects accounted for this analysis of laser beam formation were the gain, thermal lens, diffraction, and losses. In this case, the equation becomes similar to Schrödinger wave equation with a finite potential barrier, which is complex in our case. We have found the eigenvalues and eigenfunctions (corresponding to mode shapes) for three specific cases and evaluated beam quality factors M^2 and growth ratios λ_{re} for each separate mode. For simplicity, we introduced an equation that allows rough estimation of composite (multiple modes) beam quality factor M^2, disregarding competition of generated modes. Calculated M^2 values were compared to experimental ones, and satisfactory agreement was found.

3.2 Spatial Filtering in Photonic Crystal McL

Publication directly related to this dissertation section:

Matas Plukys, Lina Grineviciute, Julianija Nikitina, Darius Gailevicius, and Kestutis Staliunas, "Enhancement of brightness in microchip laser with angular filtering mirrors," *Optics & Laser Technology*, vol.181, Part

C, p. 111904, 2025, https://doi.org/10.1016/j.optlastec.2024.111904

McLs are very compact and efficient coherent light sources; however, their applications are restricted due to poor beam quality and limited brightness, especially in high-emission power regimes. We used a thin-film-based angular filtering mirror to substitute one of the planar resonator mirrors to solve this limitation. The angle-selective reflection suppresses the high-order transverse modes and enables lasing on the lowest-order ones, thus improving the spatial quality of the emitted beam. Our experimental results, supported by numerical simulations, demonstrate decrease of beam quality parameter M^2 and a twofold increase in the brightness of emitted radiation.

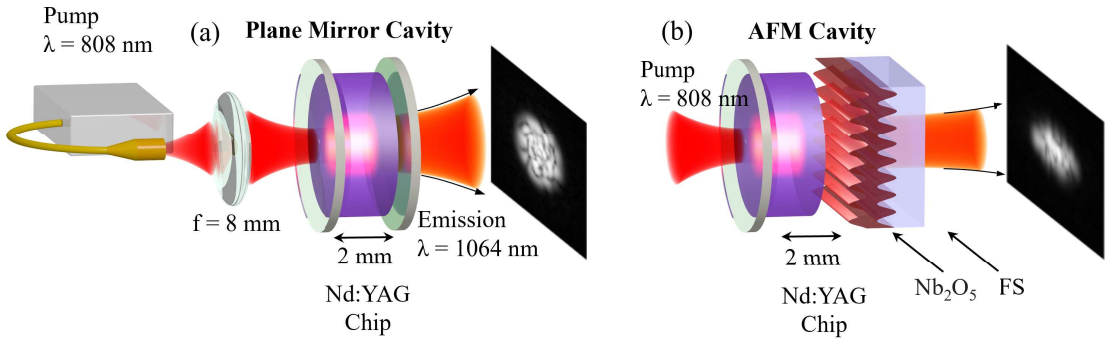


Figure 3.5: Conceptual scheme of microchip cavity with conventional output mirror, which, in high power regimes, emit the beam of poor spatial quality (a). McL with one conventional mirror replaced by angular filtering mirror (b). The angular filtering mirror filters in vertical direction (transversely to the direction of fringes), therefore, the resulting beam has reduced M_y^2 in that direction, and remains with the same M_x^2 in the horizontal direction.

We substitute one of the laser resonator mirrors by a Angular Filtering Mirror (AFM). In this specific case the reflectivity of the AFM is angle-sensitive in vertical direction (transversely to the direction of periodic fringes). AFM acts the same as the angular or spatial filter, but in reflection. It reflects the on-axis- components, whereas larger-angle -components are efficiently diffracted at the diffraction angle and experience higher losses in cavity. AFM performs the angular filtering without access to the far-field domain. This allows AFM to be ultra-compact,

only several micrometers thick.

AFM allows to keep the cavity design simple, because it replaces conventional output coupler and brings no additional intracavity element. It also allows the cavity to be ultracompact, where the rear mirror is coated directly on active material on one side, and AFM is attached from the other side. AFM technology is favorable to mass production and in the future can be cost efficient as it can be manufactured on large wafer and cut into small pieces similarly as microchip crystal are processed. The AFM efficiency can be further increased with 2D designs. On the other hand, the transmissive photonic crystal [159] is an additional element, which brings higher complexity to cavity, contains finite length, which could be limited factor in ultracompact design. The transmissive PhC [159] processing is time consuming, where each PhC is formed with femtosecond laser individually.

The resulting beam exhibits reduced quality factor M^2 and a twofold increase in laser brightness, achieved by applying angular filtering in only one direction.

3.2.1 Angular filtering mirror

In the current investigation, a structure was intentionally designed and fabricated to provide a maximal reflection coefficient for zero angle of incidence, and sharply decreasing reflection for (positive and negative) angles of incidence larger than 1 degree. In this way the structure was designed to work as AFM. The thin films have been fabricated by the ion beam sputtering method, depositing niobium oxide thin film on periodically modulated fused silica substrate (with gratings period – 625 nm and modulation amplitude around 200 nm) and replicating the nearly sinusoidal surface of the substrate. The grating period is close to the effective wavelength inside of the planar mode of the thin film (niobium oxide, with refractive index about 2.2). This means that the first diffraction maximum is at around the gliding angle, and the incident radiation efficiently couples into the waveguiding modes of the thin film. The coupling is very sensitive to the angle of the incidence of the incident

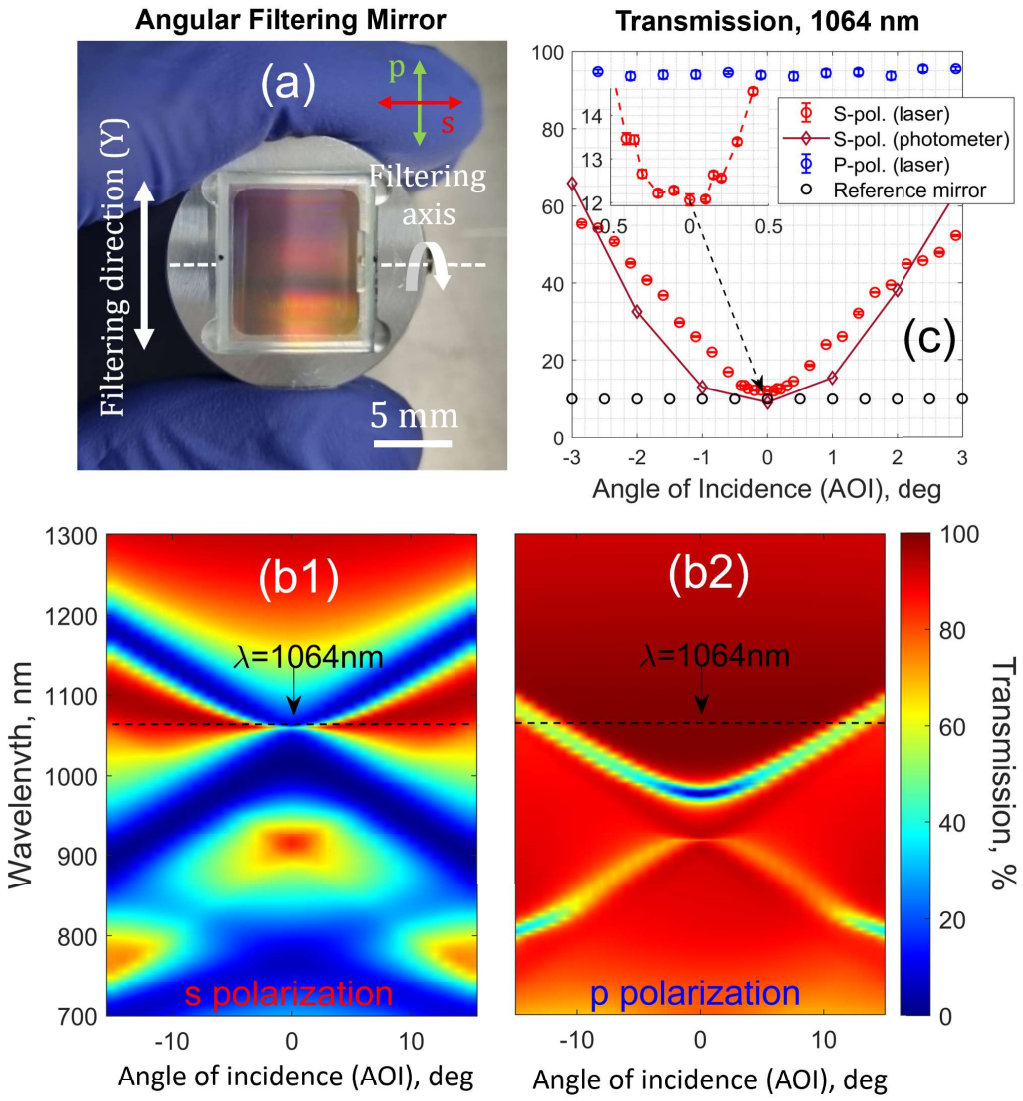


Figure 3.6: Angular filtering mirror used in the experiment with indicated filtering direction Y and polarization directions s and p (a). Experimentally measured transmission map of the filtering mirror in wavelength and angle of incidence (AOI) domains for s and p polarization directions (b1, b2). Experimentally measured transmission dependence on AOI (filtering axis Y) for two different polarizations at 1064 nm wavelength (c). Points (S-pol.(laser)) represent the transmission using s-polarized laser beam and the solid curve (S-pol.(photometer))- using an noncoherent spectrophotometer illumination (with the same s-polarization). Blue points (P-pol. (laser) represent transmission for p- polarized laser beam and hollow circles (Reference mirror) show transmission of conventional output coupler mirror used as reference.

beam, and eventually the reflection becomes very sensitive to that angle too. Therefore, the structure works as the angular filter. More technical

details of the fabrication of similar structures can be found in [191, 192]. As the angular filtering mirror is inserted in the laser cavity, higher-order modes with larger divergence are suppressed by the induced losses inside the resonator.

The AFM, which is used in our experiments, is depicted in Fig. 3.6(a). The transmission/reflection of AFM depends on the incidence angle in y direction (filtering direction) for one linear polarization direction (s), see Fig. 3.6(a). Its transmission dependence on wavelength and incidence angle (rotating the crystal in filtering plane (y,z), for s polarization) is presented in transmission map (Fig. 3.6(b)). AFM transmission dependence on incidence angle for lasing wavelength 1064 nm is shown in Fig. 3.6(c). We measured the transmission in Fig. 3.6(c) using two irradiation sources: laser T_s(laser) and spectrophotometer T_s(photometer). The two curves differ slightly from each other due to experimental artifacts, among others: considering finite input laser beam diameter ($\approx 3mm$ as a plain wave), limited laser stability, transmission variation along aperture area, also the limited angular resolution in spectrophotometer. As indicated by curve T_p(laser), the angular filtering mirror transmission is almost insensitive to incidence angle for p polarization. Also, the transmission for p and s polarizations does not vary significantly rotating around axis, perpendicular to filtering axis.

In our experiments maximum intensity inside the cavity was 50 kW/cm2, and no damage or degradation of AFM was recorded.

3.2.2 Experiment

The experimental setup is schematically shown in Fig. 3.6(b). We used 2 mm long Nd:YAG microchip crystal of 2% molar doping. One crystal facet was coated with high reflective coating for 1064 nm wavelength and high transmission for 808 nm wavelength. The other facet was coated with an anti-reflection coating for 1064 nm and the output coupler was placed directly behind the crystal, where the total cavity length was 2,1 mm. The crystal face dimensions were 3x3 mm^2. The crystal was wrapped in the indium foil and placed in the copper holder, which was

actively cooled to room temperature.

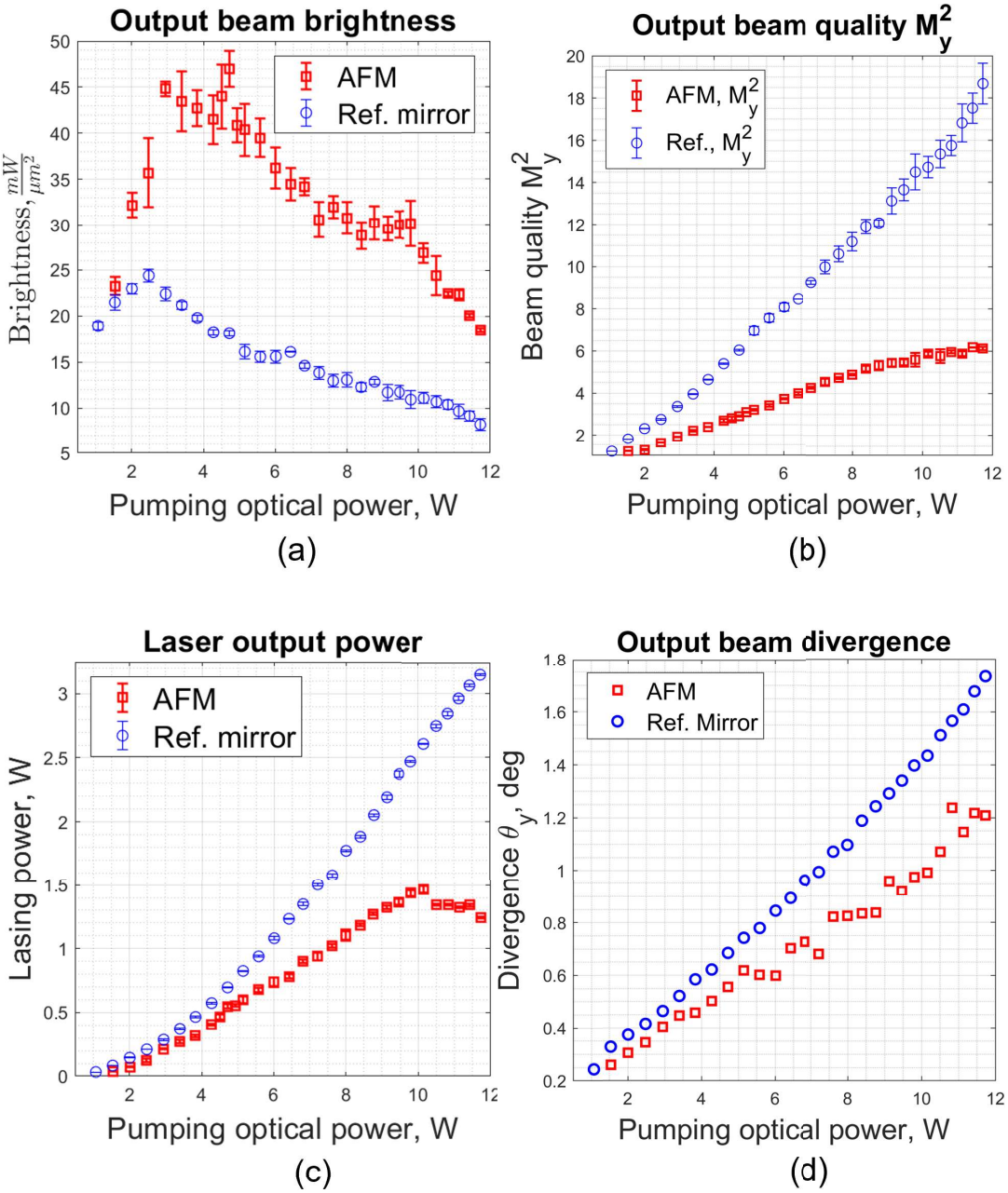


Figure 3.7: Experimentally measured laser brightness (a), beam quality (b), output power (c) and divergence (d) dependence on pumping power, when AFM and reference mirror are used as output couplers.

The AFM was placed next to the crystal facet using a separate holder and micro screw. Crystal was longitudinally pumped by multi-mode 808 nm diode coupled from the fiber of $100\mu m$ core diameter. The pumping beam was focused with the aspherical lens with focal length 8mm to $\approx 240\mu m$ diameter spot on the crystal. The distance between the fiber

end and the lens was 18 mm, while the distance between the lens and the crystal was 13 mm. Pumping power was available up to 12 W. The crystal absorbed 53% of pumping power due to its limited length and doping.

In the experiment, we compared the laser performance using two different output coupler mirrors: in one case - an AFM, and in another a usual reference dielectric mirror. The reflection coefficient of the reference mirror $R = 90\%$, was chosen very close to the reflection of AFM for zero incidence angle. We measured laser brightness (Fig. 3.7(a)), beam spatially quality M^2 (Fig. 3.7(b)) and output power (Fig. 3.7(c)) depending on the pumping power, and each was compared with the case of a reference mirror.The beam quality was estimated by measuring the beam diameters around the beam waist with a CCD camera and fitting the M^2 parameter, in accordance with the ISO 11146 standard [193].

The laser beam diameter on output coupler was 190 μm using usual mirror and 210 μm with AFM when working close to the threshold. As evident from Fig. 3.7(d) due to the minor divergence (0.2°) at the threshold, where the AFM has small ($< 0,5\%$) reflection changes (Fig. 3.6(c)), the filtering is very weak. Increasing the pumping power up to 12 W, the divergence grows to 1.8°and the AFM becomes very sensitive to such AOI. Even in the range of 2-5 W pumping, the AFM reflection decreases by about 3%, corresponding to AOI = 0.6°. The reflection change of 3% for non-collinear wave brings extra losses, so this condition favors lower-order modes. Consequently, one gets less power in the emission, however the spatial quality of the beam increases, as evidenced in Fig. 3.7(b). The parameter of merit, that evaluates the trade-off between power and beam quality is brightness. Multimode beam brightness can be adequately estimated using the formula $B = \frac{P}{M_x^2 M_y^2 \lambda^2}$ [148], where P is laser average output power, M_x^2 and M_y^2 are beam quality in x and y directions (following ISO standard [193]), λ is the wavelength. The picture Fig. 3.7(a) indicates that maximum brightness is achieved with AFM. It is higher by factor 2 compared with conventional output mirror. The brightness reaches its maximum at a pumping power 4 W and starts

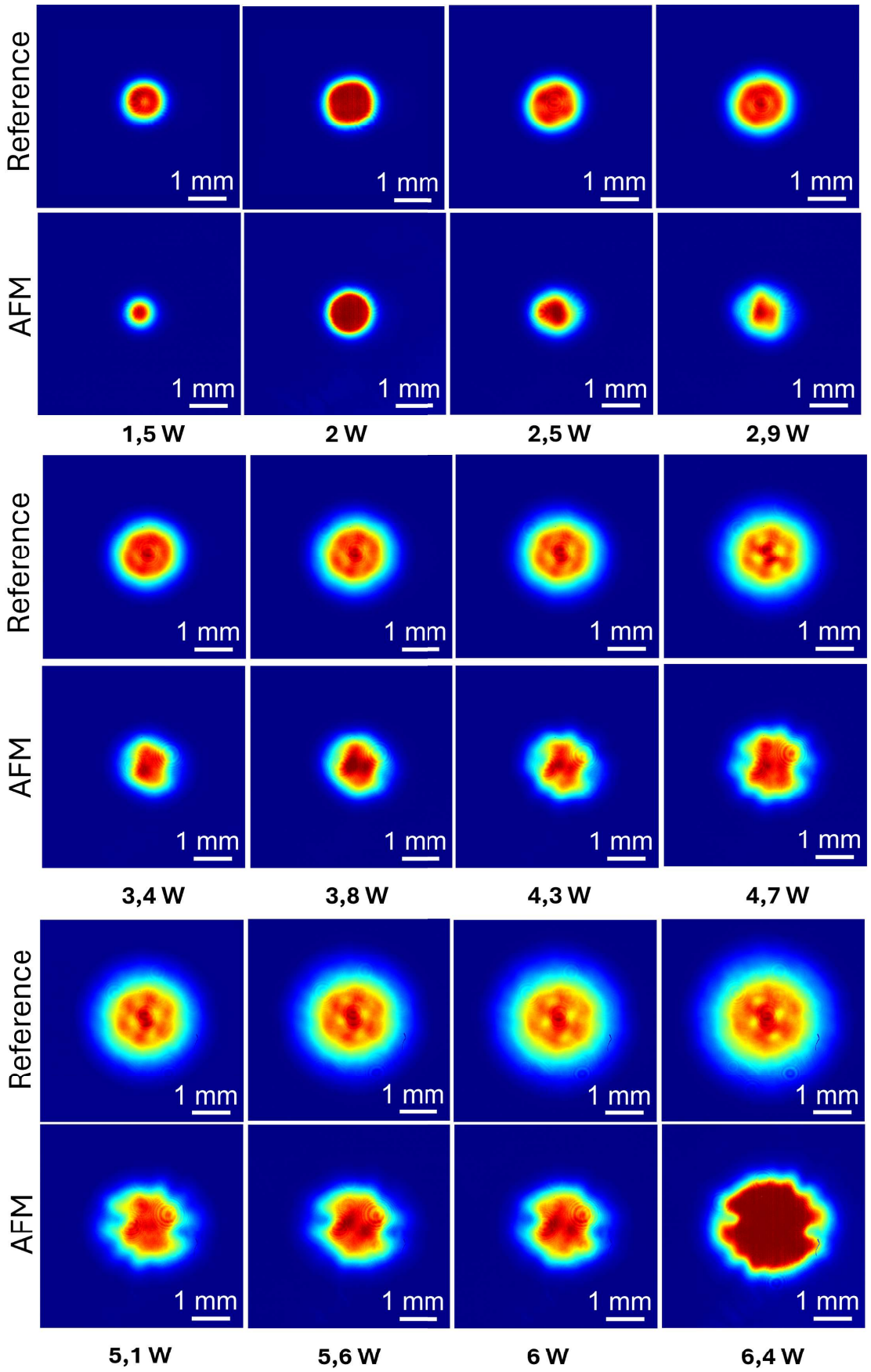


Figure 3.8: Far field beam profiles with AFM and reference mirror when pump power varies in the range 1,5-6,4 W

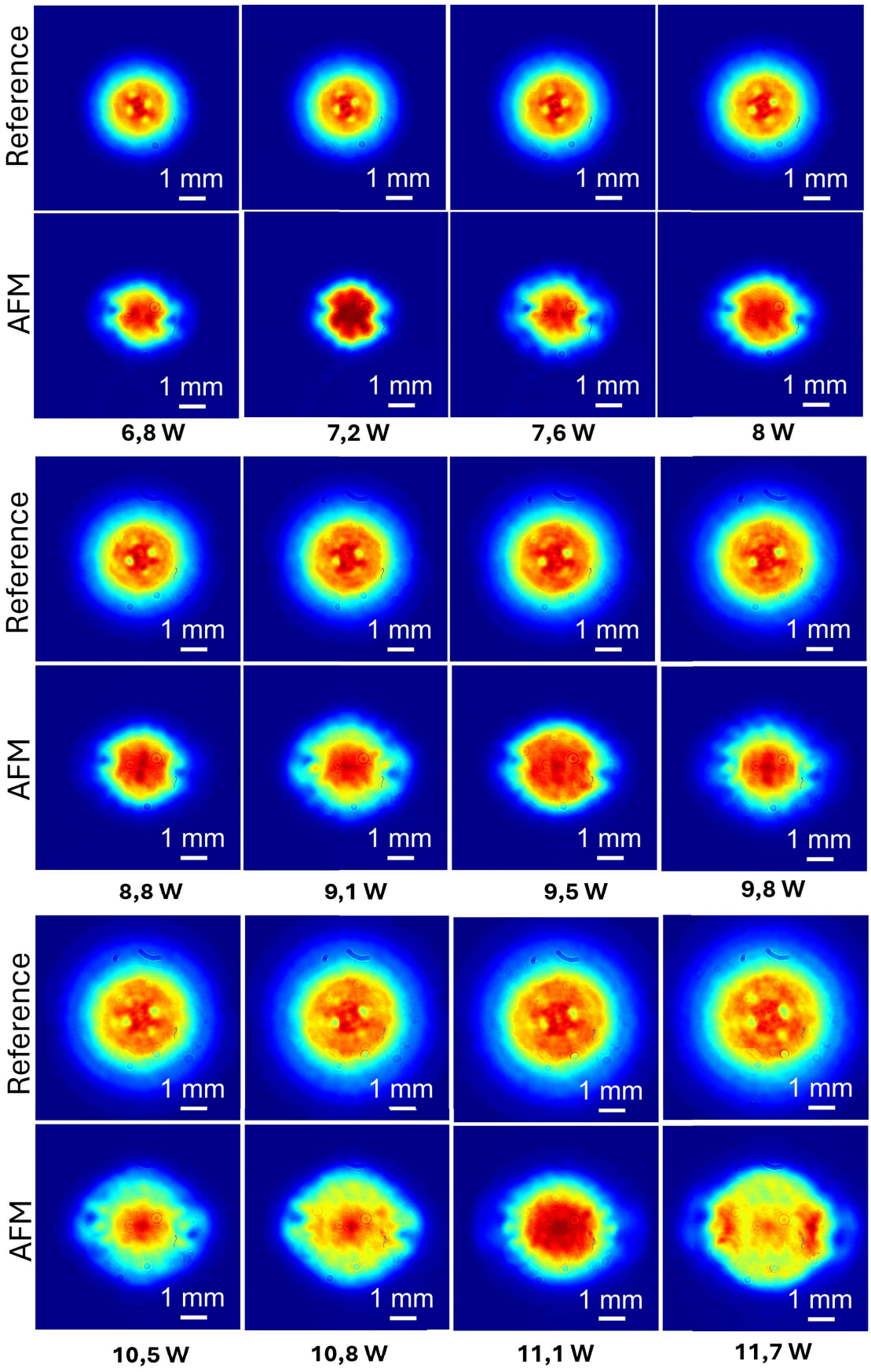


Figure 3.9: Far field beam profiles with AFM and reference mirror when pump power varies in the range 6,4-11.7 W

to decline by further increasing the pumping power. This behaviour could be interpreted taking into account that brightness linearly depends on the output power and inversely on second power of beam quality factor (M^4), whereas the experimental data shows that both the output power and the beam quality (M^2) depend linearly on the pump power.

The optical-to-optical efficiency is 28% for a microchip with the usual output coupler and 20% for a microchip with AFM, at the pumping power, where the brightness is highest (4.28 W pumping). The calculation takes into account only the absorbed light in the cavity.

3.2.3 Output beam profile Dynamics in Far and Near Field

Figures 3.8, 3.9, 3.10, 3.11 depicts the beam profiles in far and near field domains at several pumping powers, using both AFM and conventional mirror as the output coupler. As expected, the beam shapes become elliptical in far and near fields using AFM at higher pumping due to spatial frequency filtering. It corresponds to the fact that measured beam quality in filtering direction (y) is improved. One should note that with the increase of pumping power, more transverse modes become above the threshold, and the overall transverse distribution (which is a collection of many modes) becomes broader. Angular filtering creates higher losses for higher order modes and reduces the beam broadening effect. The far-field beam diameter increases more significantly than the near-field diameter with increasing pump power. This is due to thermal lensing and gain guiding effects, which cause the transverse modes to contract in the near field as the pump power increases [6]. The beam divergence continuously increases (Fig. 3.7(d)) for each mode (including fundamental), causing higher losses in cavity with AFM. At a certain point, around 10W of pump power, the increase in losses surpasses the increase of gain, leading to a decline in output power (Fig. 3.7c).

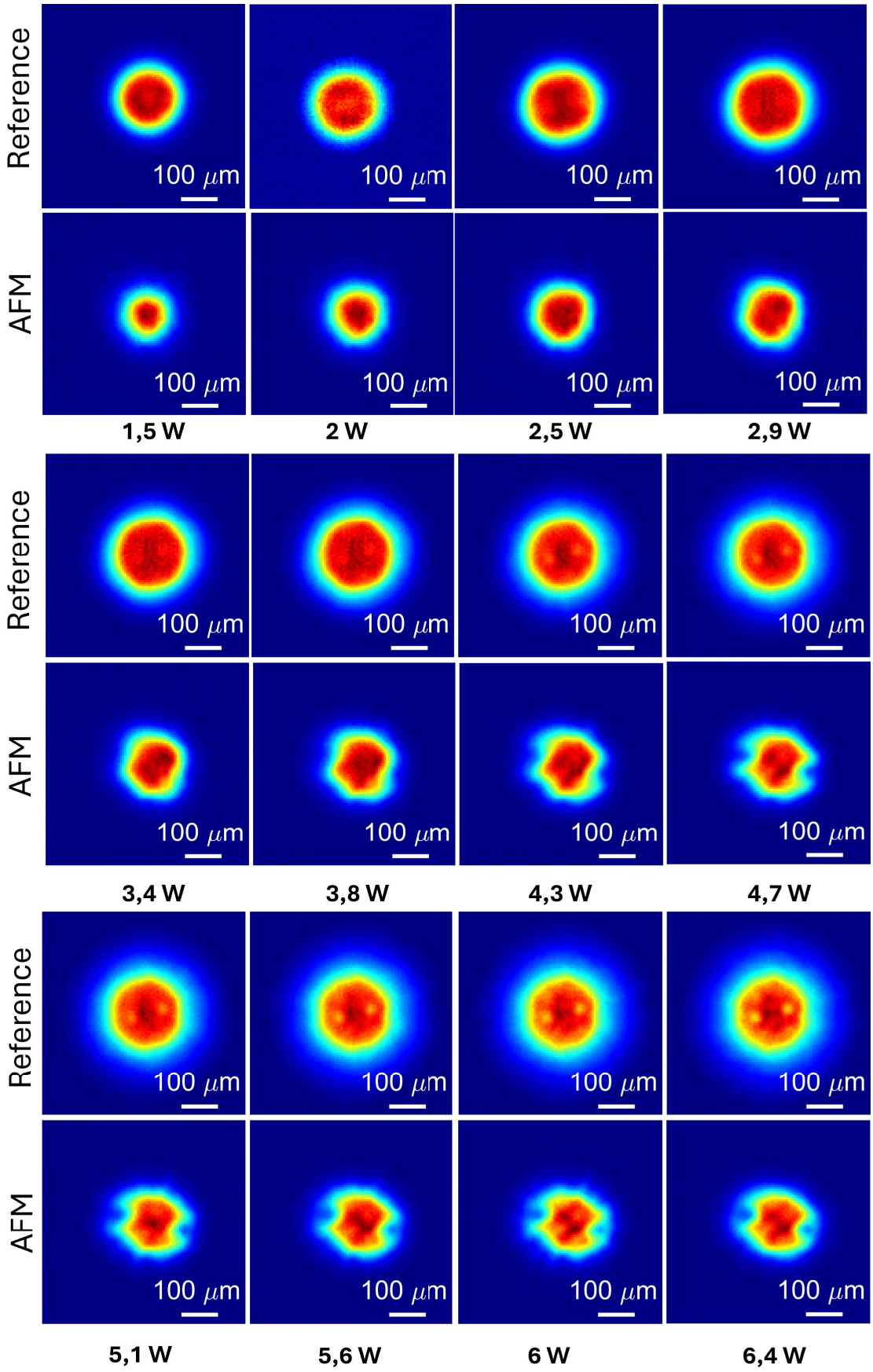


Figure 3.10: Near field beam profiles with AFM and reference mirror when pump power varies in the range of 1,5-6,4 W

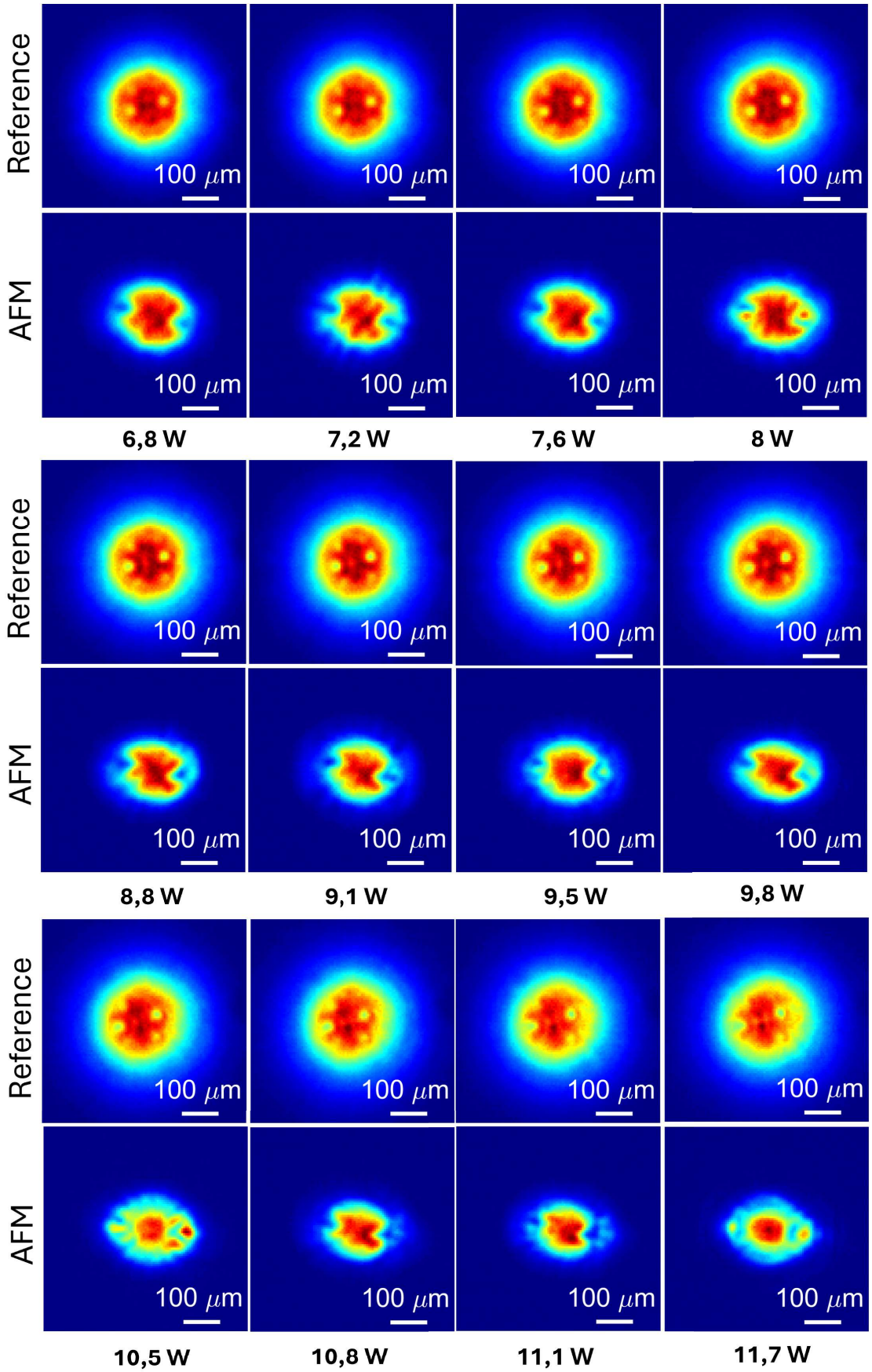


Figure 3.11: Near field beam profiles with AFM and reference mirror when pump power varies in the range of 6,4-11.7 W

3.2.4 Numerical Simulations

In order to justify the experimental observations, also to highlight the universality of our observations, we performed numerical simulations of the McL with- and without the AFM. We numerically integrated the Maxwell-Bloch Equation (MBE) system, valid for Class B microchip laser[132, 194], [143, p. 118], and [142, p. 36]:

$$\frac{\partial E}{\partial t} = \left[-(1+i\omega_0) + ia\nabla_\perp^2 + iV(\mathbf{r}_\perp) + \hat{F}(\nabla_\perp)\right] E + P\,, \tag{3.13a}$$

$$\frac{\partial P}{\partial t} = -\gamma_\perp (P - ED), \tag{3.13b}$$

$$\frac{\partial D}{\partial t} = -\gamma_\parallel \left(D - D_0(\mathbf{r}_\perp) + \frac{EP^* + E^*P}{2}\right), \tag{3.13c}$$

where the slowly varying electrical field complex amplitude (envelope) $E(\mathbf{r}_\perp, t)$, the material polarization $P(\mathbf{r}_\perp, t)$, and the population inversion $D(\mathbf{r}_\perp, t)$ are defined in two-dimensional transverse space $\mathbf{r}_\perp$ and evolve in time. $D_0(\mathbf{r}_\perp)$ is the unsaturated (pump induced) population inversion. Time is normalized to photon life time $\tau = \frac{2L}{c(T+\delta)}$, L being the length of the resonator, T is the output coupler transmission (0.1 in our case), δ cavity losses per round trip (experimentally measured $\delta = 0.017$). Photon lifetime in experiment was $\tau \approx 0.1ns$. Diffraction coefficient $a = \frac{L\lambda}{2\pi(T+\delta)}$ scales the transverse space (in experiment $a \approx 2 \times 10^3 \mu m^2$). ω_0 is the resonance detuning from the gain line center, $\gamma_\perp$ is the material polarization relaxation rate, which corresponds to Nd:YAG gain linewidth $\approx$ 100 GHz [16] and ,when normalized to photon relaxation rate, is typically of order of 10. Population inversion decay rate $\gamma_\parallel$ corresponds to Nd:YAG fluorescence lifetime $\approx 230\mu s$ and is typically of order of 10^{-6} (normalized to photon relaxation rate). $V(\mathbf{r}_\perp)$ is the confining potential in transverse space (in McL we considered thermal lensing, where refraction index follows the pump profile $V(\mathbf{r}_\perp) = \alpha \cdot D_0(\mathbf{r}_\perp)$. The filtering function of AFM is introduced phenomenologically by the operator $\hat{F}(\nabla_\perp)$ providing the far-field transmission profile $\log\left(\hat{F}(k_\perp)\right)$, and matching the experimentally measured AFM angular transmission.

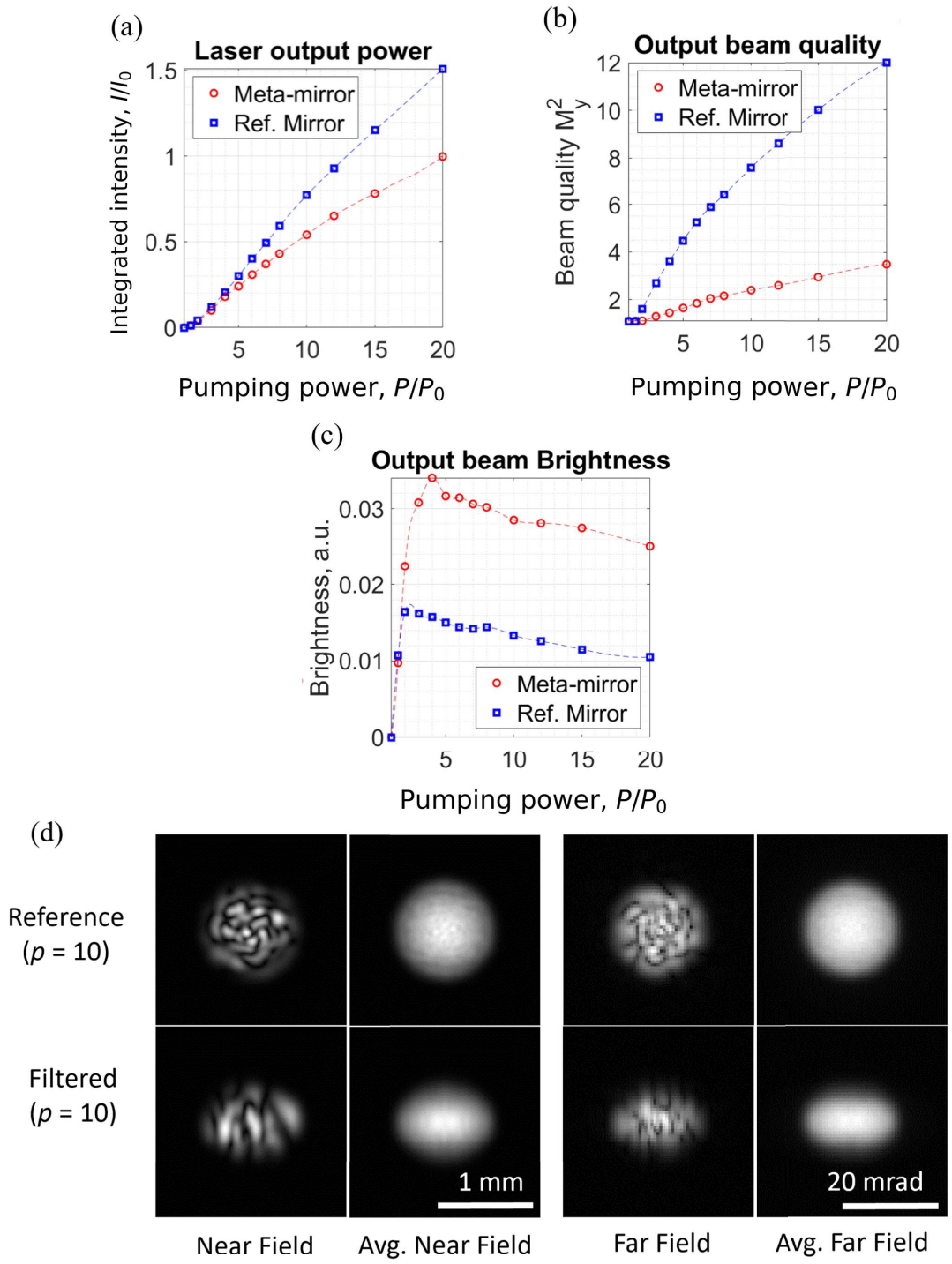


Figure 3.12: Summary of numerical simulations of McL with AFM: (a) shows the emission power, (b) the M^2 and (c) the brightness of the emitted beam, depending on the pump power. The blue lines represent the reference case with no angular filtering, where the red graph corresponds to resonator with AFM. The near- and far-field beam profiles as well as averaged near and far-field profiles at a particular pump value ($p = 10$) are shown on inserts: the near field window corresponds to 2x2 mm, and far field windows - to 40x40 mrad.

Due to mounting strain and heat accumulation in the active media [153, 195], the beam experiences birefringence and intercoupling between polarization states. These effects were not included in our numerical calculations.

The results (beam intensity, M^2 and brightness) are presented in Fig. 3.12, where the blue circles correspond to the case in presence of AFM, and red squares – to the reference cases without angular filtering. We have chosen the parameters of angular filtering function coinciding maximally with that of the experimental sample. The beam quality parameter M^2 was estimated using the method outlined in Section 4.3.2. This involved numerically integrating the first and second moments of electrical field E, as well as the A and B auxiliary integrals. The tendencies show the same qualitative features as in experiment (compare with Fig. 3.7). The emitted power with AFM was of the level of 70% from the reference laser. The M^2 reduced several times, and the brightness maximally increased around two times.

3.2.5 Summary

An enhancement of the beam-quality factor M^2 and brightness in microchip-laser radiation was demonstrated by employing an angular-filtering mirror in place of a conventional plane-mirror outcoupler. For that purpose we designed and fabricated the angle filtering mirror - a nano-modulated thin film structure with the reflectance strongly dependent on the incidence angle. In our experiment, we observed an increase of brightness by approximately two times. The numerical simulations of single-longitudinal-mode approximation support this experimental result, and give a hint on the universality of this result. It should be noted that 2D angular filtering is not restricted to this twofold increase of brightness.

Demonstrated approach differs from alternative approaches in that it neither introduces additional alignment requirements, such as with apertures or gradient mirrors, nor limits the low-order transverse mode size by additional diffraction losses (clipping). Its novelty and properties

arise from the selectivity mechanism realized by Fano-like resonances occurring in periodically modulated surface gratings.

3.3 Polarization Filtering in Nd:YAG Microchip Laser

Publication directly related to this dissertation section:

Matas Plukys, Lina Grineviciute, Julianija Nikitina, Darius Gailevicius, and Kestutis Staliunas, "Polarization enhancement in Nd:YAG microchip laser with Meta-Mirror output coupler," *Optics Letters*, vol. 50, pp. 4666–4669, 2025. https://doi.org/10.1364/OL.566958

*(Selected as an **Editor's Pick**)*

In this section we present a novel design of a polarizing Meta-Mirror and implement it in combination with polarized pumping in an Nd:YAG McL to enhance the laser's polarization contrast ratio (see Fig. 3.13). We systematically compare the individual and combined effects of these two techniques in different pump power regimes to clarify their respective contributions to polarization contrast enhancement. We identify a distinct pump threshold beyond which polarized pumping alone becomes inefficient. Beyond this threshold, the meta-mirror continues to enhance polarization contrast without introducing additional losses, while simultaneously improving beam quality and brightness. Additionally, this setup improves beam quality, output power, and overall brightness.

The Nd:YAG monocrystal exhibits slight birefringence as a result of mechanical stress imposed by the crystal holder. Consequently, the orthogonal polarization states experience slightly different refractive indices, leading to a small difference in optical path lengths. This difference allows two sets of longitudinal modes to coexist [174–176]. The orientation of the orthogonal polarization states is determined by the geometry of the crystal holder and, in our case, aligns with the direction of the applied mechanical pressure (see Fig. 3.16(c)). Additionally, the

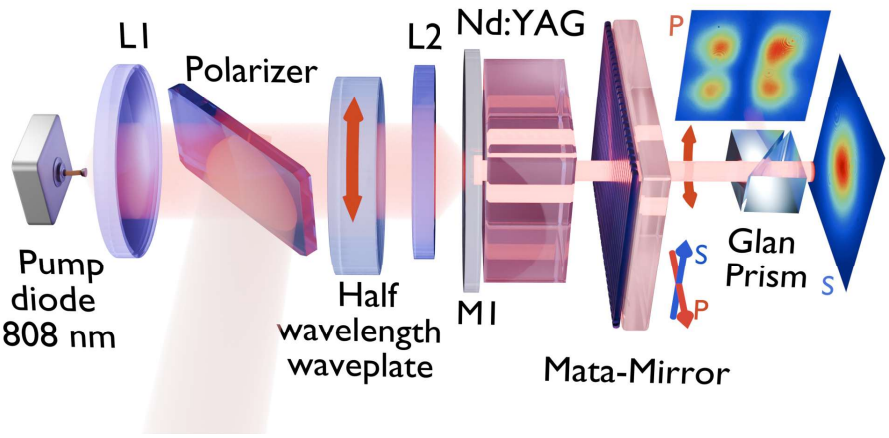


Figure 3.13: Conceptual schematic of a microchip cavity with a Meta-Mirror, enabling controlled pumping polarization contrast and direction (a). Key components include L1 (50 mm collimation lens), W1 (808 nm half-wave plate for polarization control), L2 (50 mm focusing lens), and M1 (high-reflectivity cavity rear mirror at 1064 nm, transmissive at 808 nm). The study examines the effects of pumping polarization, Meta-Mirror rotation, and crystal holder geometry on the output polarization contrast (b).

gain in Nd:YAG is anisotropic and depends on the polarization direction of the pump[174]. When the pump polarization aligns with one of the orthogonal polarization eigenstates, the gain for that state increases, resulting in linearly polarized laser output. The meta-mirror, on the other hand, functions as a polarizing output coupler at normal incidence (AOI = 0). It strongly reflects the S-polarized component while transmitting the orthogonal P-polarized component (see Fig. 3.16). This effectively raises the lasing threshold for the P polarization, thereby favoring the generation of the S-polarized state.

We investigate polarization contrast enhancement by employing the meta-mirror at various rotation angles (see Fig. 3.16(c)), such that the S and P polarization states either align with or deviate from the intrinsic orthogonal polarization axes of the laser crystal. Additionally, we vary the pump polarization direction to either coincide with or differ from both the meta-mirror polarization axes and those of the crystal. Experimental data are presented to evaluate the effects under different configurations,

and we provide insights into the dominant mechanisms contributing to polarization contrast enhancement across a range of pump power levels in Nd:YAG microchip laser cavity.

3.3.1 Polarizing Meta-Mirror

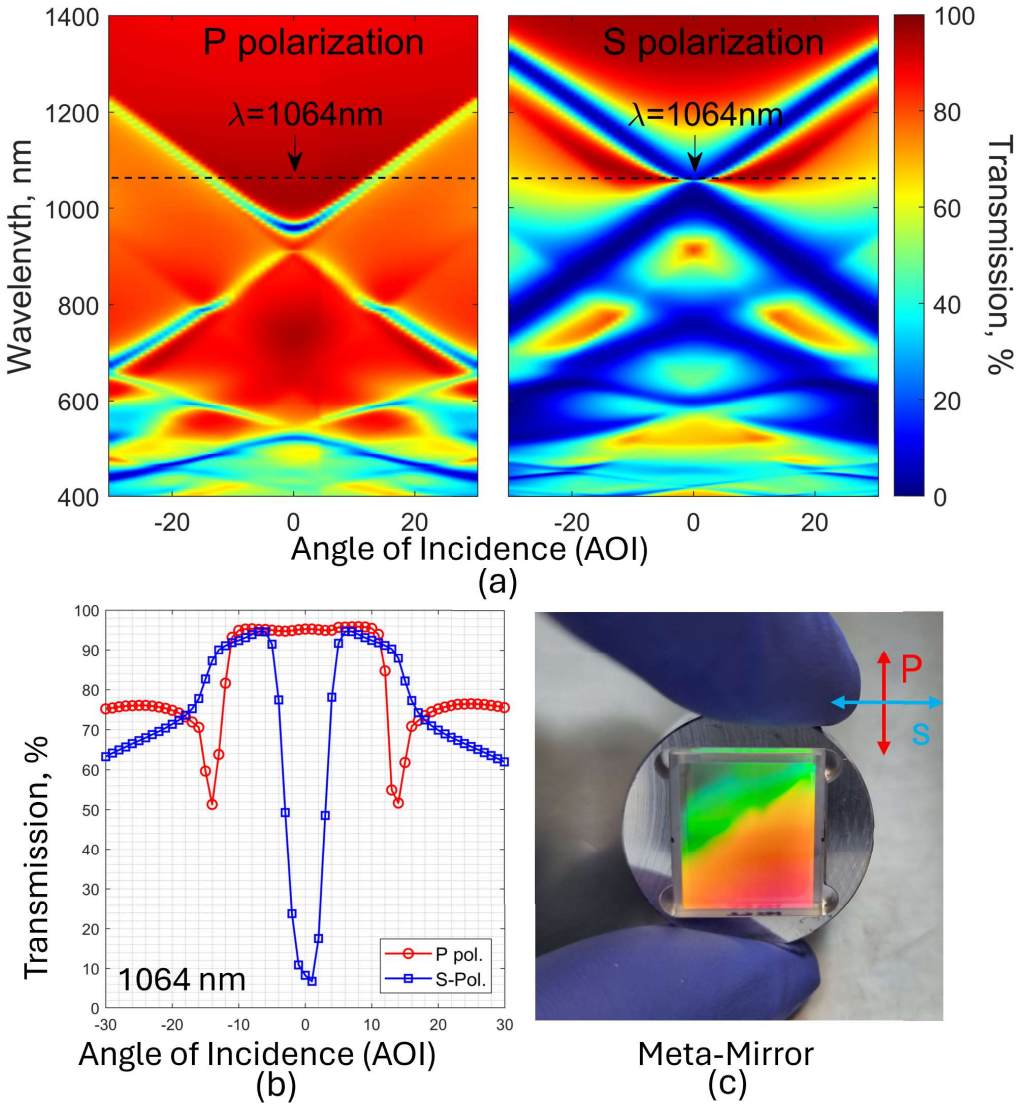


Figure 3.14: Meta-Mirror transmission maps for S- and P-polarized light as functions of angle of incidence (AOI) and wavelength (a). Transmission graph at 1064 nm showing dependence on AOI for both S- and P-polarizations (b). A photograph of the Meta-Mirror, with S- and P-polarization directions indicated (c).

We designed and developed special Meta-Mirror for use as an polarizing output coupler in a Nd:YAG microchip cavity to enhance polarization contrast at high-power regimes. The design is based on recent observa-

tion[173], where the Fano-like resonances in nanostructured thin films enable a sharp reflection change for S and P polarizations while working at AOI=0. We characterize this Meta-Mirror by frequency and angular selectivity of light transmission through the structure (see Fig. 3.14(a)).

The Meta-Mirror was intentionally designed and fabricated to provide a maximal reflection coefficient for S polarization ($R_s > 90\%$) and minimum reflection for P polarization ($R_p < 5\%$) at 1064nm wavelength and AOI=0 deg (see Fig. 3.14(b)), in order to maximize the polarization contrast. Polarization directions S and P are indicated in Fig. 3.14(c). The achieved distinction between S and P polarizations $\Delta R = R_s - R_p = 85\%$ is significantly higher than so far demonstrated in resonant gratings [153, 183], anisotropic nano-structured thin films [184, 185] and anisotropic grating mirrors [186], where the reported ΔR are 10, 40 and 45% accordingly. Polarizing Meta-Mirror does not introduce any absorbtion losses, which were reported in anisotropic nano-structured thin films [184]. Here reported S polarization reflection contains gentler dependence on AOI (see Fig. 3.14(b)) than reported angular filtering mirror in [4], in order to diminish the angular filtering and highlight the polarizing effect.

The thin films have been fabricated by the ion beam sputtering method, depositing niobium oxide thin film on periodically modulated fused silica substrate (with gratings period – 625 nm and modulation amplitude around 200 nm) and replicating the nearly sinusoidal surface of the substrate. The grating period is close to the effective wavelength inside of the planar mode of the thin film (niobium oxide, with refractive index about 2.2). This means that the first diffraction maximum is at around the gliding angle, and the incident radiation efficiently couples into the waveguiding modes of the thin film. More technical details of the fabrication of similar structures can be found in [191, 192]. In our experiments maximum intensity inside the cavity was 50 kW/cm2, and no damage or degradation of Meta-Mirror was recorded.

3.3.2 Laser Parameter Experimental Investigation

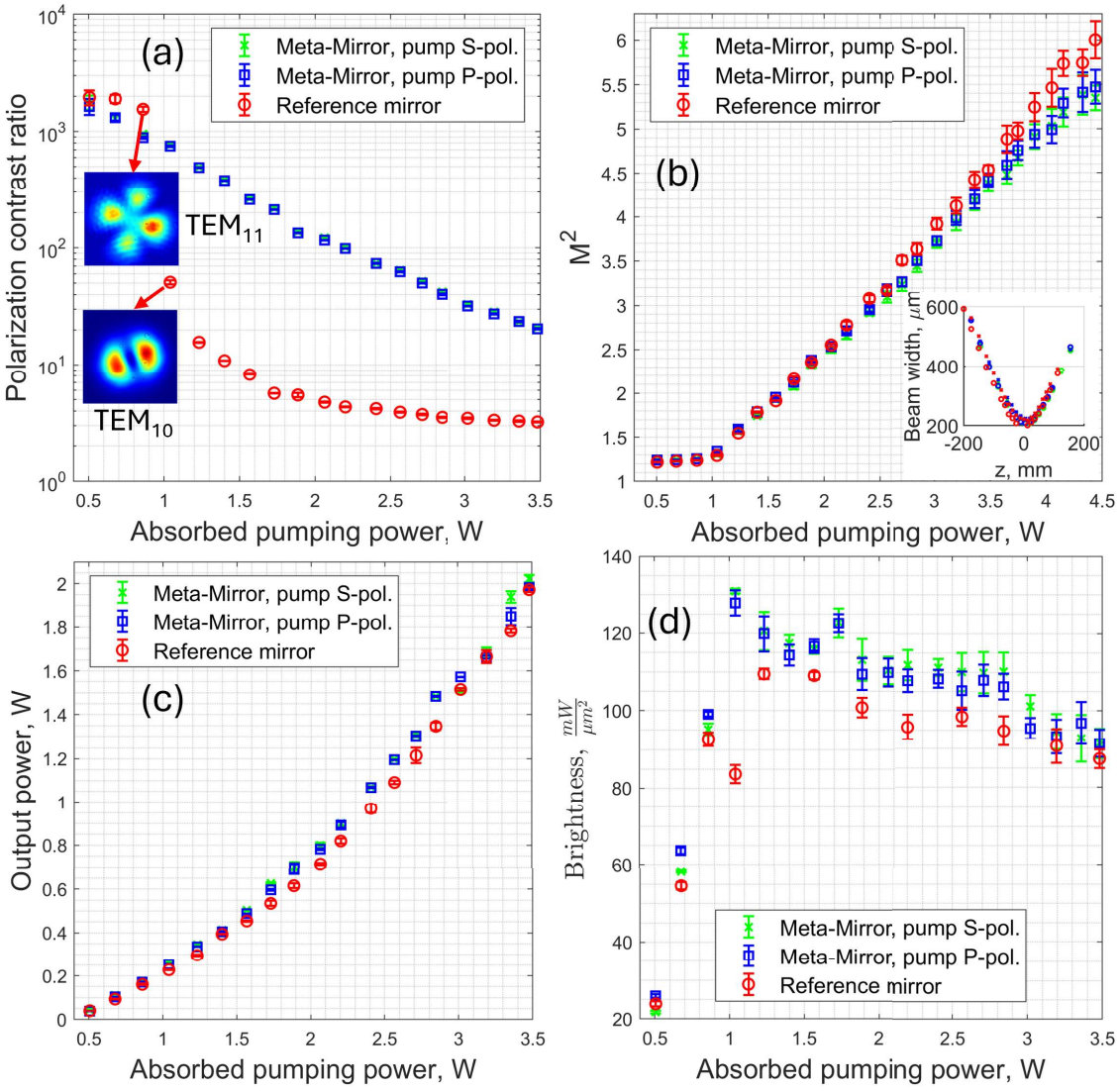


Figure 3.15: Dependence of pol. contrast ratio (a), beam quality factor M^2 (b), laser output power (c) and brightness (d) on P_{abs}. Measurements were performed for both cases where the pumping pol. direction aligns with the MM's S- and P-polarizations. For the reference mirror, the pumping pol. is optimized for max. output pol. contrast. The profile images in insets of (a) illustrate a sudden drop in pol. contrast and shift in profile shape (P-pol.) around $P_{abs} \approx 1$W when the reference output coupler is used. The inset of (b) shows the beam width dependence on propagation distance, when $P_{abs} = 1.4$W.

The experimental setup is schematically shown in Fig. 3.13(a). We used 2 mm long Nd:YAG microchip crystal of 2% molar doping. The one crystal face was coated with high reflective coating for 1064 nm wavelength and high transmission for 808 nm wavelength. The other

crystal face was coated with an anti-reflection coating for 1064 nm. The crystal face dimensions were 3x3 mm^2. The crystal was wrapped in the indium foil and placed in the copper holder, which was actively cooled to room temperature. The Meta-Mirror was placed in 3 mm from the crystal face using a separate holder and micro screw. Crystal was longitudinally pumped by multi-mode 808 nm diode coupled from the fiber of $100\mu m$ core diameter. The pumping beam was collimated with 50 mm lens and went through Brewster angle polarizer. The pumping polarization contrast achieved was 1:300. Polarized pumping went through L/2 waveplate at 808 nm, which was rotated on motorized stage, allwing to change the pumping beam polarization angle in the range of 0-360 degrees. With 50 mm lens the pumping beam was focused to $\approx 300\mu m$ diameter spot on the Nd:YAG crystal. Pumping power was available up to 12 W. The polarization contrast was measured by glan-prism separating S and P polarization due to internal reflection allowing 1:100000 polarization contrast, which is two orders higher than measured max. polarization ratio of laser beams in experiment.

We investigated the output beam polarization contrast ratio, beam quality factor (M^2), output power and brightness dependence on absorbed pumping power in the laser crystal (see Fig. 3.15). We compared three most extreme regimes: (1) Meta Mirror used as output coupler when pumping polarization coincides with S polarization (green curve); (2) Meta Mirror used as output coupler when pumping polarization coincides with P polarization (green curve); (3) Usual isotropic output coupler with reflectance very close to S polarization in Meta-mirror (R=90%) when pumping polarization is aligned with orthogonal polarization eigenstate in laser crystal. Generation threshold was very similar for all three cases at 0.5W absorbed pump power (Fig. 3.15(c)). The output power was highest with Meta-mirror and pumping aligned with S-pol., where the anisotropic gain stronger component coincides with the polarization supported by Meta-Mirror in cavity. Rotating the pump polarization from S to P, the output power drops continuously and is smallest when reaching P-pol, but it is still higher than with isotropic reference mirror. Polarization

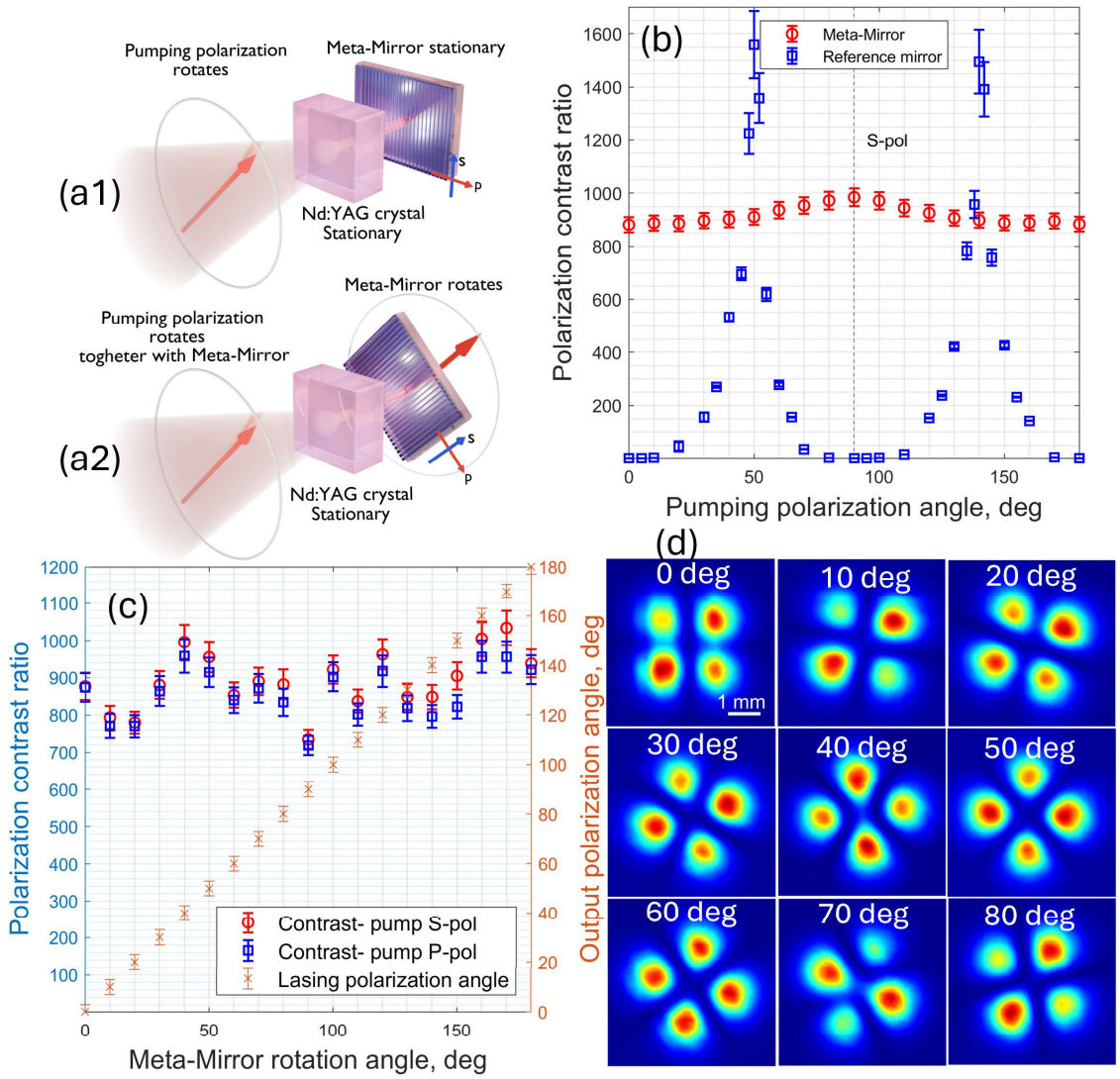


Figure 3.16: Laser polarization contrast as a function of pump polarization angle and Meta-Mirror (MM) rotation is shown for an absorbed power of $P_{abs} = 0.86$. Figures (a1) and (b) illustrate the case where only the pump polarization is rotated. Figures (a2) and (c) show the case where the MM is rotated together with the pump polarization vector. Figure (d) presents the P-polarized beam pattern, while figure (c) also shows the lasing polarization angle as a function of MM rotation.

contrast ratio is highest at generation threshold (see Fig. 3.15(a), 1:2000 for isotropic reference mirror, 1:1800 for Meta-mirror with S-pol. pump, 1:1700 for Meta-mirror with P-pol. pump) and drops when pump power is increased due to heat accumulation and stress in the active media [153, 195] leading to depolarization. With Meta-mirror the contrast ratio drops gradually when increasing the pump power, but with isotropic mirror the contrast drops dramatically at around 1 W of absorbed pump power,

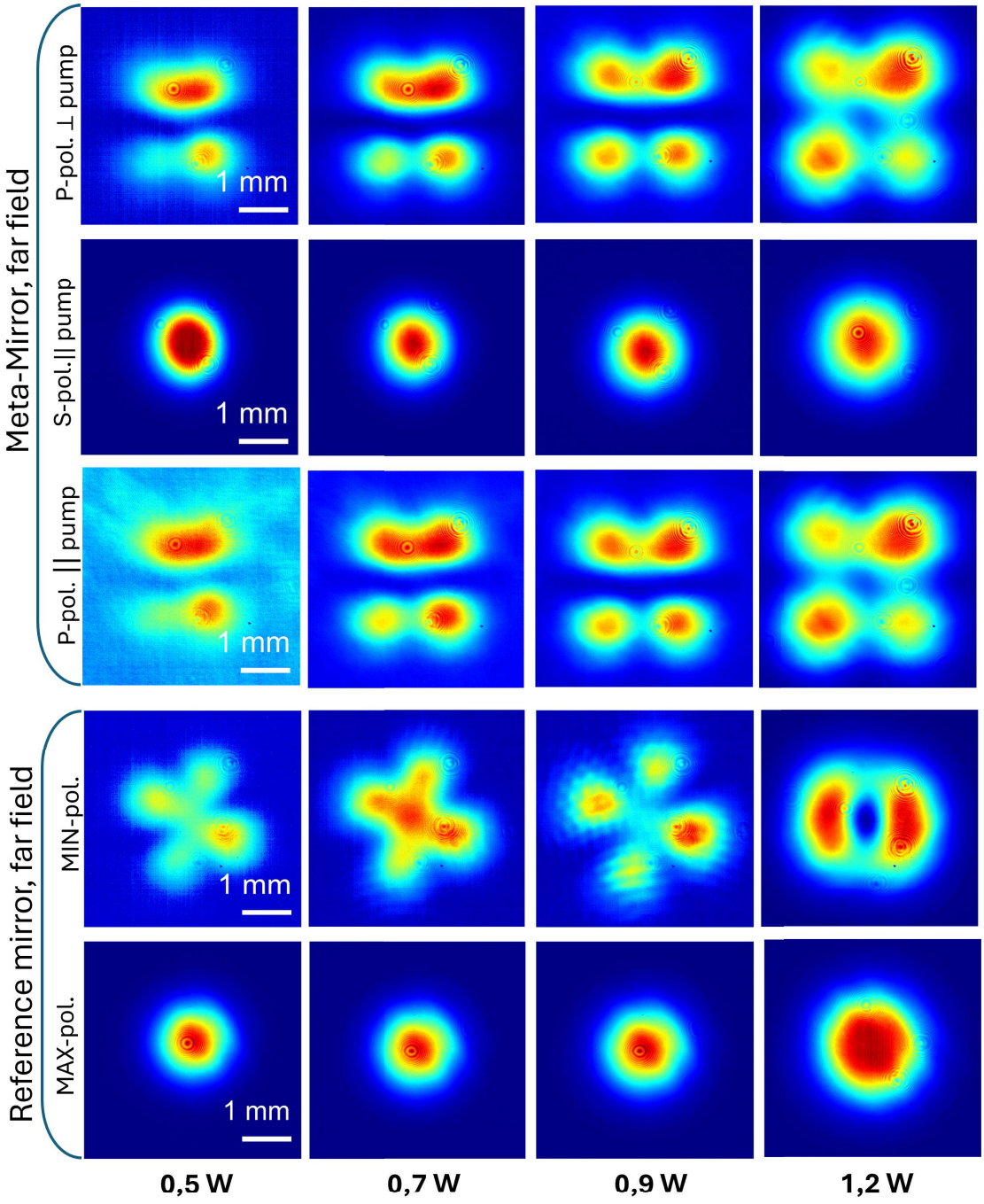


Figure 3.17: Far field beam profile shapes at various P_{abs} (0,5–1,2 W) captured at a distance of 18 cm from the cavity.

where the mode shape of weaker polarized component changes from 11 to 10 (see Fig. 3.15(a)) and becomes much stronger. After passing the 1W threshold, only Meta-mirror approach keeps the beam polarized. Due to slightly higher output power and better beam quality (Fig. 3.15(c,b)), the Meta-Mirror appliance leads to higher brightness (Fig. 3.15(d)), where the pump polarization alignment with S-pol. leads to further brightness

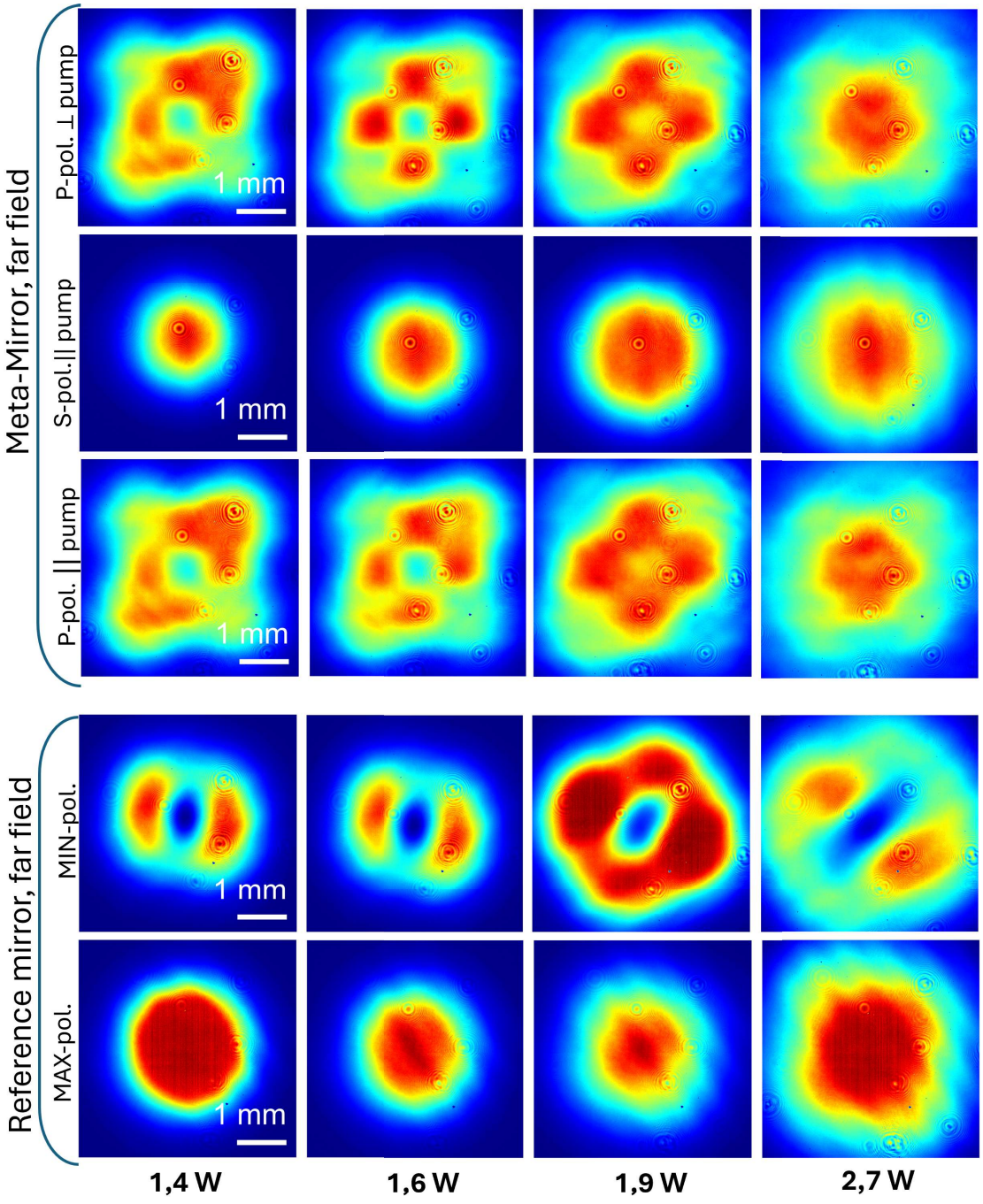


Figure 3.18: Far field beam profile shapes at various P_{abs} (1,4–2,7 W) captured at a distance of 18 cm from the cavity.

improvement.

We measured the polarization contrast ratio dependence on pumping polarization angle, when the absorbed pumping power was set just before the 1W threshold (see Fig. 3.17(a)). As graph indicates, the contrast ratio is very sensitive to pumping polarization direction, when using isotropic mirror, where it can vary from fully depolarized to 1:1600. The curve is

steepest in proximity of laser crystal orthogonal states, which are 90 deg. from each other. Slightly change in pumping polarization direction or shift in orthogonal state position due to thermo-mechanical perturbation could lead to sharp polarization contrast drop. On the other hand, the Meta-Mirror cavity is much less sensitive to pumping polarization, where the min. and max. values are 900 and 1000 when rotating the pumping polarization 180 degree. When rotating the Meta-Mirror in accordance to crystal orthogonal states (see Fig. 3.17(b)), the polarization contrast appears to be not very sensitive, where the laser output polarization direction strictly follows S-polarization direction dictated by Meta-Mirror. The Meta-Mirror primarily determines the polarization contrast, while the pumping polarization direction and the orthogonal states of the laser crystal also play significant roles (see Fig. 3.17(c)). When the Meta-Mirror is rotated around the optical axis, the pattern of the weaker polarization mode 11 rotates by the same amount (see Fig. 3.17(d))).

We investigated the beam shapes of both orthogonal polarizations (S and P) when varying the pumping power (see Fig. 3.18). The depolarizing P mode shape is symmetrical to Meta-Mirror (Fig. 3.18(a-f)) axis or to laser crystal orthogonal states (Fig. 3.18(g-l)), when using isotropic mirror (it coincides with crystal holder symmetry in Fig. 3.17(c)). Stronger S-polarization shape is less influenced by Meta-Mirror or orthogonal states and is close to Gaussian (Fig. 3.18(m-r)). By increasing the pump power, the both orthogonal polarizations become multi-mode.

3.3.3 Discussion

During the experiments, a slightly higher polarization contrast ratio was observed for the isotropic mirror under polarized pumping than for the meta-mirror when operating near the generation threshold (see Fig. 3.15(a)). Several factors may account for this behavior:

1. The meta-mirror exhibits a relatively high transmission at the pump wavelength (808 nm), transmitting approximately 20% for S polarization and about 90% for P polarization. In contrast, the

reference mirror is specified by the manufacturer to transmit less than 10% at 808 nm. To suppress the pump contribution to the measured polarization contrast ratio, 808 nm blocking filters were employed and the power meter was placed at the maximum available distance. Nevertheless, near the generation threshold, even a residual pump level on the order of 10 µW becomes significant and may favor the isotropic reference mirror in the measured contrast ratio.

2. Another possible explanation is that the Meta-Mirror exhibits slight birefringence, which causes a small modulation of the linear polarization across the beam cross-section when working in reflection. This effect may have contributed to the limited polarization contrast observed during the experiment. The maximal polarization contrast ratio measured with Meta-Mirror was 1:1600, while the measured polarization contrast ratio with isotropic mirror and polarized pumping was slightly higher at threshold.

It should be noted that the polarization contrast ratio measurement standard deviations close to threshold are significant. The polarization contrast ratio measured with the reference mirror represents the best result under polarized pumping conditions. Even a slight change in the pump polarization direction or a minor rotation of the crystal's birefringence axis—possibly due to thermal drift—can cause a sharp drop in polarization contrast.

During the investigation, an important question arose: "why does the polarization contrast not reach its maximum when the pump polarization and the S-polarization of the mirror are aligned with the orthogonal eigen-polarization of the active element?" Our interpretation is that the meta-mirror acts as the dominant factor—the leading-order term—while both the pump polarization and the intrinsic birefringence of the active element contribute only as small perturbations. Consequently, the overall improvement in polarization contrast appears to be additive rather than multiplicative, with the meta-mirror providing the most significant

contribution.

It should be noted that the Meta-Mirror contains low sensitivity to the pump polarization direction (see Fig. 3.16(c)), and the active medium can be directly pumped using a multimode fiber with an unpolarized pump source—without any significant impact on the generation threshold or polarization contrast ratio. In contrast, when using an isotropic mirror, a polarizer must be introduced to filter out half of the pump power, effectively doubling the generation threshold. Nevertheless, we chose to compare the data based on the absorbed pump power rather than the power delivered by the pump diode. This approach allows us to study the dynamics of both systems more meaningfully, rather than focusing solely on highlighting the advantages of the Meta-Mirror.

It should be noted that not all McLs utilize polarized pumping. In our study, we compare the Meta-Mirror's performance against an advanced technique. The polarization contrast ratio of 1:3, achieved with an isotropic mirror at 3 W of absorbed pump power, represents the upper limit attainable even when using polarized pumping.

In setups where the pump source is delivered via fiber—as in our configuration—achieving polarized pumping requires additional steps: the beam must be collimated, passed through a polarizer, and then focused into the gain medium. This increases the overall complexity, alignment sensitivity, and physical size of the system. Furthermore, the polarization must be carefully aligned with the birefringence axis of the laser crystal, which is highly sensitive to mechanical stress from the crystal holder. As a result, polarization contrast becomes only semi-stable, with performance depending strongly multiple factors.

In this investigation, we set out the following main goals:

1. To fabricate a Meta-Mirror with a record-high reflection difference between S- and P-polarized light, and apply it in McL in order to maximize polarization contrast.

2. To achieve this without compromising McL output power, beam quality, or brightness.

3. To verify whether enhanced polarization contrast can lead to overall improvements in beam quality and brightness.

4. To assess the influence of polarized pumping and stress-induced birefringence in Nd:YAG on the performance of the Meta-Mirror.

As an additional objective, we aimed to study polarization dynamics under polarized pumping and an isotropic mirror at high powers—an aspect, to the best of our knowledge, not previously investigated at high powers. Notably, the identification of a threshold pump power beyond which the output beam ceases to be significantly polarized appears to be a particularly interesting result.

3.3.4 Summary

We presented a novel design of a polarizing Meta-Mirror and employed it in combination with polarized pumping in a Nd:YAG McL to enhance the laser's polarization contrast ratio. We investigated the polarization contrast dynamics as a function of pump power and the orientation of the Meta-Mirror polarization axis relative to the pump polarization and the orthogonal polarization axes of the laser crystal. For comparison, we also evaluated the performance using a conventional isotropic mirror, where the polarization contrast is determined solely by the pump polarization and the intrinsic orthogonal states of the laser crystal.

As demonstrated by our experimental data (Fig. 3.15), both the Meta-Mirror and polarized pumping individually achieve a polarization contrast ratio exceeding 1000, up to an absorbed pump power threshold of approximately 1 W. Beyond this point, only the Meta-Mirror is capable of sustaining high polarization contrast, which gradually declines with further increase of pump power. In addition, the use of polarizing Meta-Mirror also enhances the beam quality factor (M^2), output power, and brightness slightly. Optimal performance is observed when the pump polarization direction is aligned with the Meta-Mirror's S-axis, resulting in increased brightness and improved polarization contrast.

The Meta-Mirror configuration provides significantly lower sensitivity to the pump polarization direction compared to a standard output coupler (see Fig. 3.16). At an absorbed pump power of 0.86 W, the polarization contrast ratio in the Meta-Mirror setup remains relatively stable, varying only between 900 and 1000 3.16. In contrast, the conventional setup shows a much stronger polarization fluctuation, ranging from 1 to 1500. The contrast curve reaches its steepest slope at the maximum value, which aligns with the orthogonal polarization axes of the laser crystal.

Rotating the Meta-Mirror relative to the longitudinal mode polarization direction (determined by crystal holder symmetry) 3.16, we observed chaotic polarization contrast fluctuations within a range of 700–1000 rather than following a strict trend. The output polarization direction closely follows the Meta-Mirror's rotation, aligning with the corresponding symmetry changes in the beam profile.

Chapter 4

Research Methodology

4.1 Experimental methods

During this investigation, several experimental tools were employed for data collection. This section describes the experimental setups and methodologies used to obtain the data presented in Sections 3.1, 3.2, and 3.3.

4.1.1 Pumping Configurations

For optical pumping, a fiber-coupled laser diode with a core diameter of 100 μm was employed. The diode was mounted on a Peltier element and actively temperature-stabilized at 25°C to ensure consistent spectral and power characteristics. The dependence of the diode's optical output power on the injection current is shown in Fig. 4.1(a); a maximum drive current of 9 A provided an optical output power of approximately 12 W. As the pump power increased from the lasing threshold up to 12 W, the emission peak wavelength shifted from $\approx$ 803 nm to $\approx$ 805 nm, which is close, though not identical, to the wavelength corresponding to the maximum absorption cross-section of the Nd:YAG active medium (see Fig. 4.1(b)). Further increase in the injection current would induce additional red-shifting of the emission spectrum; however, the current was limited to 9 A to avoid diode degradation and to maintain measurement

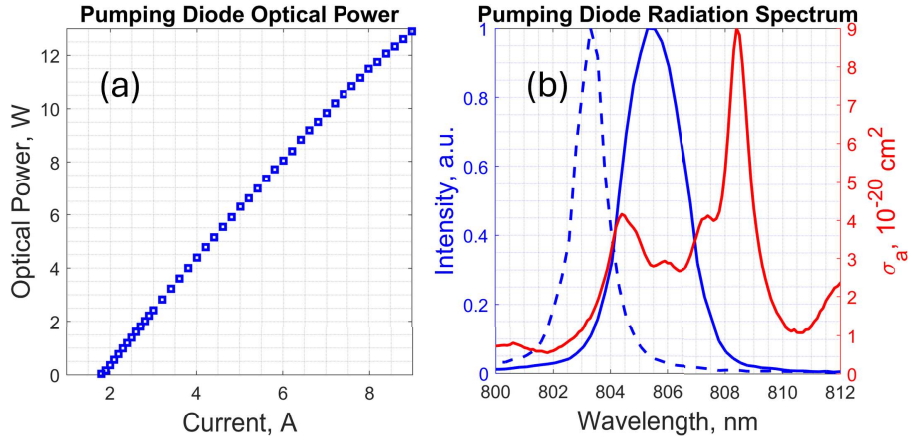


Figure 4.1: (a) Optical output power of the pump diode as a function of the injection current. (b) Emission spectra of the pump diode measured at minimum and maximum injection currents of 2 A (dashed blue line) and 9 A (solid blue line), respectively. For comparison, the red solid line represents the wavelength-dependent absorption cross-section $\sigma_a(\lambda)$ of the Nd:YAG crystal.

repeatability.

For the experiments described in sections 3.1 and 3.2, the pumping configuration shown in Fig. 4.2(a) was employed. The pump radiation emitted from the fiber end facet was focused by a single aspherical lens L_1 with a focal length of 8 mm. The spatial intensity distribution of the pump beam was recorded near the beam waist using a CMOS camera mounted on a linear translation stage equipped with a micrometer screw, providing sub-millimeter positioning accuracy. The beam diameter was measured as a function of the propagation distance Y for several fiber–lens distances X within the ranges of 11–16 mm (see Fig. 4.2(b)) and 17–20 mm (see Fig. 4.2(c)). The polarization direction of the pump output was unstable and varied with both the injection current and the positioning of the fiber cable.

For the experiments described in section 3.3, the pumping configuration shown in Fig. 4.3(a) was employed. This configuration provided additional stabilization of the pump polarization direction and enabled precise control and rotation of the polarization state. The pump diode radiation was delivered through an optical fiber, whose end facet was positioned at a distance A from a plano-convex lens L_1 with a focal length

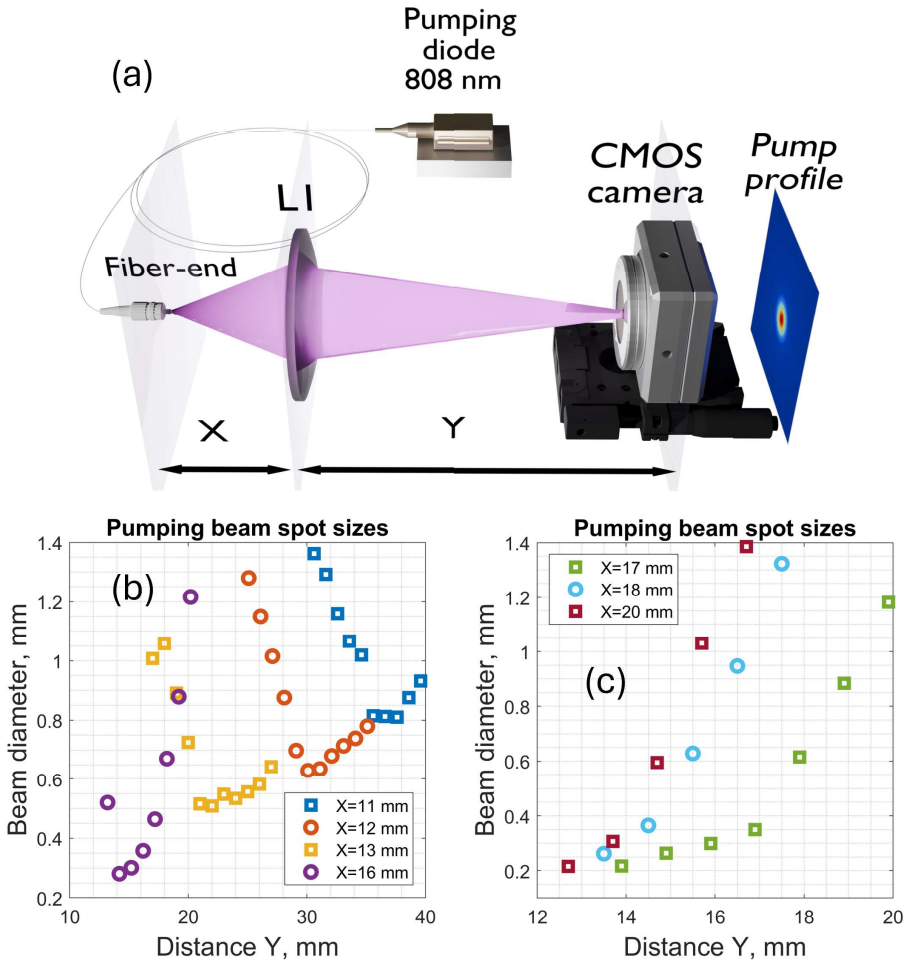


Figure 4.2: (a) Experimental setup for measuring the pump spot size and location, employed in the experiments described in sections 3.1 and 3.2. The dependence of the beam diameter on Y was recorded for several fiber–lens separations X in the ranges of 11–16 mm (b) and 17–20 mm (c).

of 50 mm. The beam then passed through a polarizer that transmitted the p-polarized component and reflected the s-polarized one. The linearly polarized pump beam subsequently propagated a distance B before entering a second plano-convex lens L_2 with an identical focal length of 50 mm. The resulting pump spot was imaged onto a CMOS camera, whose sensor was positioned at a distance C from lens L_2. The beam diameters were determined at the $1/e^2$ intensity level from the recorded spatial intensity profiles. To characterize the beam propagation, the CMOS camera was translated along the optical axis using a micrometer-precision translation stage, allowing the beam diameter to be measured as a function of distance C. The distances A and B were adjusted such

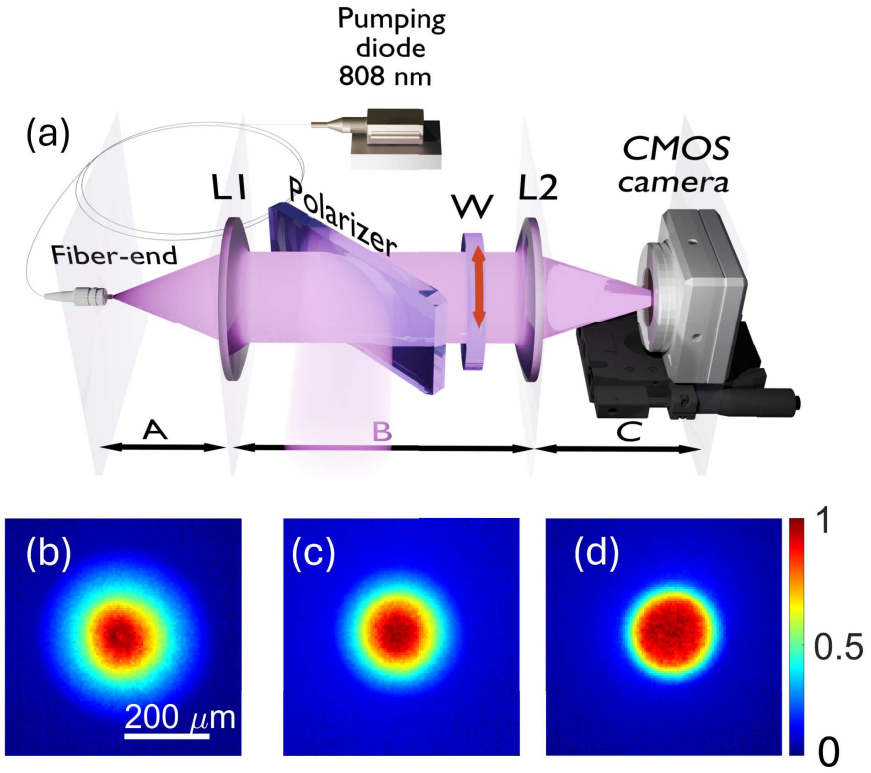


Figure 4.3: (a) Experimental setup for measuring the pump spot size and location, as employed in the experiments described in section 3.3. Beam profiles were recorded in 1 mm steps (b, c, d), where (b) corresponds to the input facet of the Nd:YAG crystal described in section 3.3. Due to the higher refractive index of Nd:YAG compared to air, a 1 mm propagation distance in air corresponds to approximately 1.8 mm of beam evolution inside the crystal.

that the beam waist at the caustic was approximately 300 μm. Beam profiles were recorded in 1 mm steps (b, c, d), where (b) corresponds to the input facet of the Nd:YAG crystal described in section 3.3. Due to the higher refractive index of Nd:YAG compared to air, a 1 mm propagation distance in air corresponds to approximately 1.8 mm of beam evolution inside the crystal. The pump beam polarization contrast ratio and the polarized pump optical power were evaluated using the setup depicted in Fig. 4.4(a). The beam emitted from the fiber was collimated by lens L_1 and subsequently passed through a Brewster-angle polarizer, which converted the initially unpolarized radiation into a linearly polarized beam. The half-wave plate W was mounted on a step-motor rotation stage, enabling precise control of the pump polarization direction between

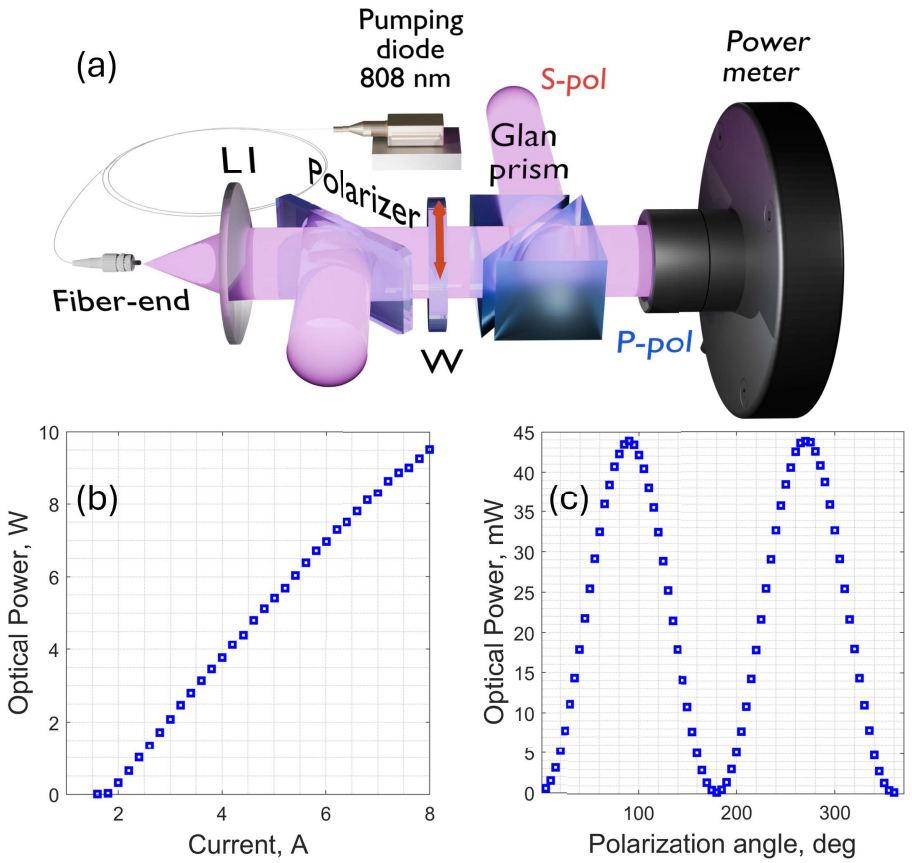


Figure 4.4: (a) Experimental setup for measuring the pump polarization contrast ratio and the polarized pump optical power. The dependence of the optical power on the injection current (b) was measured with the Glan–Prism removed from the setup. The pump polarization contrast ratio estimated from the graph in (c) is approximately 1:270.

horizontal and vertical orientations. A Glan–Prism polarizer was used to separate the s- and p-polarization components, providing a polarization extinction ratio of 1:10^6. The rotation angle of the wave plate W was calibrated with respect to the polarization direction by measuring the transmitted optical power (c), where the change in polarization angle corresponded to half the wave plate rotation angle. The dependence of the optical power on the injection current (b) was measured with the Glan–Prism removed from the setup. The overall optical power was lower compared to Fig. 4.1(a) due to the rejection of the s-polarized component by the polarizer. The pump polarization contrast ratio, estimated from the graph in (c), was approximately 1:270, corresponding to the ratio of minimal and maximal transmitted powers P_{min} and P_{max}, respectively.

A two-lens configuration (collimation and focusing) was employed, as shown in Fig. 4.4, instead of a single-lens system for the following reasons:

1. The Brewster-angle polarizer, with face dimensions of 20×40 mm^2 and a thickness of 5 mm, required additional space in the optical path;

2. The transmission and reflection characteristics of the polarizer for the s- and p-polarization components are highly sensitive to the angle of incidence (AOI); using a collimated beam ensures that its spatial frequency components correspond to small AOI values.

Although it was experimentally possible to reduce the focused pump spot size below 300 μm, we intentionally selected conditions under which the pump spot size was approximately three times larger than the fiber core diameter. Based on prior experience, a larger pump spot yields reduced divergence of the generated laser beam. This lower divergence was required to avoid spatial filtering effects by the Meta-Mirror, which, although beneficial, was excluded here to isolate the polarization-related effects. Additionally, a smaller waist size in the crystal center would result in greater beam size variation at the input and output faces of the microchip crystal, introducing further deviation from the mean-field approximation.

4.1.2 Active Medium Investigation

Throughout all experiments, the active medium employed was Nd:YAG. Two distinct Nd:YAG microchip laser crystals were used, differing in Nd^{3+} ion molar concentration, crystal length, absorbed pump fraction, and cavity losses:

1. **Crystal No. 1:** Nd:YAG crystal with a length of $L_1 = 2.3$ mm was used in the experiments described in Section 3.1. According to the manufacturer's specifications, the Nd^{3+} molar doping concentration was 1%. The crystal had a 3×3 mm^2 aperture and was employed in a longitudinal pumping configuration, as illustrated in

Fig. 4.2. Both surfaces were plano–plano; one side was coated with high reflection (HR) at 1064 nm and high transmission (HT) at 808 nm, while the opposite side was antireflection (AR) coated for both 1064 nm and 808 nm. The measured absorbed pump power in the crystal was approximately 50% over the diode injection current range of 3–9 A and varied by only a few percent within this interval. The remaining half of the pump power was transmitted through the crystal. The evaluated absorption coefficient was $\alpha_1 = 3.01$ cm^{-1}. When this crystal was incorporated into the laser cavity, the measured round-trip loss was $\delta = 0.0635$ (see Section 4.1.8, Cavity No. 1).

2. **Crystal No. 2:** Nd:YAG crystal with a length of $L_2 = 2.0$ mm was used in the experiments described in Sections 3.2 and 3.3. The manufacturer specified a Nd^{3+} molar doping concentration of 2%, whereas the measured absorption coefficient corresponds to a lower effective neodymium concentration. The crystal had the same 3×3 mm^2 face dimensions and was placed in the longitudinal pumping configuration shown in Fig. 4.3. Its surfaces were also plano–plano, with identical coating design to Crystal No. 1: HR@1064 nm/HT@808 nm on one side and AR@1064 nm,808 nm on the other. The measured absorbed pump fraction was approximately 53%. The corresponding absorption coefficient was determined as $\alpha_2 = 3.78$ cm^{-1}. The round-trip cavity loss measured with this crystal was $\delta = 0.0173$ (see Section 4.1.8, Cavity No. 2).

The absorption coefficient α of each crystal was determined by measuring the incident pump power P_{in} before and the transmitted power P_{t} after the crystal, and applying the Beer–Lambert relation for known crystal lengths L_1 and L_2:

$$P_{\text{t}} = P_{\text{in}} e^{-\alpha L}, \qquad \alpha = -\frac{\ln\left(\frac{P_{\text{t}}}{P_{\text{in}}}\right)}{L}. \tag{4.1}$$

The corresponding absorbed power fraction along the crystal length z is

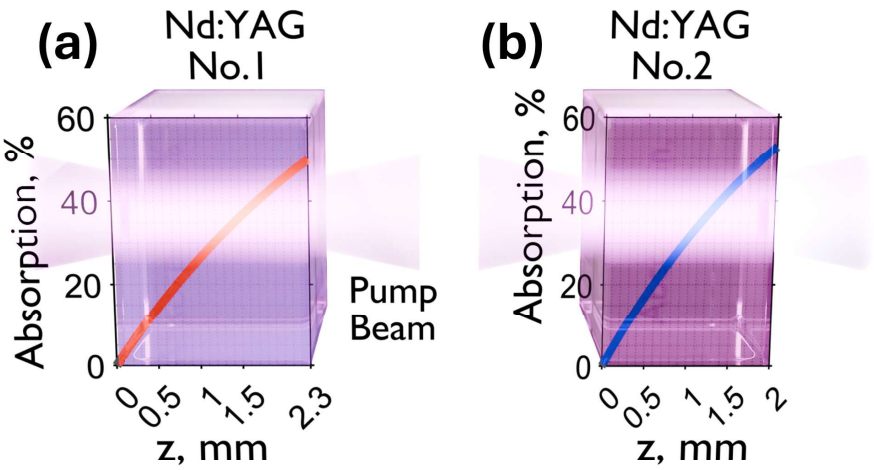


Figure 4.5: Calculated absorbed pump power as a function of propagation distance z inside the Nd:YAG microchip crystals: (a) Crystal No. 1 with an absorption coefficient of $\alpha_1 = 3.01$ cm^{-1}, used in the experiments described in Section 3.1; and (b) Crystal No. 2 with an absorption coefficient of $\alpha_2 = 3.78$ cm^{-1}, used in the experiments presented in Sections 3.2 and 3.3.

given by $1 - e^{-\alpha z}$. The absorption dependence on propagation distance z for both crystals is plotted in Fig. 4.5.

4.1.3 Laser power measurement

For power measurements, we employed the Ophir 3A thermopile sensor, capable of measuring optical power in the range of 10 μW to 3 W, with an optical aperture of $\varnothing$9.5 mm. The device operates over a broad spectral range from approximately 0.19 to 20 μm. The thermopile sensor consists of an array of thermocouples that convert incident radiation into a voltage via the Seebeck effect. A detailed description of this sensor model can be found at MKS Inc. website. The sensor response time is relatively slow ($\sim$ 1.8 s), and thus, only the average power was evaluated during the experiments. The laser power was isolated from the residual pump radiation using a dichroic mirror, designed to be highly reflective at 808 nm (pump wavelength) and highly transmissive at 1064 nm (lasing wavelength). The output power was measured following the procedure below:

1. The laser was switched on and allowed to stabilize for approximately

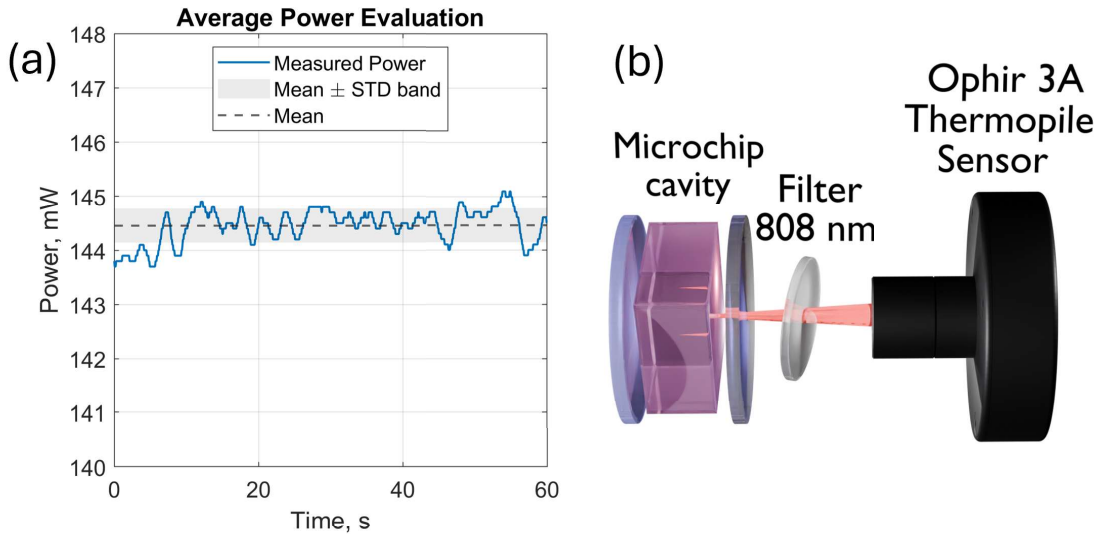


Figure 4.6: Time-resolved laser power measurement (a). The power trace was logged and used to compute the mean power (μ) and standard deviation (σ). (b) Ophir 3A thermopile sensor used for average-power measurements; model details: MKS Inc. website.

1 min, with the power meter already active. The optical path was then blocked to record the background signal, which was later subtracted from the measured power values.

2. The optical path was unblocked, and the power meter was allowed to reach thermal equilibrium for an additional ~ 1 min.
3. The laser power was subsequently logged for another 1 min.
4. The first and second statistical moments were calculated from the dataset, yielding the average power and corresponding standard deviation.

4.1.4 Masurement of Beam Quality Factor M^2

The beam quality factor M^2 was measured in accordance with the ISO 11146 standard [193]. The experimental setup (see Fig. 4.7) was arranged such that the laser beam emerging from the McL cavity was directed towards the beam propagation analyzer (BPA) via two metallic mirrors (MeM), positioned at an incidence angle of $\approx 45°$, which enabled beam alignment.

Residual pump radiation at 808 nm was suppressed using a pump reflection filter (PRF), transmitting only the laser wavelength. Within the

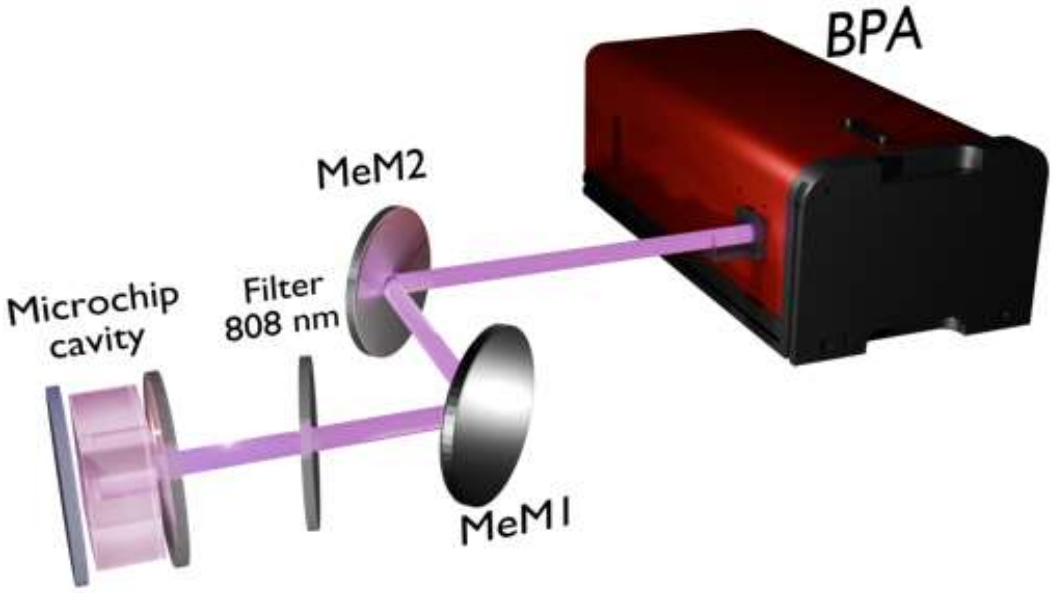


Figure 4.7: Experimental setup for measuring the beam quality factor M^2. The laser beam emitted from the McL cavity first passes through an optical filter that transmits the lasing wavelength at 1064 nm while blocking the residual pump radiation at 808 nm. The filtered beam is subsequently reflected twice by silver mirrors (MeM1 and MeM2), which enable precise adjustment of the beam alignment. Finally, the beam is directed into the beam propagation analyzer (BPA), which incorporates a focusing lens with a focal length of $f = 400$ mm at its input.

BPA, the beam intensity was adjusted using a variable attenuator before passing through a focusing lens of focal length 400 mm (see Fig. 4.8). The converging beam then propagated through a folded optical path consisting of eight mirrors, four of which were mounted on a motorized linear translation stage, allowing continuous variation of the propagation distance between the focusing lens and the CCD camera positioned at the end of the optical path. The CCD camera captured beam profiles around the focal region (beam waist), from which the beam widths were determined and subsequently used for the M^2 evaluation. The input beam alignment is important for accurate estimation of M^2, since an off-axis beam may experience partial clipping along the optical path due to the limited clear aperture (see Fig. 4.8). Under such conditions, the beam quality factor M^2 is no longer a valid descriptor for beams containing sharp or discontinuous edges [147]. Moreover, off-axis prop-

agation causes the effective propagation distance to deviate from the nominal value, introducing an additional systematic error and leading to further inconsistency in the M^2 measurement. Cases (1) and (2) illustrate the beam profiles for misaligned and correctly aligned beam paths, respectively, as the stage is translated.

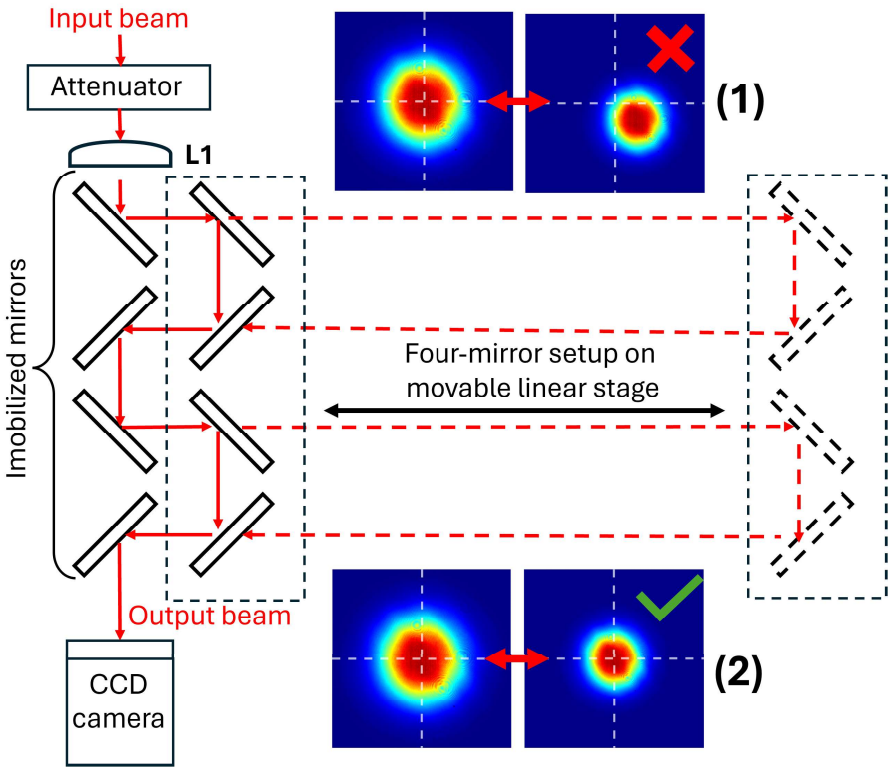


Figure 4.8: Schematic illustration of the Beam Propagation Analyzer (BPA) principle. The input laser beam passes through an attenuator and a focusing lens with a focal length of $f = 400$ mm (L1), and is subsequently reflected eight times by mirrors positioned at a 45° angle of incidence. The total propagation length is adjusted by translating a four-mirror assembly mounted on a linear stage, while the beam diameter is recorded using a CCD camera.

The beam width (BW) is determined using the following expressions for the x- and y-directions:

$$w_x^2 = 4\frac{\iint (x - x_0)^2 I(x,y)\,\mathrm{d}x\,\mathrm{d}y}{\iint I(x,y)\,\mathrm{d}x\,\mathrm{d}y}, \qquad w_x^2 = 4\sigma_x^2, \tag{4.2}$$

$$w_y^2 = 4\frac{\iint (y - y_0)^2 I(x,y)\,\mathrm{d}x\,\mathrm{d}y}{\iint I(x,y)\,\mathrm{d}x\,\mathrm{d}y}, \qquad w_y^2 = 4\sigma_y^2, \tag{4.3}$$

where the beam radius is denoted as w_x and w_y for the x- and y-directions, respectively, and $\sigma_{x,y}$ represent the normalized second moments. The function $I(x, y)$ denotes the measured intensity distribution on the CCD camera plane, while x_0 and y_0 correspond to the first spatial moments:

$$x_0 = \frac{\iint x\, I(x,y)\, \mathrm{d}x\, \mathrm{d}y}{\iint I(x,y)\, \mathrm{d}x\, \mathrm{d}y}, \qquad y_0 = \frac{\iint y\, I(x,y)\, \mathrm{d}x\, \mathrm{d}y}{\iint I(x,y)\, \mathrm{d}x\, \mathrm{d}y}. \tag{4.4}$$

The measured beam width (BW) values are expressed as functions of the position along the optical axis z:

$$w_x^2(z) = w_{0x}^2 + \left[M_x^2 \frac{\lambda}{\pi w_{0x}} (z - z_{0x}) \right]^2, \qquad w_y^2(z) = w_{0y}^2 + \left[M_y^2 \frac{\lambda}{\pi w_{0y}} (z - z_{0y}) \right]^2, \tag{4.5}$$

where w_{0x} and w_{0y} denote the beam waist radii at the caustic, z_{0x} and z_{0y} are the corresponding waist positions, λ is the laser wavelength (1064 nm in this case), and M_x^2 and M_y^2 are the beam quality factors. These parameters are determined by plotting the measured beam width dependencies $w_x(z)$ and $w_y(z)$, fitting them according to Eq. 4.5, and extracting the corresponding fit coefficients. The fitting function is expressed in terms of the coefficients A, B, and C:

$$w^2(z) \;=\; A\, z^2 + B\, z + C, \tag{4.6}$$

then with the identified coefficients the beam parameters are calculated:

$$z_0 \;=\; -\frac{B}{2A}, \qquad w_0^2 \;=\; C - \frac{B^2}{4A}, \qquad M^2 \;=\; \frac{\pi}{\lambda}\, w_0\, \sqrt{A}. \tag{4.7}$$

In practice, certain measurement points may exhibit significant deviations due to several factors:

1. camera noise (readout or shot noise);
2. partial beam clipping at the detector edges;
3. pixel saturation effects;
4. dust particles, scattering, or other optical artifacts;
5. slight misalignment or mechanical vibrations.

The overall (composite) beam quality factor was evaluated from the

beam quality factors measured in the x and y directions as

$$M^2 = \sqrt{M_x^2\, M_y^2}. \tag{4.8}$$

Each beam quality factor measurement was repeated multiple times, and the corresponding mean values and standard deviations were calculated from the obtained data.

4.1.5 Laser Beam Brightness Evaluation

During the experiments, beam brightness was determined from the measured output power P and beam-quality factors M_x^2 and M_y^2 [196] using

$$B \;=\; \frac{P}{M_x^2\, M_y^2\, \lambda^2}. \tag{4.9}$$

The quantities P, M_x^2, and M_y^2 were measured repeatedly, from which we estimated their first and second moments. Define $X \equiv M_x^2$ and $Y \equiv M_y^2$. The corresponding means and variances [197, p.54] are

$$\mu_P = \langle P \rangle\,, \qquad \sigma_P^2 = \left\langle P^2 \right\rangle - \mu_P^2, \tag{4.10}$$

$$\mu_X = \langle X \rangle = \left\langle M_x^2 \right\rangle, \qquad \sigma_X^2 = \left\langle X^2 \right\rangle - \mu_X^2 = \left\langle M_x^4 \right\rangle - \mu_X^2, \tag{4.11}$$

$$\mu_Y = \langle Y \rangle = \left\langle M_y^2 \right\rangle, \qquad \sigma_Y^2 = \left\langle Y^2 \right\rangle - \mu_Y^2 = \left\langle M_y^4 \right\rangle - \mu_Y^2. \tag{4.12}$$

The mean brightness can be approximated [198, p. 40] as:

$$\langle B \rangle = \mu_B = \frac{\langle P \rangle}{\langle M_x^2 \rangle \left\langle M_y^2 \right\rangle \lambda^2}. \tag{4.13}$$

Using a first-order Taylor expansion of Eq. (4.9) about the mean value $\langle B \rangle$, together with the standard error-propagation formula for statistically independent variables [198, p. 41], the standard deviation of the brightness was approximated as

$$\sigma_B \;\approx\; \mu_B \sqrt{\left(\frac{\sigma_P}{\mu_P}\right)^2 + \left(\frac{\sigma_X}{\mu_X}\right)^2 + \left(\frac{\sigma_Y}{\mu_Y}\right)^2}. \tag{4.14}$$

4.1.6 Laser beam profile estimation in near and far fields

During the experiments, the laser beam intensity distribution was investigated in both the near- and far-field regions. The experimental setups are illustrated in Fig. 4.9, where the beam intensity profiles were recorded using a silica-based CMOS camera (model WinCamD-LCM, DataRay Inc.). The camera features a pixel size of 5.5 μm and a sensor area of $11.3 \times 11.3\,\mathrm{mm}^2$. Each intensity pattern was averaged over an integration time of approximately 83 ms. Additional specifications of the CMOS camera can be found at DataRay Inc. website.

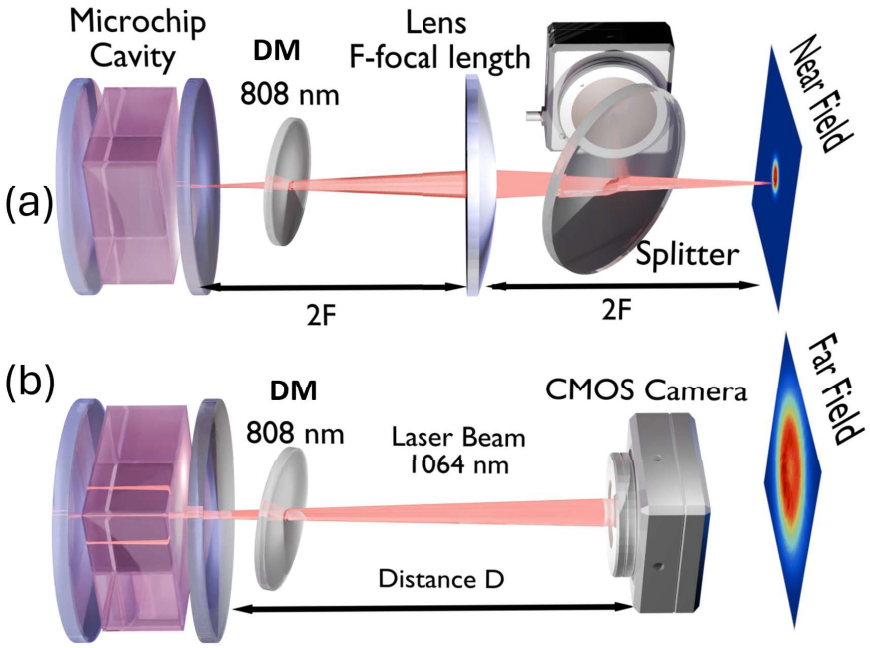


Figure 4.9: Schematic representation of the experimental setups used for laser beam intensity profile measurements in the (a) near-field and (b) far-field configurations.

Dichroic mirror (DM) reflecting the pump wavelength at 808 nm and transmitting the laser wavelength at 1064 nm was used to block the residual pump radiation (see Fig. 4.9). Neutral density filters were employed before the camera sensor, ensuring that the measured signal remained within the linear dynamic range of the detector—below the saturation threshold $I_{\mathrm{sat}} \approx 1\,\mathrm{mW/cm}^2$ and above the noise floor $I_{\mathrm{noise}} \approx 1\,\mu\mathrm{W/cm}^2$. The recorded two-dimensional intensity arrays (2048×2048

pixels) were subsequently processed in MATLAB (MathWorks, Inc.), where the first and second statistical moments of the beam intensity were calculated and the corresponding spatial intensity distributions were visualized.

For the far-field beam profile measurements (see Fig. 4.9(b)), the CMOS camera was positioned behind the McL cavity at a distance of $D \approx 30\,\text{cm}$, which exceeds the Rayleigh length z_R of the investigated beams. The typical beam waist radius in our experiments was $w_0 \approx 150\,\mu\text{m}$, corresponding to a Rayleigh length of $z_R \approx 6.6\,\text{cm}$ at a wavelength of 1064 nm. The far-field region is thus defined as the propagation zone beyond the Rayleigh range.

For the near-field beam characterization (see Fig. 4.9(a)), a $4F$ imaging system was employed, containing a plano-convex lens with a focal length of $F = 75\,\text{mm}$ placed at a distance of $2F = 150\,\text{mm}$ from both the laser cavity and the CMOS camera. A wedged beam splitter was used to reflect a small fraction of the laser power from one splitter surface onto the CMOS detector.

Beam profiles were recorded using a WinCamD-LCM CMOS camera (DataRay Inc.).Additional specifications of the CMOS camera can be found at DataRay Inc. website

4.1.7 Laser Polarization Extinction Ratio Estimation

The laser beam polarization extinction ratio (PER) was measured using the setup illustrated in Fig. 4.10. The beam emitted from the McL cavity first passes through a spectral filter that blocks residual pump radiation at 808 nm. It is then directed into a Glan–Prism polarizer, which spatially separates the S and P polarization components via internal reflection. The Glan–Prism reflects the S-polarized component and transmits the P-polarized component with an intrinsic extinction ratio of approximately $1{:}10^6$, which is about two orders of magnitude higher than the maximum polarization ratio measured for the laser beam in the experiment.

The Glan–Prism is mounted on a rotation stage, allowing precise P-polarization alignment with the strong and weak laser beam polar-

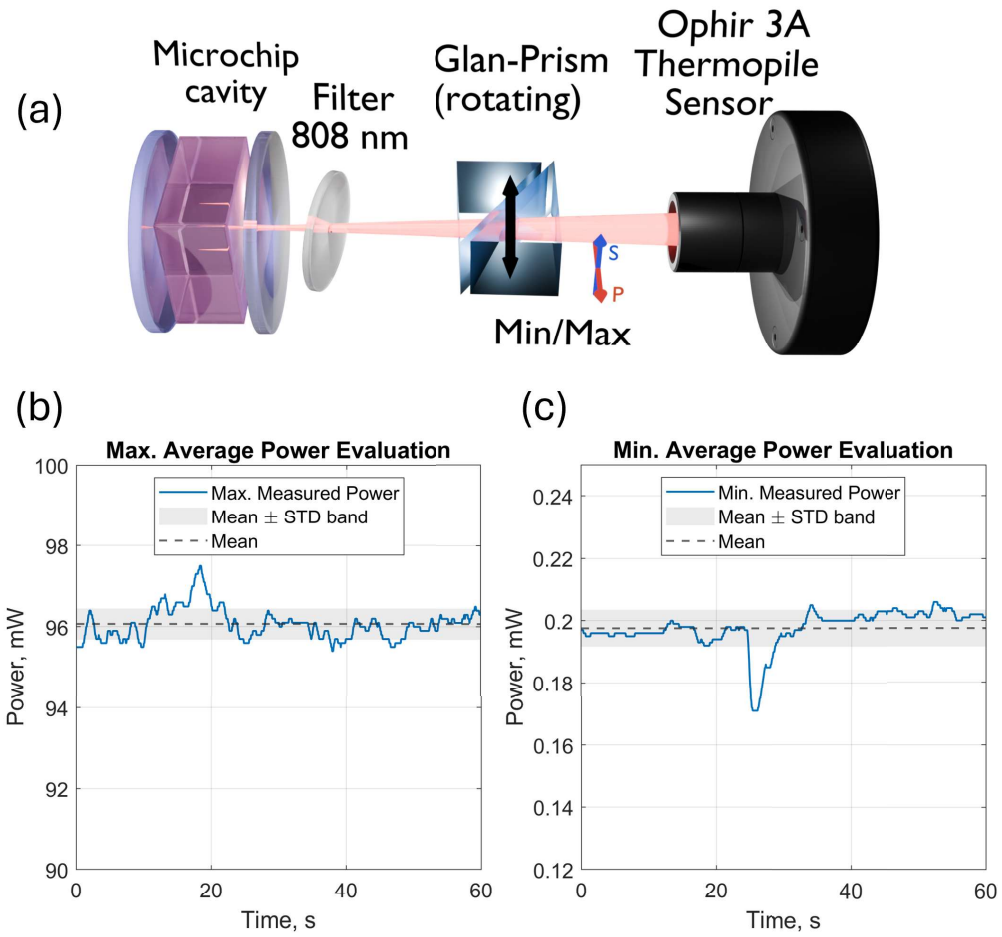


Figure 4.10: (a) Experimental setup for laser beam polarization contrast estimation. The prism is mounted on a rotation stage, allowing precise alignment with the strong (b) and weak (c) polarization axes.

ization axes. The average powers of the corresponding polarization components, denoted as $P_{\max}$ and $P_{\min}$, are measured using an Ophir 3A thermopile sensor (model details: MKS Inc. website), with each measurement integrated over approximately one minute (see examples in Fig. 4.10(b,c)). The mean values $\langle P_{\max} \rangle$ and $\langle P_{\min} \rangle$, together with their standard deviations $\sigma_{P_{\max}}$ and $\sigma_{P_{\min}}$, are then evaluated. Based on these quantities, the mean and standard deviation of the polarization extinction ratio (PER) are calculated as follows:

$$\langle PER \rangle = \frac{\langle P_{max} \rangle}{\langle P_{min} \rangle}, \qquad \sigma_{PER} = \langle PER \rangle \sqrt{\left(\frac{\sigma_{Pmax}}{\langle P_{\max} \rangle} \right)^2 + \left(\frac{\sigma_{Pmin}}{\langle P_{\min} \rangle} \right)^2}. \tag{4.15}$$

Residual pump light, even after the application of an 808 nm optical

filter, could lead to inaccuracies in power measurements. To minimize this effect, the power meter was positioned several meters away at the end of the optical table, thereby reducing the influence of scattered pump radiation. Given the high thermal sensitivity of the thermopile sensor, a stabilization period was introduced prior to each measurement: the pump laser was switched on with the optical path blocked, and the system was allowed to thermally stabilize for approximately 2 minutes. The most sensitive measurements were performed near the generation threshold, corresponding to an absorbed pump power of 0.5 W. At this condition, the laser output power was 40 mW, and the measured polarization extinction ratio (PER) was approximately 1:1800. The weaker polarization component power was around 22 µW, which lies well within the specified detection range of the sensor. However, close to the threshold, pronounced power fluctuations were observed, leading to an increased standard deviation in the measured PER.

4.1.8 Estimation of Cavity Losses

The experimental evaluation of the cavity round-trip intensity loss, δ, was required for our semi-analytical treatment in section 3.1.4 and to verify efficient resonator operation. For a four-level laser, δ can be determined by using a set of output couplers with different reflectivities and measuring the corresponding pump-threshold power for each case [16, 199]. The threshold condition is then given by:

$$-\ln R = 2g_0 l - \delta, \tag{4.16}$$

where g_0 is the small-signal (unsaturated) gain coefficient, l is the crystal length, and R is the output-coupler intensity reflectivity. In the small-signal regime, g_0 is directly proportional to the pump power P_{in}. We write

$$2g_0 l \;=\; \frac{2\eta}{I_{\text{S}} A}\, P_{\text{in}},$$

where η is the pump-to-inversion efficiency, I_{S} is the saturation intensity, and A is the effective mode area in the gain medium. Substituting this

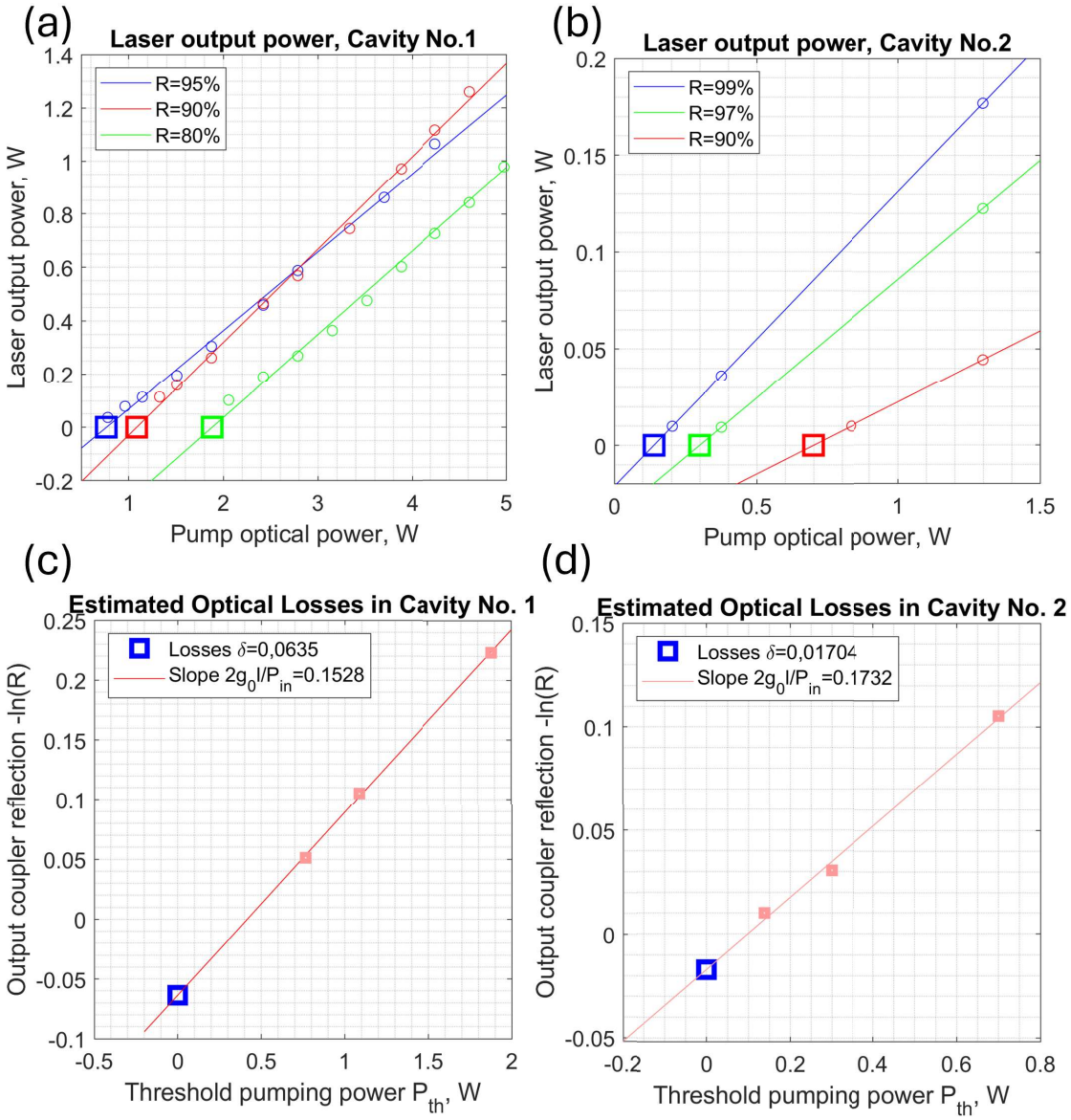


Figure 4.11: Experimental estimation of the round-trip losses δ in two laser cavities, denoted as Cavity No. 1 (a,c) and Cavity No. 2 (b,d). The cavities contained Nd:YAG crystals with Nd^{3+} doping levels of 1% and 2%, and crystal lengths of 2.3 mm and 2.0 mm, respectively. The laser threshold pump powers were derived from the measured output–pump power dependence by linear fitting, where the intercept of the fitted line with the abscissa axis defines the threshold (a,b). Measurements were performed using three output couplers with reflectivities of $R = 95\%, 90\%, 80\%$ for Cavity No. 1 and $R = 99\%, 97\%, 90\%$ for Cavity No. 2. The natural logarithms of the output coupler reflectivities were plotted versus the corresponding threshold pump powers (c,d), and the linear extrapolation to the ordinate axis yielded the round-trip loss values: $\delta \approx 0.06$ for Cavity No. 1 and $\delta \approx 0.02$ for Cavity No. 2.

relation into the threshold condition (4.16) yields

$$-\ln R = \frac{2\eta}{I_S A} P_{in} - \delta. \tag{4.17}$$

The round-trip loss δ is a fixed property of the cavity and does not change with pump power or with the output-coupler reflectivity R. At lasing threshold the condition (4.16) holds, with the pump power P_{in} evaluated at its threshold value P_{th}.

We experimentally determined δ for two resonators, denoted Cavity No. 1 (Fig. 4.11(a,c)) and Cavity No. 2 (Fig. 4.11(b,d)). The cavities incorporated Nd:YAG crystals with Nd^{3+} doping levels of 1% and 2%, and crystal lengths of 2.3 mm and 2.0 mm, respectively. Cavity No. 1 was used in the experiments described in section 3.1, while Cavity No. 2 was used in sections 3.2 and 3.3. The losses were estimated as follows:

1. Measure the threshold pump power P_{th} using several output couplers with different reflectivities R (see Fig. 4.11(a,b)).

2. Plot $-\ln R$ versus P_{th} (see Fig. 4.11(c,d)).

3. Fit a straight line to the data and extrapolate to $P_{\text{th}} = 0$; the intercept gives the round-trip resonator loss δ (see Fig. 4.11(c,d)).

The estimated round-trip losses are $\delta \approx 0.06$ for Cavity No. 1 and $\delta \approx 0.02$ for Cavity No. 2. In section 3.1 we used the parameter $\rho = \frac{-\ln R+\delta}{2}$, which, for an output-coupler reflectivity $R = 0.9$, evaluates to $\rho \approx 0.0825$. The factor of 2 arises because ρ is defined for the field amplitude; the corresponding intensity exponent is twice as large. Indeed, if the amplitude ansatz is $A(t) = A_0\, e^{\rho t/2}$, then the intensity is $I(t) = |A(t)|^2 = |A_0|^2\, e^{\rho t}$.

4.1.9 Estimation of the Optimal Output Coupler Reflectivity

Here, we estimate the dependence of the optimal output coupler reflectivity on the incident pump power for both Cavity No. 1 and Cavity No. 2,

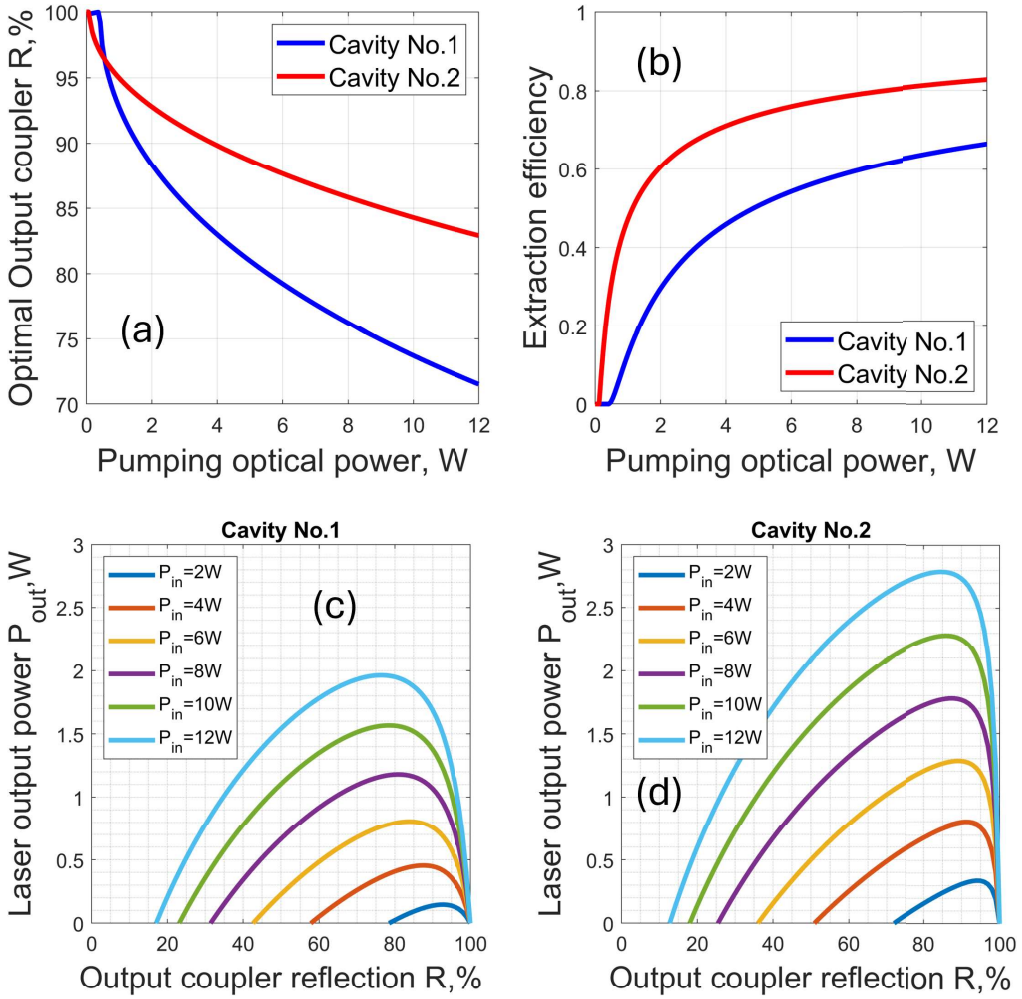


Figure 4.12: (a) Optimal output coupler reflectivity dependence on pumping optical power for cavity No.1 and No.2. (b) Extraction efficiency dependence on pumping optical power for cavity No.1 and No.2, when using the optimal output coupler. (c, d) Laser output power dependence on output coupler reflection R for several pumping optical powers in cavity no.1 and cavity no.2.

discussed in Section 4.1.8. As shown in Fig. 4.11, the round-trip loss values were determined to be $\delta \approx 0.06$ for Cavity No. 1 and $\delta \approx 0.02$ for Cavity No. 2. Furthermore, as indicated in Fig. 4.11(c,d), the corresponding slope parameters were obtained as $2g_0 l/P_{\text{in}} = 0.1528\ \text{W}^{-1}$ and $2g_0 l/P_{\text{in}} = 0.1732\ \text{W}^{-1}$, respectively. The optimal output coupler reflectivity R_{opt} can then be expressed as follows [16]:

$$-\ln R_{\text{opt}} = \left(\sqrt{\frac{2g_0 l}{\delta}} - 1\right)\delta, \qquad R_{\text{opt}} = e^{-\left(\sqrt{\frac{2g_0 l}{\delta}}-1\right)\delta}, \tag{4.18}$$

where $2g_0 l$ denotes the small-signal (unsaturated) gain accumulated over one cavity round trip. This quantity depends on the incident pump power P_{pump} and can be expressed for Cavity No. 1 as $2g_0 l = 0.1528\, P_{\text{pump}}$ and for Cavity No. 2 as $2g_0 l = 0.1732\, P_{\text{pump}}$ (see Fig. 4.11). The resulting dependence of the optimal output coupler reflectivity $R_{\text{opt}}(P_{\text{pump}})$ for both cavities is illustrated in Fig. 4.12(a).

The extraction efficiency η_E is then expressed as follows [16, Ch. 3]:

$$\eta_E = P_{\text{opt}}/ = P_{\text{avail}}, \qquad \eta_E = \left(1 - \sqrt{\delta/2g_0 l}\right)^2, \tag{4.19}$$

where P_{avail} is the power in upper lasing level (available power) and P_{opt} is lasing power when using the optimal output coupler (see Fig. 4.12(a)). The extraction efficiency dependence on pumping optical power is depicted in Fig. 4.12(b) for both cavities no.1 and no.2.

The laser output power can then be expressed as follows [16, Ch. 3]:

$$P_{\text{out}} = A \left(\frac{1-R}{1+R}\right) I_S \left(\frac{2g_0 l}{\delta - \ln R} - 1\right), \tag{4.20}$$

where $I_S = \frac{h\nu}{\sigma \tau_f}$ is the saturation intensity, which is an intrinsic material parameter determined by the photon energy $h\nu$, the stimulated emission cross-section σ, and the fluorescence lifetime of the upper laser level τ_f. For the Nd:YAG active medium, the saturation intensity is estimated to be $I_S = 2.49 \times 10^7$ W/m^2. The mode area A within the active region was evaluated from the measured laser beam waist using a CMOS camera in the near field (see Sections 3.2.3 and 4.1.6). The average beam radius was found to be $w \approx 115$ μm, yielding a mode area of $A \approx \pi w^2 \approx 1.3 \times 10^{-7}$ m^2.

The dependence of the output power on the output coupler reflectivity R at several pump power levels is presented in Fig. 4.12(c,d) for Cavity No. 1 and Cavity No. 2, respectively. Cavity No. 1 was used for experiments described in section 3.1 and Cavity No. 2 in sections 3.2 and 3.3.

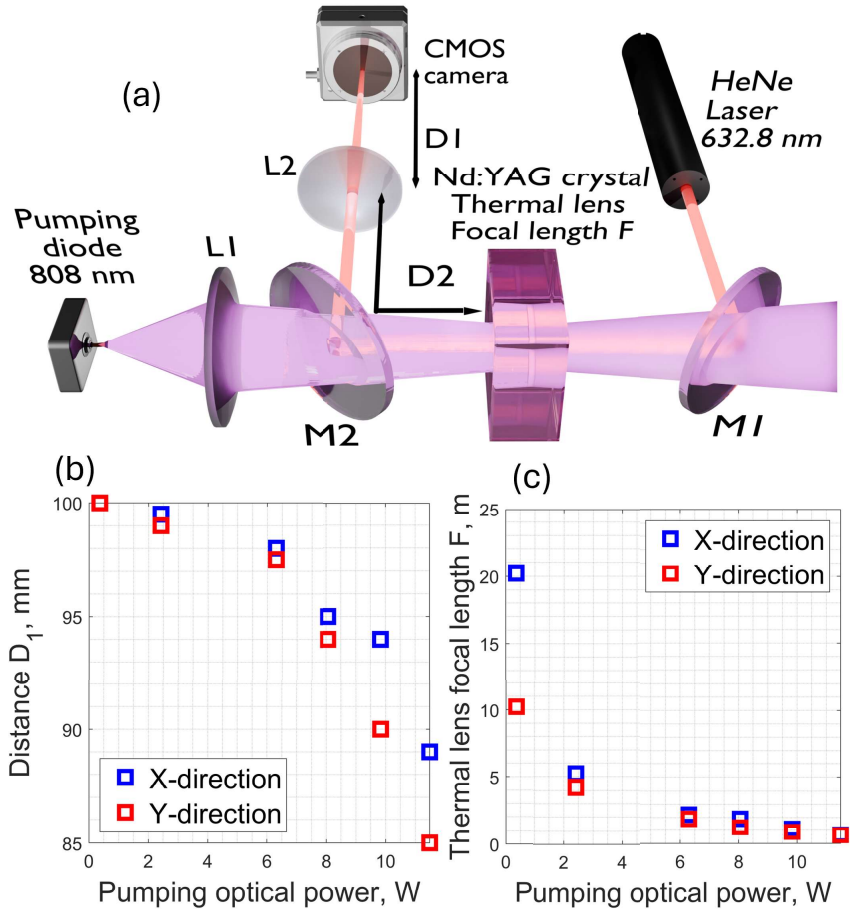


Figure 4.13: (a) Optical setup for estimating the thermal lens focal length F in the Nd:YAG microchip laser crystal.(b) The measured dependence of the focal plane distance D_1 on the absorbed pump power.(c) The extracted dependence of the thermal lens focal length F on the pump power, calculated using the ABCD-matrix-based relation given in Eq. (4.26).

4.1.10 Thermal Lens Estimation

We experimentally evaluated the focal length of the thermally induced lens in the Nd:YAG microchip crystal used in the experiments described in Section 3.1. The investigated crystal was 2.3 mm long with 3×3 mm^2 aperture faces, doped with 1% of Nd^{3+} ions, wrapped in indium foil, and actively cooled around the aperture region at a constant room temperature. An 808 nm fiber-coupled diode laser (fiber core diameter 100 μm) delivering up to 12 W of pump power was used as the pumping source. The experimental optical setup is shown in Fig. 4.13(a). The pump radiation was focused into the Nd:YAG crystal by an aspherical lens L1 with a focal length of 8 mm, forming a ≈ 280 μm pump spot, thereby

inducing a thermal lens. Mirrors M1 and M2 were highly reflective at 633 nm and transmissive at 808 nm. A He–Ne laser beam was aligned to propagate through the crystal from the opposite side, passing the induced thermal lens, being reflected by mirror M2, and subsequently refocused by lens L2 with a focal length of 100 mm. The distance between the Nd:YAG crystal and the center of lens L2 was fixed at $D_2 = 325$ mm. The position of the He–Ne focal plane, located at a distance D_1 from lens L2, was determined using a CMOS camera mounted on a micrometer-precision translation stage.

As the absorbed pump power increased, the induced thermal lens modified D_1, which was measured at several pump powers [see Fig. 4.13(b)]. The corresponding thermal lens focal lengths F were then calculated as a function of the pump power [see Fig. 4.13(c)] using the ABCD matrix formalism. In this analysis, the optical system is modeled as a sequence consisting of an unknown thin lens of focal length F (representing the thermal lens), followed by free-space propagation of length D_2, a known thin lens with $f = 100$ mm, and a final free-space propagation of length D_1 (experimentally determined by the translation stage). The overall system is therefore represented by the following matrix multiplication:

$$M = P(D_1)\, L(f)\, P(D_2)\, L(F). \tag{4.21}$$

The standard ABCD matrices for free-space propagation and thin lenses are given by:

$$M = \begin{pmatrix} 1 & D_1 \\ 0 & 1 \end{pmatrix} \begin{pmatrix} 1 & 0 \\ -\dfrac{1}{f} & 1 \end{pmatrix} \begin{pmatrix} 1 & D_2 \\ 0 & 1 \end{pmatrix} \begin{pmatrix} 1 & 0 \\ -\dfrac{1}{F} & 1 \end{pmatrix} = \begin{pmatrix} A & B \\ C & D \end{pmatrix}, \tag{4.22}$$

where

$$A = \frac{-D_1F - D_1f + D_2(D_1 - f) + Ff}{Ff} \quad B = -\frac{D_1D_2}{f} + D_1 + D_2$$
$$C = \frac{D_2 - F - f}{Ff}, \qquad D = \frac{-D_2 + f}{f}. \tag{4.23}$$

If the incident beam has height x_1 and propagation angle θ_1, then after passing through the optical system:

$$\begin{pmatrix} x_2 \\ \theta_2 \end{pmatrix} = \begin{pmatrix} A & B \\ C & D \end{pmatrix} \begin{pmatrix} x_1 \\ \theta_1 \end{pmatrix}, \tag{4.24}$$

where the incident He–Ne beam is assumed to be collimated ($\theta_1 = 0$), and the observation plane located at a distance D_1 corresponds to the focal plane, i.e., the plane where the beam converges to a point ($x_2 = 0$). This focusing condition is fulfilled when the matrix element $A = 0$.

By setting $A = 0$, we obtain:

$$-D_1F - D_1f + D_2(D_1 - f) + Ff = 0. \tag{4.25}$$

Solving Eq. (4.25) for F, we obtain:

$$\boxed{F = \frac{D_1D_2 - D_1f - D_2f}{D_1 - f}}, \qquad (D_1 \neq f). \tag{4.26}$$

.

4.1.11 Angular Filtering Mirror Investigation

The angular filtering mirror (AFM) employed in Section 3.2 was characterized by measuring its transmission dependence on the angle of incidence (AOI) using a laser beam, as illustrated in Fig. 4.14. The laser beam emerging from the microchip cavity first passed through a filter that blocked the residual pump radiation at 808 nm while transmitting the lasing wavelength at 1064 nm. Subsequently, the beam propagated through a Glan–Prism polarizer that selected either the horizontally (a) or vertically (b) polarized component, depending on the prism orientation. The beam was then expanded by a plano–concave lens L_1 ($f_1 = -12$ mm) and a plano–convex lens L_2 ($f_2 = 100$ mm), increasing its diameter approximately fivefold and reducing its divergence from about 5 mrad to 0.5 mrad. The AFM was mounted on a motorized rotation stage providing AOI control with a precision of 0.02°. The transmitted power was

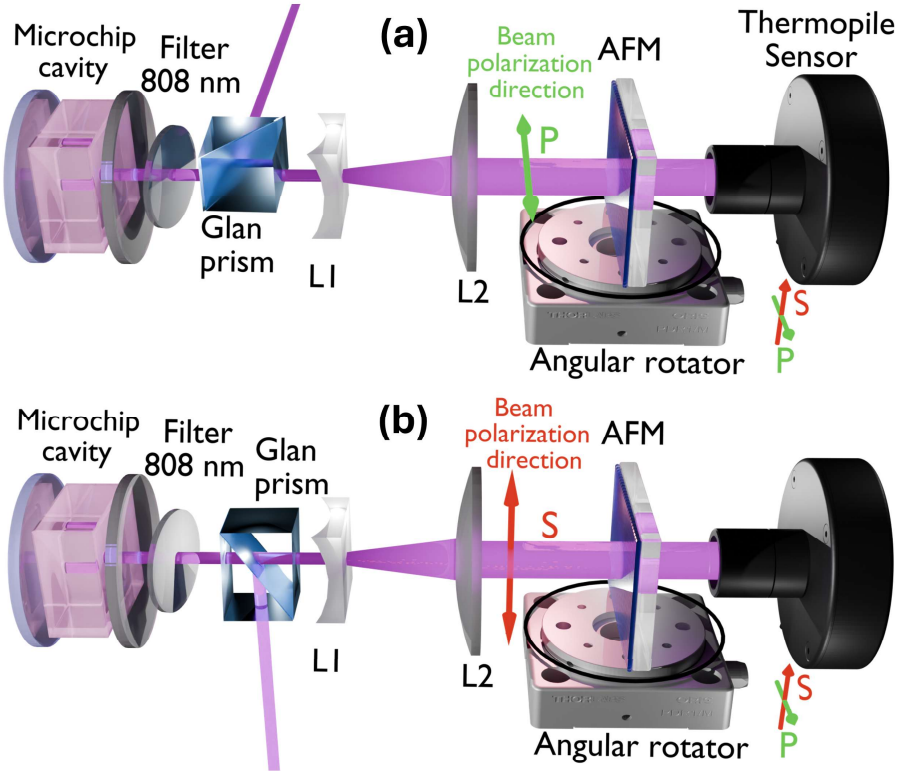


Figure 4.14: Experimental setup for measuring the angular filtering mirror (AFM) transmission versus angle of incidence (AOI). Panels (a) and (b) correspond to p- and s-polarized measurements, respectively.

recorded using a thermopile sensor and normalized to the incident power measured without the AFM. The measurement configurations for the p- and s-polarized components are shown in panels (a) and (b), respectively.

4.2 Analytical methods

In this section, the analytical methods employed for transverse-mode analysis are discussed; these methods were used primarily in Sec. 3.1. First, the analytical formulation based on the slowly varying envelope approximation (SVEA) is introduced, with emphasis on its range of validity and inherent limitations. Next, analytical expressions for thermal lenses are compared for top-hat and Gaussian pump profiles. Finally, the analytical form of the Laguerre–Gaussian beam is discussed, which serves as a reference for numerical evaluating the beam-quality factor M^2. The more extensive analytical content was moved to the Appendix to improve clarity for the reader.

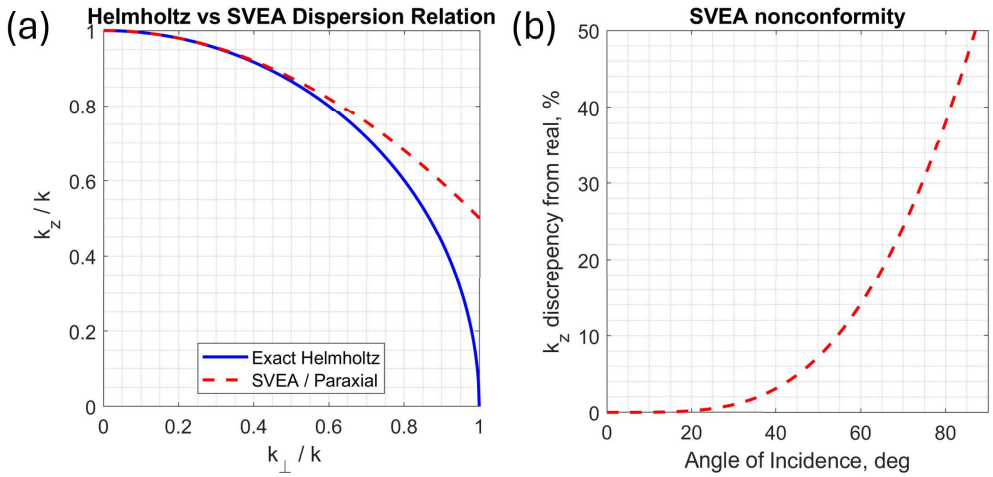


Figure 4.15: Dispersion relations of the Helmholtz equation and the Slowly Varying Envelope Approximation (SVEA), with the transverse wave vector $k_\perp$ and longitudinal component k_z normalized to the wavenumber $k = \frac{2\pi}{\lambda}$ (a). Relative discrepancy of the longitudinal component k_z (in percent) as a function of the angle of incidence (AOI) under the SVEA (b).

4.2.1 Paraxial Approximation

The slowly varying envelope approximation (SVEA) [59, p. 628], [200, p. 52]:

$$\nabla_\perp^2 A(x,y,z) + 2ik\frac{\partial A(x,y,z)}{\partial z} = 0, \tag{4.27}$$

which originates from the wave equation in vacuum (see the Appendix for details). The SVEA dispersion relation $k_z(k_\perp, k)$ [59, p. 659]:

$$k_z = k - \frac{k_\perp^2}{2k}, \quad k_\perp^2 = k_x^2 + k_y^2, \tag{4.28}$$

where the exact Helmholtz dispersion relation [59, p. 659]:

$$k_z = k\sqrt{1 - \frac{k_\perp^2}{k^2}} \tag{4.29}$$

The dispersion relation derived within the SVEA framework deviates from the exact Helmholtz solution and is therefore subject to limitations. In particular, for plane-wave eigenmodes with an angle of incidence larger than about 20°, the SVEA model shows a significant discrepancy from

the exact behavior (see Fig. 4.15). See the Appendix for details.

4.2.2 Thermal Lens Shapes in Longitudinally Pumped McL Crystal

Top hat and Gaussian pumping thermal load distribution can be represented in following equation [75]:

$$S(r,z) = Q_0 \exp(-\alpha z) \begin{cases} \exp\left(-2\dfrac{r^2}{w^2}\right), & \text{Gaussian pump,} \\ 1, \quad 0 \le r \le a, & \text{top-hat pump,} \\ 0, \quad a < r \le b, & \text{top-hat pump,} \end{cases} \tag{4.30}$$

where Q_0 is normalization constant, α is the pump absorption coefficient, a is the radius of the pumping beam, and b is the radius of the laser rod. The corresponding temperature distributions are [75]:

$$\Delta T(r,z) = \Delta T_0 \exp(-\alpha z) \begin{cases} \ln\left(\dfrac{b^2}{r^2}\right) + E_1\left(\dfrac{2b^2}{w^2}\right) - E_1\left(\dfrac{2r^2}{w^2}\right), & \text{Gaussian pump,} \\ 1 - \dfrac{r^2}{a^2} + \ln\left(\dfrac{b^2}{a^2}\right), \quad 0 \le r \le a, & \text{top-hat pump,} \\ \ln\left(\dfrac{b^2}{r^2}\right), \quad a < r \le b, & \text{top-hat pump,} \end{cases} \tag{4.31}$$

where $\Delta T(r,z) = T(r,z) - T(b,z)$ is the temperature difference from the crystal outer edge, ΔT_0 is the normalization constant, $E_1(u) = \int_1^\infty \frac{e^{-ut}}{t}\, dt$. We assume that $\Delta n = \frac{\partial n}{\partial T}\, \Delta T$, and $\frac{\partial n}{\partial T}$ is constant.

Figure 4.16 shows the Gaussian and Top-Hat pump intensity profiles together with the corresponding induced refractive index modulation $\Delta n(r)$ as a function of the radial distance r, for beam radii $a = w = 150\ \mu$m and a crystal aperture of $b = 1$ mm. Parabolic approximations are applied in the region $r < a$ (panel b), while deviations from the parabolic shape become significant for $r > a$. The refractive index modulation profiles are qualitatively similar for both Top-Hat and Gaussian pump beams; for a Super-Gaussian pump, the resulting $\Delta n(r)$ is expected to

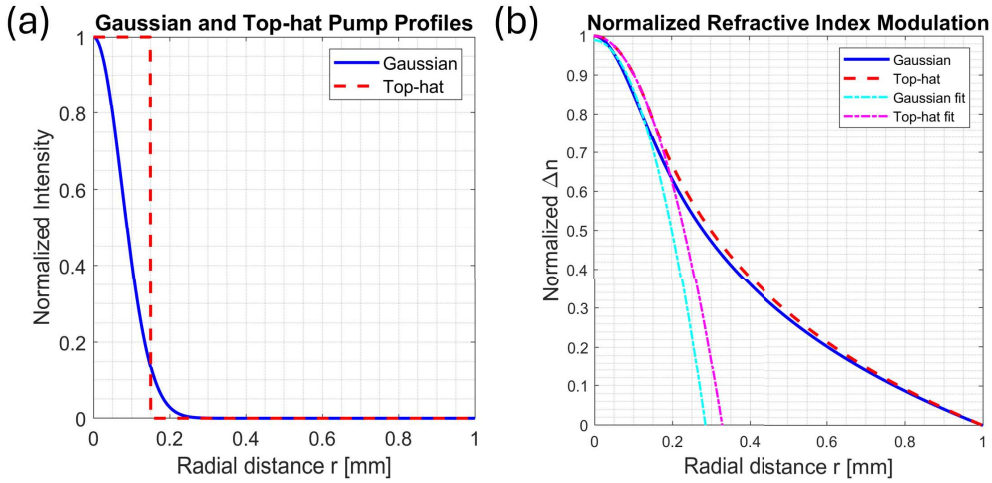


Figure 4.16: Gaussian and Top-Hat pump intensity profiles (a) and the corresponding induced refractive index modulation $\Delta n(r)$ (b) as a function of the radial distance r.

lie between these two cases.

4.2.3 Gaussian-Laguerre Beams

Gaussian-Laguerre Beams are described with equation [127]:

$$\mathcal{E}_p^l(r,\phi,z) = \mathcal{E}_0 \frac{w_0}{w(z)} \left(\frac{\sqrt{2}r}{w(z)}\right)^l L_p^l\left(\frac{2r^2}{w^2(z)}\right) \exp\left(-\frac{r^2}{w^2(z)}\right) \times \exp\left[-ikz - ik\frac{r^2}{2R(z)} + il\phi + i(2p+l+1)\psi(z)\right], \tag{4.32}$$

where the physical quantities $w(z)$, $R(z)$, $\zeta(z)$, θ, z_R, k are related in following expressions:

$$w(z) = w_0\sqrt{1+\left(\frac{z}{z_R}\right)^2}, \tag{4.33}$$

$$R(z) = z\left[1+\left(\frac{z_R}{z}\right)^2\right], \tag{4.34}$$

$$\zeta(z) = \arctan\left(\frac{z}{z_R}\right), \tag{4.35}$$

$$\theta = \frac{\lambda}{\pi w_0}, \tag{4.36}$$

$$z_R = \frac{\pi w_0^2}{\lambda}, \tag{4.37}$$

$$k = \frac{2\pi}{\lambda}. \tag{4.38}$$

The symbol notations are explained in table 4.1. The beam radius

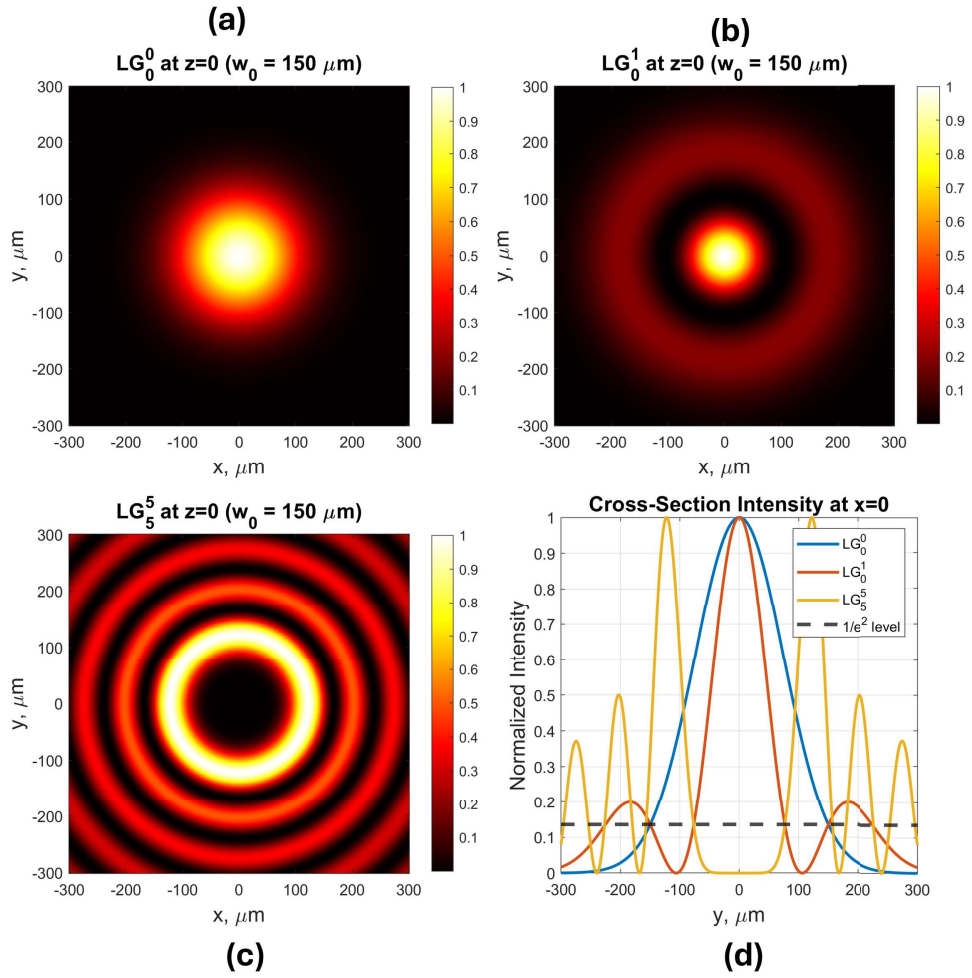


Figure 4.17: Transverse cross-sections (XY plane) at $z = 0$ for a Gaussian beam (a) and Laguerre–Gaussian modes LG_0^1 (b) and LG_5^5 (c), all with the same beam waist $w_0 = 150\,\mu$m. Panel (d) shows the corresponding one-dimensional cross-sections at $z = 0$ along the line $y = 0$.

$w(z)$ and waist radius w_0 are the same for each mode of different p and l indexes. However, practical meaning $w(z)$ has only for fundamental gaussian mode (p,l=0), where it can be experimentally, numerically and analytically be estimated at height $1/e^2$ of its intensity peak. Higher order mode intensity is modulated at radial coordinate, where its ripples can cross the height of $1/e^2$ intensity peak, leading to unclear meaning.

The Gaussian beam and Laguerre-Gaussian beam LG_0^1, LG_5^5 cross-sections XY at z=0 (caustica) with the same beam waist $w_0 = 150\mu m$ are depicted in fig.4.17. The derivation of the Gaussian–Laguerre beam from the SVEA, together with an ideal thermal-lens constraint in the microchip cavity, is provided in the Appendix.

4.2.4 Macroscopic Maxwell–Bloch equations for McL with AFM

The macroscopic Maxwell–Bloch equations originated in the laser pattern-formation and nonlinear-dynamics community [142, 143, 194] and have previously been applied to microchip laser systems [132]. The equations couple the classical wave equation for the complex electric field E with two material equations that provide a macroscopic description of the polarization P and the population inversion D in the active medium [143, Ch. 5]. The macroscopic quantities P and D originate from the underlying quantum-mechanical description of light–matter interaction. In this framework, the classical dipole moment is replaced by the expectation value of the dipole moment, which determines the medium polarization P [143, p. 104]. The population inversion D is given by the difference in the occupation probabilities of the excited and ground electronic states [143, p. 105].

We employ an equation set closely related to those presented in [132, 194], [143, p. 118], and [142, p. 36], adapted here to describe our microchip laser incorporating an AFM:

$$\frac{\partial E}{\partial t} = \left[-(1+i\omega_0) + ia\nabla_\perp^2 + iV(\mathbf{r}_\perp) + \hat{F}(\nabla_\perp)\right] E + P\,, \tag{4.39a}$$

$$\frac{\partial P}{\partial t} = -\gamma_\perp (P - ED), \tag{4.39b}$$

$$\frac{\partial D}{\partial t} = -\gamma_\parallel \left(D - D_0(\mathbf{r}_\perp) + \frac{EP^* + E^*P}{2} \right), \tag{4.39c}$$

The complex fields $E(r,t)$ and $P(r,t)$ are the envelopes of the electromagnetic (optical) field and the polarization, respectively, while $D(r,t)$ is the real-valued field of the population inversion, which in the absence of stimulated radiation is equal to its unsaturated value $D_0(r)$ [142, p. 36].

The polarization and population-inversion decay rates $\gamma_\perp$ and $\gamma_\parallel$ are intrinsic properties of the active medium, corresponding to the gain bandwidth and the fluorescence lifetime, respectively. In our case, the active material was Nd:YAG, for which the gain bandwidth and fluorescence lifetime are reported in [16, p. 55].

The terms that specifically describe a microchip laser cavity are $ia\nabla_\perp^2$, $iV(r_\perp)$, and $\hat{F}(\nabla_\perp)$. The diffraction term $ia\nabla_\perp^2$ accounts for the paraxial propagation of the electric field inside the cavity, where the diffraction coefficient a depends on the cavity length and the laser wavelength. The term $iV(r_\perp)$ introduces a phase modulation determined by the thermally induced lens. Finally, the operator $\hat{F}(\nabla_\perp)$ represents the angular-filtering action of the AFM and is introduced phenomenologically to reproduce the far-field transmission profile, matched to the experimentally measured angular transmission of the AFM.

4.2.5 Linear field equation

The macroscopic Maxwell–Bloch equations [142, p. 36] (see Eq. 4.39) are nonlinear and involve two material variables: the polarization P and the population inversion D. A significant simplification of the model is achieved by assuming that both P and D evolve on timescales much faster than the optical field E, which enables their adiabatic elimination. Under this assumption, the field dynamics reduces to [142, p. 37]

$$\frac{\partial E}{\partial t} = \rho\, E + i\,(a\nabla^2 - \omega)\, E - E\,|E|^2, \tag{4.40}$$

where the parameter ρ represents the balance between gain and loss in the laser resonator. Equation 4.40 is known as the Ginzburg–Landau equation and remains nonlinear due to the gain-saturation term $E|E|^2$.

In the present study (see Sec. 3.1), we further simplify this equation by considering operation close to the generation threshold, where gain saturation can be neglected. Accordingly, the nonlinear term is omitted, $E|E|^2 \to 0$. In addition, we assume zero detuning, $\omega \to 0$. Within this linear approximation, the modified electric field is denoted by A, and the governing equation becomes

$$\frac{\partial A}{\partial t} = -\rho\, A + id\nabla^2 A + i\sigma(r)\, A + \gamma(r)\, A, \tag{4.41}$$

where the spatial modulations of the refractive index $\sigma(r)$ and the gain

$\gamma(r)$ are introduced into the linear field equation.

4.3 Numerical methods

4.3.1 Evaluation of Transverse Mode Eigenfrequencies

This section describes the methodology employed to numerically determine the transverse-mode eigenfrequencies. The numerically obtained values were later used in Section 3.1 for the evaluation of the beam-quality factors. All computations were performed using the *Mathematica* software package (Wolfram Research, Inc.) [201].

The task is to solve the Bessel transcendental equation:

$$\frac{\alpha\, J_{l-1}(\alpha)}{J_l(\alpha)} = -\frac{\beta\, K_{l-1}(\beta)}{K_l(\beta)}, \tag{4.42}$$

where α and β are complex eigenvalues to be determined. The functions $J_l(x)$ and $K_l(x)$ denote the Bessel function of the first kind and the modified Bessel function of the second kind, respectively. The coefficient l is the azimuthal mode number and must be an integer to satisfy the physical periodicity condition $e^{2\pi i l} = 1$, ensuring field continuity after a full 2π rotation.

Both $J_l(x)$ and $K_l(x)$ are transcendental functions defined analytically through related, but distinct, differential equations:

$$x^2\frac{d^2y}{dx^2} + x\frac{dy}{dx} + \left(x^2 - l^2\right) y = 0, \tag{4.43}$$

$$x^2\frac{d^2y}{dx^2} + x\frac{dy}{dx} - \left(x^2 + l^2\right) y = 0, \tag{4.44}$$

where the azimuthal number l appears squared, making the equation independent of its sign and restricting the eigen-solution set to non-negative integers $l = 0, 1, 2, \ldots$. The function $J_l(\alpha)$ exhibits oscillatory behavior, whereas $K_l(\beta)$ decays exponentially.

The functions $J_l(\alpha)$ and $K_l(\beta)$ were numerically evaluated over a broad parameter space (l, α, β). Both arguments α and β in Eq. 4.42

were allowed to vary in the complex plane, being physically determined by the pump-induced gain and the thermally induced phase modulation. The pumping effect was expressed through the complex parameter ζ introduced in Eq. 3.7, where the corresponding eigenvalues were calculated as $\alpha = \sqrt{\zeta^2 - \beta^2}$ and $\beta = \sqrt{\zeta^2 - \alpha^2}$. Then the Eq. 4.42 can be expressed for ζ and β:

$$\frac{\sqrt{\zeta^2 - \beta^2}\, J_{l-1}\left(\sqrt{\zeta^2 - \beta^2}\right)}{J_l(\sqrt{\zeta^2 - \beta^2})} = -\frac{\beta\, K_{l-1}(\beta)}{K_l(\beta)}. \tag{4.45}$$

Numerical solutions of Eq. 4.45 were obtained using the *FindRoot* function. The method relies on local linearization of the function and exhibits quadratic convergence near the solution, making it highly efficient when an appropriate initial guess is chosen. However, convergence is highly sensitive to the starting point: unsuitable initial estimates may lead to divergence or convergence toward unintended roots.

In this work, the initial complex values of β were iteratively adjusted for both their real and imaginary components within a selected range of ζ. Each ζ value corresponds to several possible β solutions, representing different radial mode numbers m. Depending on the chosen initial guess, the algorithm converges to one or another transverse mode associated with a specific m. The procedure was initialized along a random line in the complex plane representing the initial set of β values for a given ζ. The resulting solutions were analyzed graphically to identify regions exhibiting smooth and physically consistent behavior. Based on these observations, the initial-guess curve was refined iteratively according to the local slope indicated by the graphical results. This process was repeated until stable eigen-solutions corresponding to the selected radial orders m were obtained. Additional checks were performed between adjacent solution regions to ensure that no modes were missed.

4.3.2 Beam quality M^2 of single modes calculation in McL

This section describes the methodology employed to numerically determine the single mode beam quality M^2 from phase and amplitude distribution in the transverse plane of the particular mode electrical field $A(\xi, \phi)$ given in Eq. 3.2 and Eq. 4.46 in polar coordinate system:

$$\begin{cases} A(\xi,\phi) = J_l(\alpha\xi)\, e^{i\phi l} & \text{if} \quad \xi < 1; \\ A(\xi,\phi) = \frac{J_l(\alpha)}{K_l(\beta)} K_l(\beta\xi)\, e^{i\phi l} & \text{if} \quad \xi > 1. \end{cases} \tag{4.46}$$

Here, $\xi = r/R$ is the normalized radial coordinate, where r is the physical radius and R is the pump radius, while ϕ denotes the azimuthal angle.

The calculation of the beam quality factor M^2 would be straightforward if the electric field were located at the waist plane, allowing the use of the well-known relation $M^2 = 4\pi\sigma_0\sigma_s$ [202], where σ_0^2 and σ_s^2 are the second moments of the field in the spatial and Fourier domains, respectively. However, in the present case the field distribution is complex (since the coefficients α and β are complex) and defined outside the waist region. An analytical approach for evaluating the beam quality factor in two dimensions outside the waist was proposed by H. Yoda, P. Polynkin, and M. Mansuripur [149], formulated in Cartesian coordinates. In brief, the method involves calculating the first and second spatial moments in the Cartesian coordinate system (x, y):

$$\begin{aligned} \langle x \rangle &= \int\int x dx dy |A(x,y)|^2, \\ \langle y \rangle &= \int\int y dx dy |A(x,y)|^2, \end{aligned} \tag{4.47}$$

$$\begin{aligned} \sigma_x^2 &= \int\int dx dy \left(x - \langle x \rangle\right)^2 |A(x,y)|^2, \\ \sigma_y^2 &= \int\int dx dy \left(y - \langle y \rangle\right)^2 |A(x,y)|^2. \end{aligned} \tag{4.48}$$

Additionally, the auxiliary integrals $A_{x,y}$ and $B_{x,y}$ should be evaluated (see in appendix section). The quantities $A_{x,y}$, $B_{x,y}$, and $\sigma_{x,y}^2$ are

substituted into the final expressions for M_x^2 and M_y^2:

$$\begin{aligned} M_x^2 &= \sqrt{4B_x\sigma_x^2 + A_x^2}, \\ M_y^2 &= \sqrt{4B_y\sigma_y^2 + A_y^2}. \end{aligned} \tag{4.49}$$

The final beam quality factor is then:

$$M^2 = \sqrt{M_x^2 M_y^2}. \tag{4.50}$$

In our case, the electric field was expressed in polar coordinates (ξ, ϕ), and the auxiliary integrals A and B were modified accordingly and evaluated explicitly (see the Appendix for details).

Due to the multi-step procedure and computational complexity involved, there is a possibility that numerical inaccuracies or implementation errors could affect the estimated beam quality factor M^2. To validate the computational method, identical calculations were performed for Laguerre–Gaussian modes, whose beam quality factor M^2 is well known [203]. It is expressed in terms of the mode indices p and l as

$$M_{p,l}^2 = 2p + l + 1, \tag{4.51}$$

and remains invariant whether the beam is near the waist (caustic), within the Rayleigh range, or far beyond it. The same computational procedure used for the Bessel-type fields defined in Eq. 4.46 was applied to the Laguerre–Gaussian modes. The numerically obtained M^2 values for Laguerre–Gaussian beams, both within and outside the waist region, agreed very closely with the analytical expression in Eq. 4.51. This agreement was maintained over a wide range of propagation distances z and beam waist sizes, as well as for different combinations of mode indices (p, l).

Main Results

1. A nano-modulated thin-film angle filtering mirror (AFM) with reflectance strongly dependent on the incidence angle was designed, fabricated, and implemented as an output coupler in a microchip laser cavity.

   (a) **An experimental increase of beam quality factor M^2 was demonstrated compared to a conventional plane-mirror outcoupler.**

   (b) **An experimental increase of brightness by approximately two times was demonstrated compared to a conventional plane-mirror outcoupler.**

   (c) **Numerical simulations within the single-longitudinal-mode approximation supported the experimental observations and indicate that two-dimensional angular filtering is not fundamentally limited to a twofold brightness enhancement.**

2. A nano-modulated polarizing Meta-Mirror output coupler was developed and implemented in a Nd:YAG microchip laser in combination with polarized pumping. The polarization contrast dynamics were investigated as a function of absorbed pump power and the relative orientation between the pump polarization, the Meta-Mirror axis, and the orthogonal polarization axes induced in the crystal by mechanical stress.

   (a) **A polarization contrast ratio exceeding 1000 was ex-**

perimentally demonstrated up to an absorbed pump power of approximately 1 W using either the Meta-Mirror or polarized pumping.

(b) **Beyond this threshold, only the Meta-Mirror configuration sustained a high polarization contrast, whereas the polarization contrast obtained using polarized pumping alone decreased sharply.**

(c) **The Meta-Mirror configuration exhibited significantly lower sensitivity to changes in the pump polarization direction compared to a conventional isotropic output coupler.**

(d) **The polarization direction of the output laser beam strictly followed the orientation of the Meta-Mirror.**

(e) **A slight improvement of the beam quality factor M^2, output power, and overall brightness was experimentally observed in comparison with a conventional plane-mirror outcoupler.**

3. A practical theoretical model based on two-dimensional linear field equations was developed to describe transverse modes and to estimate the beam quality factor M^2 in microchip lasers with cylindrically symmetric gain and refractive-index profiles.

   (a) **The transverse-mode structure and corresponding eigenvalues were calculated for axisymmetric gain and thermally induced refractive-index profiles.**

   (b) **The transverse eigenvalue problem was formulated and solved in a form mathematically analogous to a Schrödinger-type equation with a complex potential.**

   (c) **The beam quality factor M^2 was evaluated directly from the calculated electric-field distributions.**

   (d) **The theoretically predicted M^2 values were experimentally verified.**

Conclusions

1. Intracavity angular filtering by reflection using a nano-modulated angle filtering mirror (AFM) provides an efficient method for enhancing the spatial quality of microchip laser radiation.

   (a) **Brightness enhancement is achieved using an ultra-thin structure (hundreds of nanometers in thickness), enabling its implementation in ultra-short laser cavities.**

   (b) **The AFM does not introduce additional absorption losses, as indicated by the unchanged lasing threshold.**

   (c) **The AFM performs spatial filtering in the angular domain rather than by spatial truncation, and therefore does not introduce aperture-induced diffraction losses.**

   (d) **Two-dimensional angular filtering is able to further increase the brightness enhancement.**

2. Intracavity polarization filtering by reflection using a polarizing Meta-Mirror provides an efficient approach for enhancing the polarization properties of a Nd:YAG-based microchip laser:

   (a) **The Meta-Mirror does not introduce additional absorption losses, as evidenced by the unchanged lasing threshold.**

   (b) **The Meta-Mirror approach operates independently of polarized pumping and is fully compatible with**

multimode, unpolarized fiber-coupled pump sources.

(c) **Polarized pumping alone is insufficient to maintain high polarization contrast at elevated pump powers, whereas the Meta-Mirror sustains high polarization contrast.**

(d) **The Meta-Mirror significantly reduces sensitivity to variations in pump polarization direction.**

(e) **Polarization filtering by reflection simultaneously improves spatial beam parameters and overall brightness.**

3. The developed theoretical model provides a practical tool for predicting the beam quality factor M^2 in microchip lasers.

(a) **The transverse-mode problem in microchip lasers can be treated using a semi-analytical approach.**

(b) **The beam quality factor M^2 can be evaluated, linking theoretical modal analysis with experimentally measurable resonator parameters.**

(c) **The agreement between theory and experiment confirms the validity of the model for practical beam-quality estimation in microchip laser systems.**

Appendix

Paraxial Approximation

Table 4.1: Key symbols and descriptions for laser beams

Symbol	**Description**
w	Monochromatic wave angular frequency
c	Speed of light
λ	Monochromatic wave wavelength
n	Refractive index
k	Wave number, defined as $2\pi n/\lambda$.
$E(\mathbf{r}, t)$	Physical electric field of a monochromatic wave.
$\mathcal{E}(\mathbf{r})$	Electrical field spatial envelope. Relation with electrical field $E(\mathbf{r}, t) = \mathcal{E}(\mathbf{r})e^{-i\omega t}$
$A(\mathbf{r})$	Slowly varying electrical field spatial envelope. Relation with electrical field $E(\mathbf{r}, t) = A(\mathbf{r})e^{i(kz-\omega t)}$
$\mathcal{E}_0$	Electric field spatial envelope amplitude.
w_0	Beam waist radius (minimum beam radius at $z = 0$).
$w(z)$	Beam radius at position z along the propagation axis.
$R(z)$	Radius of curvature of the phase front at position z.
$\psi(z)$	Gouy phase shift of the propagating beam.

Table 4.1: Key symbols and descriptions for Laguerre–Gaussian modes (continued)

Symbol	**Description**
z_R	Rayleigh length, the distance over which the beam radius approximately doubles.
r	Radial coordinate in cylindrical coordinates.
ϕ	Azimuthal angle in cylindrical coordinates.
p	Radial mode index (number of radial intensity nodes).
l	Azimuthal mode index (topological charge, corresponding to orbital angular momentum).
L_p^l	Generalized Laguerre polynomial of order p and azimuthal index l.

We start with the scalar wave equation in vacuum [200, p. 38]:

$$\nabla^2 E(\mathbf{r},t) - \frac{1}{c^2}\frac{\partial^2 E(\mathbf{r},t)}{\partial t^2} = 0. \tag{4.52}$$

Assuming a monochromatic wave of angular frequency ω:

$$E(\mathbf{r},t) = \mathcal{E}(\mathbf{r})e^{-i\omega t}, \tag{4.53}$$

we obtain the Helmholtz equation for the electrical field spatial envelope [59, p. 626], [200, p. 40], [204, p. 52]:

$$\nabla^2 \mathcal{E}(\mathbf{r}) + k^2 \mathcal{E}(\mathbf{r}) = 0, \quad k = \frac{\omega}{c}. \tag{4.54}$$

For a beam propagating predominantly along the z-axis, we write [59, p. 627]

$$\mathcal{E}(x,y,z) = A(x,y,z)e^{ikz}, \tag{4.55}$$

where $A(x,y,z)$ is the slowly varying envelope and e^{ikz} is the carrier .

The Laplacian of $\mathcal{E}$ is

$$\nabla^2 \mathcal{E} = \frac{\partial^2 \mathcal{E}}{\partial z^2} + \frac{\partial^2 \mathcal{E}}{\partial x^2} + \frac{\partial^2 \mathcal{E}}{\partial y^2}. \tag{4.56}$$

Substituting $\mathcal{E} = Ae^{ikz}$ gives

$$\frac{\partial^2 \mathcal{E}}{\partial z^2} = e^{ikz} \left(\frac{\partial^2 A}{\partial z^2} + 2ik \frac{\partial A}{\partial z} - k^2 A \right), \tag{4.57}$$

and

$$\frac{\partial^2 \mathcal{E}}{\partial x^2} + \frac{\partial^2 \mathcal{E}}{\partial y^2} = e^{ikz} \nabla_\perp^2 A, \tag{4.58}$$

where $\nabla_\perp^2 = \frac{\partial^2}{\partial x^2} + \frac{\partial^2}{\partial y^2}$ is the transverse Laplacian. Inserting these into the Helmholtz equation:

$$e^{ikz} \left(\frac{\partial^2 A}{\partial z^2} + 2ik \frac{\partial A}{\partial z} + \nabla_\perp^2 A \right) = 0. \tag{4.59}$$

Under the slowly varying envelope approximation (SVEA), we neglect $\partial^2 A / \partial z^2$ compared to $2ik\, \partial A / \partial z$, yielding the paraxial wave equation [59, p. 628], [200, p. 52]:

$$\nabla_\perp^2 A(x, y, z) + 2ik \frac{\partial A(x, y, z)}{\partial z} = 0. \tag{4.60}$$

This equation describes the evolution of a slowly varying beam envelope along the propagation direction z. Assume a separable form:

$$A(x, y, z) = X(x)\, Y(y)\, Z(z). \tag{4.61}$$

Substituting (4.61) into (4.60) gives:

$$i \frac{Z'}{Z} = -\frac{1}{2k} \left(\frac{X''}{X} + \frac{Y''}{Y} \right). \tag{4.62}$$

Since the left-hand side depends only on z and the right-hand side only on x, y, each side must equal a constant. Introduce separation constants k_x, k_y:

$$\frac{X''}{X} = -k_x^2, \qquad (4.63) \qquad\qquad \frac{Y''}{Y} = -k_y^2. \qquad (4.64)$$

Thus

$$i\,\frac{Z'}{Z} = \frac{k_x^2 + k_y^2}{2k}. \qquad (4.65)$$

The solution of each separable is then:

$$X(x) = C_x e^{ik_x x}, \qquad (4.66) \qquad\qquad Y(y) = C_y e^{ik_y y}, \qquad (4.67)$$

$$Z(z) = C_z \exp\left(-i\frac{k_x^2 + k_y^2}{2k} z\right). \qquad (4.68)$$

A single eigen-solution labeled by (k_x, k_y) is

$$A_{k_x,k_y}(x, y, z) = C\,\exp[i(k_x x + k_y y)]\,\exp\left(-i\frac{k_x^2 + k_y^2}{2k} z\right). \qquad (4.69)$$

Because plane waves form a complete basis, the general solution is a superposition [204, pp. 74–78]:

$$A(x, y, z) = \frac{1}{(2\pi)^2} \iint_{-\infty}^{\infty} \tilde{A}(k_x, k_y)\,\exp[i(k_x x + k_y y)]\,\exp\left(-i\frac{k_x^2 + k_y^2}{2k} z\right) dk_x\, dk_y \qquad (4.70)$$

where $\tilde{A}(k_x, k_y)$ is the angular spectrum, i.e. the Fourier transform of the initial field [204, p. 74]:

$$\tilde{A}(k_x, k_y) = \iint_{-\infty}^{\infty} A(x, y, 0)\, e^{-i(k_x x + k_y y)}\, dx\, dy. \qquad (4.71)$$

Electrical field spatial envelope for single eigen-solution is then:

$$\mathcal{E}_{k_x,k_y}(x, y, z) = A_{k_x,k_y}(x, y, z) e^{ikz} = C\,\exp[i(k_x x + k_y y)]\,\exp\left(iz\left[k - \frac{k_x^2 + k_y^2}{2k}\right]\right). \qquad (4.72)$$

The general solution of spatial envelope is then following [204, pp. 74–78]:

$$\mathcal{E}(x,y,z) = \frac{1}{(2\pi)^2} \iint_{-\infty}^{\infty} \tilde{\mathcal{E}}(k_x,k_y)\, \exp[i(k_x x + k_y y)]\, \exp\left(iz \left[k - \frac{k_x^2 + k_y^2}{2k} \right] \right) dk_x\, dk_y \tag{4.73}$$

The angular spectrum of spatial envelope is Fourier transform of initial field (identical as in Eq. (4.71)) :

$$\tilde{\mathcal{E}}(k_x,k_y) = \iint_{-\infty}^{\infty} \mathcal{E}(x,y,0)\, e^{-i(k_x x + k_y y)}\, dx\, dy. \tag{4.74}$$

The dispersion relation $k_z(k_\perp, k)$ of SVEA [59, p. 659] is clearly to be identified from Eq. (4.73):

$$k_z = k - \frac{k_\perp^2}{2k}, \quad k_\perp^2 = k_x^2 + k_y^2 \tag{4.75}$$

The rejection of term $\partial^2 A/\partial z^2$ in equation (4.59) leads to changed SVEA dispersion relation in accordance to Helmholtz wave equation dispersion relation. The solutions of Helmholtz equation (4.54) are plane waves:

$$\mathcal{E}(x,y,z) = e^{i(k_x x + k_y y + k_z z)}. \tag{4.76}$$

Substituting into Eq. (4.54) gives the exact Helmholtz dispersion relation [59, p. 659]:

$$k_x^2 + k_y^2 + k_z^2 = k^2 \quad \Rightarrow \quad k_z = k\sqrt{1 - \frac{k_\perp^2}{k^2}}, \quad k_\perp^2 = k_x^2 + k_y^2. \tag{4.77}$$

The Taylor expansion of Helmholtz dispersion relation:

$$k_z = k\sqrt{1 - \frac{k_\perp^2}{k^2}} = k\left[1 - \frac{1}{2}\frac{k_\perp^2}{k^2} - \frac{1}{8}\left(\frac{k_\perp^2}{k^2} \right)^2 - \dots \right] \approx k - \frac{k_\perp^2}{2k} \tag{4.78}$$

The approximated dispersion relation of Helmholz wave equation in Eq. (4.78) is exactly the dispersion relation of SVEA in Eq. (4.78). Thus, the SVEA/paraxial approximation corresponds to the first-order Taylor expansion of the exact Helmholtz dispersion relation.

Phase Modulation by Lens: First- and Two-Step Approximations

The sag (height) of spherical surface expressed in cylindrical coordinates:

$$s(r) = R - \sqrt{R^2 - r^2}, \quad r = \sqrt{x^2 + y^2}. \tag{4.79}$$

Applying Taylor expansion when $r \ll R$ [200, p. 170]:

$$s(r) = \frac{r^2}{2R} + \frac{r^4}{8R^3} + \frac{r^6}{16R^5} + \frac{5r^8}{128R^7} + O\left(\frac{r^{10}}{R^9}\right). \tag{4.80}$$

By retaining only the first-order term from Eq. (4.80), and taking into account that, for a mirror, the incident wave travels twice the sagitta distance, while using the relation between the focal length of a spherical lens F and the mirror radius $R = 2F$, the phase modulation introduced by both the spherical mirror in reflection and the spherical lens in transmission can be approximated as [59, p. 786], [204, p. 83]:

$$\Phi_{mirror}(r) = 2k\, s(r) \approx k\frac{r^2}{R}, \quad \Phi_{lens}(r) \approx k\frac{r^2}{2F}. \tag{4.81}$$

Please note that the elements are considered as thin where the phase modulation takes place in plane surface. The slowly varying envelope changes then passing the plane from z_0^- to z_0^+ as follows [59, p. 786], [204, p. 83]:

$$A(z_0^+, r) = A(z_0^-, r) \exp\Big(-ik\frac{r^2}{2F}\Big). \tag{4.82}$$

When the phase shift is small $\left|\frac{kr^2}{R}\right| \ll 1$, we can linearize the exponential using the first-order Taylor expansion:

$$\exp\Big(-ik\tfrac{r^2}{R}\Big) \approx 1 - ik\tfrac{r^2}{2F} \tag{4.83}$$

Then, the phase modulation $V(r)$ can be expressed as follows:

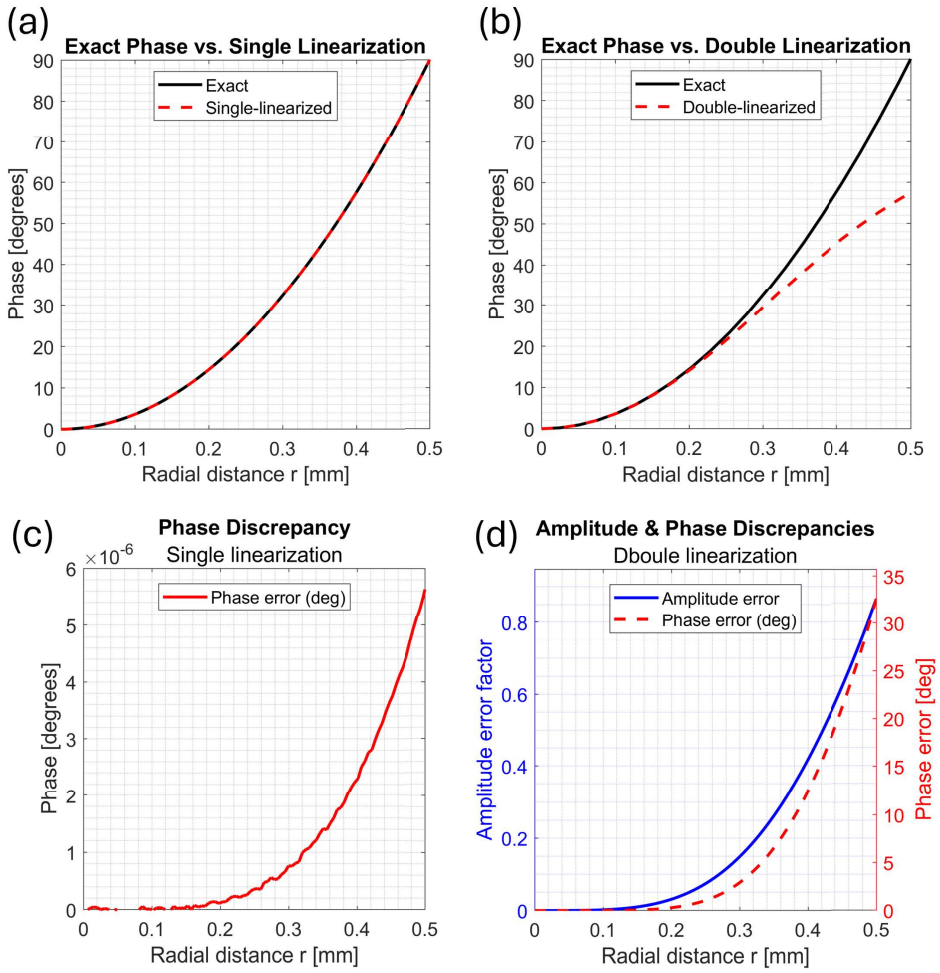


Figure 4.18: The phase modulation induced by a spherical lens with focal length $F = 0.5$ m, or by spherical mirror with radius of curvature $R = 1$ m, at a wavelength of $\lambda = 1$ μm is shown as a function of radial distance r, together with comparisons to first(a)- and two-step (b) linearized approximations. The first linearization is defined in Eq. (4.81), while the two-step linearization applies both Eq. (4.81) and Eq. (4.83). The single linearization yields a phase error approximately six orders of magnitude smaller (c) than that obtained with the two-step approach (d). In addition, the two-step linearization also alters the amplitude (d), leading to pronounced discrepancies in both phase and amplitude for radial distances exceeding $r > 200\,\mu$m.

$$A(z_0^+, r) \approx A(z_0^-, r)\left(1 - i\frac{kr^2}{2F}\right), \quad V(r) = 1 - i\frac{kr^2}{2F}. \tag{4.84}$$

By using the approximation in Eq. (4.83), both complex amplitude and

phase are perturbed:

$$\Delta\big|A(z_0^+, r)\big| = \Big|A(z_0^-(r))\Big| \left(\sqrt{1 + \left(k\tfrac{r^2}{2F}\right)^2} - 1\right) \tag{4.85}$$

$$\Delta \arg\big(A(z_0^+, r)\big) = 2ks(r) - \arctan\Big(k\tfrac{r^2}{2F}\Big). \tag{4.86}$$

As an example, the phase modulation induced by a spherical mirror with a radius of curvature $R = 1\,\mathrm{m}$ at a wavelength of $\lambda = 1\,\mu\mathrm{m}$ is shown in Fig. 4.18 as a function of the radial distance r, together with the first-order approximation (Eq. (4.81)) and the two-step linearized approximation (Eqs. (4.81) and (4.83)). It can be observed that the second step of linearization introduces a phase error approximately six orders of magnitude larger than that of the first-order case. The limitations of the two-step linearization should therefore be taken into account. In this work, we experimentally investigate microchip lasers with a typical intracavity beam radius in the range of 100–200 μm.

Gaussian-Laguerre Beams under SVEA and Thermal Lens Constraint in Microchip Cavity

If connecting beam propagation under SVEA with approximated ideal parabolic thermal lens, one can constrain the resonator equation, which takes no amplification into the account. Then such equation in cylindrical coordinates becomes very similar as described in [6, 133, 135]:

$$\frac{\partial A(r,\phi,t)}{\partial t} = \frac{iL}{k}\nabla_\perp^2 A(r,\phi,t) - \frac{ikr^2}{F}A(r,\phi,t), \tag{4.87}$$

applying the Ansatz $A(r,\phi,t) = A(r,\phi)e^{i\omega t}$:

$$\left[\frac{L}{k}\nabla_\perp^2 - \frac{kr^2}{F} - \omega\right] A(r,\phi) = 0, \tag{4.88}$$

where L is cavity length. The 2D Laplacian in polar coordinates $\nabla_\perp^2 = \partial_r^2 + \frac{1}{r}\partial_r + \frac{1}{r^2}\partial_\varphi^2$, and separate variables in radial and angular parts:

$$A(r,\varphi) \;=\; R_l(r)\, e^{il\varphi}. \tag{4.89}$$

Then

$$R_l'' + \frac{1}{r}R_l' - \frac{l^2}{r^2}R_l - \frac{k^2}{FL}\, r^2 R_l - \frac{k}{L}\,\omega\, R_l = 0. \tag{4.90}$$

where we introduced

$$\gamma^2 := \frac{k^2}{FL}, \qquad \beta := \frac{k}{L}\,\omega \tag{4.91}$$

We use following notations and Gaussian Ansatz:

$$\rho := \gamma r^2, \qquad s := |l|, \qquad R_l(r) \;=\; r^s\, e^{-\rho/2}\, v(\rho), \tag{4.92}$$

After introducing the Gaussian Ansatz we receive the equation for $v(\rho)$:

$$\rho\, v'' + (\, s + 1 - \rho\,)v' + \Big(-\frac{\beta}{2\gamma} - \frac{s+1}{2}\Big)v = 0, \tag{4.93}$$

which is Laguerre-Gaussian generalized differential equation. Polynomial solutions occur when the last coefficient equals a nonnegative integer p:

$$-\frac{\beta}{2\gamma} - \frac{s+1}{2} = p\,, \qquad p = 0, 1, 2, \dots\,, \qquad \omega = -\,\frac{L}{k}\,\gamma\,(2p + |l| + 1).$$

Then the solution is following:

$$A_{p,l}(r,\varphi) = C_{p,l}\; r^{|l|} \exp\Big(-\tfrac{r^2}{w^2}\Big)\, L_p^{|l|}\big(\frac{2r^2}{w^2}\big)\, e^{il\varphi}, \qquad p = 0, 1, 2, \dots,\; l \in \mathbb{Z} \tag{4.94}$$

where $C_{p,l}$ is a (complex) normalization constant and $v(\rho) = L_p^s(\rho)$. The beam width w is then expressed as follows:

$$w = \sqrt{\frac{2}{\gamma}} = \sqrt{\frac{2\sqrt{FL}}{k}}. \tag{4.95}$$

Laguerre-Gaussian beam described in Eq. (4.94) is independent in z

direction and remains constant during propagation in cavity. This beam propagates under the SVEA behind the resonator described in Eq. (4.70). Beam electric field envelope changes in z direction behind the cavity then [127]:

$$\begin{aligned}\mathcal{E}_p^l(r,\phi,z) = \mathcal{E}_0 \frac{w_0}{w(z)} \left(\frac{\sqrt{2}r}{w(z)}\right)^l L_p^l\left(\frac{2r^2}{w^2(z)}\right) \exp\left(-\frac{r^2}{w^2(z)}\right) \\ \times \exp\left[-ikz - ik\frac{r^2}{2R(z)} + il\phi + i(2p+l+1)\psi(z)\right],\end{aligned} \tag{4.96}$$

where the physical quantities $w(z),\ R(z),\ \zeta(z),\ \theta,\ z_R,\ k$ are described in Table 4.1.

Gaussian Beam

The Gaussian beam is the fundamental solution of Eq. (4.96) for $l = 0$ and $p = 0$, and plays a central role in practical laser applications. It serves as the established reference against which other laser beams are compared. The spatial envelope of the Gaussian beam electric field in cylindrical coordinates is given by [127]:

$$\mathcal{E}(r,z) = \mathcal{E}_0 \frac{w_0}{w(z)} \exp\left[-\frac{r^2}{w^2(z)}\right] \exp\left[i\left(kz + \frac{kr^2}{2R(z)} - \zeta(z)\right)\right]. \tag{4.97}$$

Both the amplitude term

$$\frac{w_0}{w(z)} \exp\left[-\frac{r^2}{w^2(z)}\right]$$

and the phase term

$$\exp\left[i\left(kz + \frac{kr^2}{2R(z)} - \zeta(z)\right)\right]$$

of the Gaussian beam are independent of the azimuthal angle ϕ. The corresponding intensity distribution is given by:

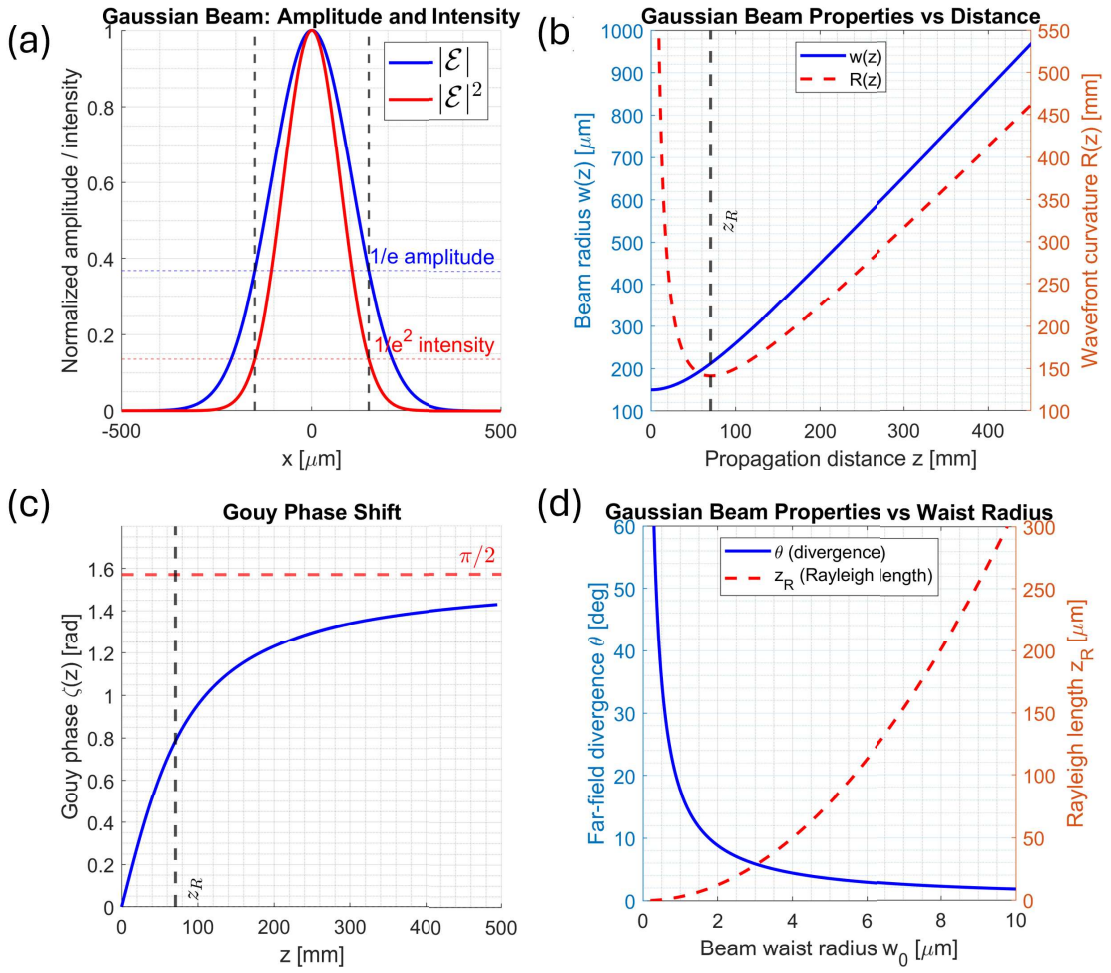


Figure 4.19: Gaussian beam amplitude and intensity profiles in the caustic region for a waist radius of $w_0 = 150\,\mu$m and wavelength $\lambda = 1\,\mu$m (a). The corresponding variations of the beam radius $w(z)$, wavefront curvature $R(z)$, and Gouy phase shift along propagation distance z are shown in panels (b) and (c). Panel (d) presents the Gaussian beam divergence θ and Rayleigh length z_R as functions of the waist radius w_0 at $\lambda = 1\,\mu$m.

$$|\mathcal{E}|^2 = \mathcal{E}_0^2 \frac{w_0^2}{w^2(z)} \exp\left[-\frac{2r^2}{w^2(z)}\right]. \tag{4.98}$$

The beam radius $w(z)$ is typically determined experimentally from the measured beam intensity distribution. By definition, $w(z)$ denotes the radius at which the intensity falls to $1/e^2$ of its maximum value, corresponding to a decrease of the field amplitude to $1/e$. Figure 4.19(a) shows the normalized Gaussian beam amplitude $|\mathcal{E}|$ and intensity $|\mathcal{E}|^2$ for a beam radius of $w(z) = 150\,\mu$m. As illustrated, the $1/e$ amplitude and

$1/e^2$ intensity levels intersect the same transverse location, confirming the consistency of the definition.

The beam radius $w(z)$ increases with distance from the waist, as shown in Fig. 4.19(b). Its evolution along the propagation axis can be divided into two regions relative to the Rayleigh range z_R. For $|z| < z_R$, the radius grows nonlinearly with z, whereas for $|z| \gg z_R$ it increases approximately linearly. This asymptotic behavior justifies the far-field divergence approximation given in Eq. 4.36.

The Gaussian wavefront curvature $R(z)$ is infinite at the waist, reaches its minimum at $z = z_R$, and increases asymptotically in the far field (red curve in Fig. 4.19(b)). The Gouy phase shift $\zeta(z)$ varies most rapidly near the waist and approaches its asymptotic limit in the far field (see Fig. 4.19(c)). As shown in Fig. 4.19(d), increasing the waist radius w_0 leads to a smaller far-field divergence θ and a larger Rayleigh range z_R.

We consider the monochromatic Gaussian beam with fixed frequency in time domain (ω) and fixed distribution of spatial spectrum $k_\perp = k_\perp(\theta)$. As the Gaussian beam is a solution of the SVEA, it has physical meaning and accurately represents reality only when its spatial spectral components remain within the angles of incidence (AOI) for which the SVEA deviation is not significant (see Fig. 4.15),which is $\approx$ below 20 deg. Gaussian beam spatial spectrum is unique, because it maintains the shape - Gaussian.

Estimation of the beam-quality factor M^2 outside the caustic

An analytical approach for evaluating the beam quality factor in two dimensions outside the waist was proposed by H. Yoda, P. Polynkin, and M. Mansuripur [149], formulated in Cartesian coordinates. In brief, the method involves calculating the first and second spatial moments in the Cartesian coordinate system (x, y):

$$\begin{aligned}\langle x\rangle &= \int\int x dx dy |A(x,y)|^2, \\ \langle y\rangle &= \int\int y dx dy |A(x,y)|^2,\end{aligned} \tag{4.99}$$

$$\begin{aligned}\sigma_x^2 &= \int\int dx dy \left(x - \langle x\rangle\right)^2 |A(x,y)|^2, \\ \sigma_y^2 &= \int\int dx dy \left(y - \langle y\rangle\right)^2 |A(x,y)|^2.\end{aligned} \tag{4.100}$$

Additionally, the auxiliary integrals $A_{x,y}$ and $B_{x,y}$ should be evaluated:

$$\begin{aligned}A_x &= \int\int dx dy \left(x - \langle x\rangle\right) \times \left[A(x,y)\frac{\partial A(x,y)*}{\partial x} - c.c.\right], \\ A_y &= \int\int dx dy \left(y - \langle y\rangle\right) \times \left[A(x,y)\frac{\partial A(x,y)*}{\partial y} - c.c.\right],\end{aligned} \tag{4.101}$$

$$\begin{aligned}B_x = \int\int dx dy \left|\frac{\partial A(x,y)}{\partial x}\right|^2 + \frac{1}{4}\times \\ \left(\int\int dx dy \left[A(x,y)\frac{\partial A(x,y)*}{\partial x} - c.c.\right]\right)^2, \\ B_y = \int\int dx dy \left|\frac{\partial A(x,y)}{\partial y}\right|^2 + \frac{1}{4}\times \\ \left(\int\int dx dy \left[A(x,y)\frac{\partial A(x,y)*}{\partial y} - c.c.\right]\right)^2.\end{aligned} \tag{4.102}$$

It should be noted that the complex conjugation applies only to the terms enclosed in square brackets. Finally, the quantities $A_{x,y}$, $B_{x,y}$, and $\sigma_{x,y}^2$ are substituted into the final expressions for M_x^2 and M_y^2, which are evaluated for a single coordinate x:

$$\begin{aligned}M_x^2 &= \sqrt{4B_x\sigma_x^2 + A_x^2}, \\ M_y^2 &= \sqrt{4B_y\sigma_y^2 + A_y^2}.\end{aligned} \tag{4.103}$$

The final beam quality factor is then:

$$M^2 = \sqrt{M_x^2 M_y^2}. \tag{4.104}$$

The beam quality factor M^2 expressions in Eqs. (4.103) and (4.104) are valid for beams propagating outside the waist plane. When applied at the waist, where the electric field is real, the calculation simplifies because the last term in the $B_{x,y}$ expressions (4.102) vanishes.

In our case, the electric field (see Eq. 4.46) is expressed in polar coordinates (ξ, ϕ), where the relations between the coordinate systems are given as:

$$\xi = \sqrt{x^2 + y^2}, \qquad \phi = \arctan\left(\frac{y}{x}\right). \tag{4.105}$$

For convenience, we denote the electric field as $A(\xi, \phi) = B(\xi)e^{il\phi}$, where $B(\xi)$ is a complex Bessel function of a generalized form that depends only on the radial coordinate ξ. The complex conjugate of the field is then given by:

$$A(\xi,\ \phi) = B(\xi)e^{il\phi}, \qquad A^*(\xi,\ \phi) = B^*(\xi)e^{-il\phi}. \tag{4.106}$$

Taking into account the relations given in Eq. 4.105, the field derivative can be expressed as:

$$\frac{\partial A}{\partial x} = \frac{\partial\Big(B\Big(\sqrt{x^2+y^2}\Big)\, e^{il\arctan(y/x)}\Big)}{\partial x} =$$
$$= \frac{\partial B}{\partial \xi}\,\frac{x}{\sqrt{x^2+y^2}}\, e^{il\phi} + B\,\frac{ily\, e^{il\arctan(y/x)}}{x^2(1+(y/x)^2)} = e^{il\phi}\left[\frac{\partial B}{\partial \xi}\cos\phi + B\,\frac{il\sin\phi}{\xi}\right]. \tag{4.107}$$

Taking into account the complex conjugation property $\left(\frac{\partial A}{\partial x}\right)^* = \frac{\partial A^*}{\partial x}$, the complex conjugate of the field derivative can be written as:

$$\left(\frac{\partial A}{\partial x}\right)^* = e^{-il\phi}\left[\frac{\partial B^*}{\partial \xi}\cos(\phi) - B^*\frac{il\sin(\phi)}{\xi}\right]. \tag{4.108}$$

Rewriting the integrands I_1 and I_2 in Eqs. 4.101 and 4.102 in terms of polar coordinates, we obtain:

$$I_1 = A(x,y)\frac{\partial A(x,y)^*}{\partial x} - A(x,y)^*\frac{\partial A(x,y)}{\partial x} = 2i\left(\cos\phi\left[-\Re\left(B(\xi)\right)\Im\left(\frac{\partial B(\xi)}{\partial \xi}\right) + \Re\left(\frac{\partial B(\xi)}{\partial \xi}\right)\Im\left(B(\xi)\right)\right] - |B(\xi)|^2\frac{l\sin\phi}{\xi}\right) \tag{4.109}$$

$$I_2 = \left|\frac{\partial A}{\partial x}\right|^2 = \frac{\partial A}{\partial x}\times\frac{\partial A^*}{\partial x} = \left[\frac{\partial B}{\partial \xi}\cos\left(\phi\right) + B\frac{il\sin\left(\phi\right)}{\xi}\right]\times\left[\frac{\partial B^*}{\partial \xi}\cos\left(\phi\right) - B^*\frac{il\sin\left(\phi\right)}{\xi}\right] = \frac{l^2|B|^2\sin^2\phi}{\xi^2} + \left|\frac{\partial B}{\partial \xi}\right|^2\cos^2\phi - \frac{2l\cos\phi\sin\phi}{\xi}\left(\Re\left(\frac{\partial B}{\partial \xi}\right)\Im\left(B\right) - \Re\left(B\right)\Im\left(\frac{\partial B}{\partial \xi}\right)\right). \tag{4.110}$$

The integrands I_1 and I_2, defined in Eqs. 4.109 and 4.110, are evaluated according to Eqs. 4.101 and 4.102 in the polar coordinate system:

$$\int_{-\infty}^{\infty} I_{1,2}\left(x,y\right)dxdy = \int_0^{2\pi}\int_0^{\infty} I_{1,2}(\xi,\phi)\;\xi\,d\xi\,d\phi. \tag{4.111}$$

The electric field $A(\xi,\phi)$, defined in Eq. 4.46, is expressed separately for the regions $\xi < 1$ and $\xi > 1$. Accordingly, the integral in Eq. 4.111 is divided into two parts, and the resulting A_x and B_x are given by:

$$A_x = \int_0^{2\pi}\int_0^{1}\xi^2\cos\phi I_1(\xi,\phi)\;\;d\xi\,d\phi + \int_0^{2\pi}\int_1^{\infty}\xi^2\cos\phi I_1(\xi,\phi)\;\;d\xi\,d\phi, \tag{4.112}$$

$$B_x = \int_0^{2\pi}\int_0^{1}\xi I_2(\xi,\phi)\;\;d\xi\,d\phi + \int_0^{2\pi}\int_1^{\infty}\xi I_2(\xi,\phi)\;\;d\xi\,d\phi + \frac{1}{4}\left(\int_0^{2\pi}\int_0^{1}\xi I_1(\xi,\phi)\;\;d\xi\,d\phi + \int_0^{2\pi}\int_1^{\infty}\xi I_1(\xi,\phi)\;\;d\xi\,d\phi\right)^2. \tag{4.113}$$

In our case, the electric field distribution exhibits radial symmetry (see Eq. 4.46); consequently, the integrals in the x and y directions are identical, i.e., $A_x = A_y$ and $B_x = B_y$.

The integrations in Eqs. 4.112 and 4.113 were performed numerically using the *Wolfram Mathematica* software package and its numerical integration function `NIntegrate` [205].

Bibliography

[1] J. J. Zayhowski and A. Mooradian, "Single-frequency microchip Nd lasers", *Optics Letters*, vol. 14, pp. 24–26, 1989.

[2] E. Molva, "Microchip lasers and their applications in optical microsystems", *Optical Materials*, vol. 11, no. 2-3, pp. 289–299, 1999.

[3] T. Robin, J. Cochard, and K. Moratis, "Laser sources: global market and trends", *Photonics Views*, vol. 21, pp. 1–81, 2024.

[4] M. Plukys, L. Grineviciute, J. Nikitina, D. Gailevicius, and K. Staliunas, "Enhancement of brightness in microchip laser with angular filtering mirrors", *Optics Laser Technology*, vol. 181, p. 111 904, 2025.

[5] M. Plukys, L. Grineviciute, J. Nikitina, D. Gailevičius, and K. Staliunas, "Polarization enhancement in Nd: YAG microchip laser with Meta-Mirror output coupler", *Optics Letters*, vol. 50, no. 15, pp. 4666–4669, 2025.

[6] M. Plukys, E. Gaizauskas, D. Gailevicius, and K. Staliunas, "Transverse modes and beam spatial quality in microchip lasers", *Phys. Rev. A*, vol. 107, p. 043 505, 2023.

[7] M. Levitt, "Laser market overview", in *The Laser Marketplace in 1989*, vol. 1124, SPIE, 1989, pp. 1–14.

[8] T. H. Maiman, "Stimulated Optical Radiation in Ruby", *Nature*, vol. 187, pp. 493–494, 1960.

[9] J. J. Zayhowski, "Microchip lasers", *Optical materials*, vol. 11, pp. 255–267, 1999.

[10] W. G. Wagner and B. A. Lengyel, "Evolution of the giant pulse in a laser", *Journal of Applied Physics*, vol. 34, no. 7, pp. 2040–2046, 1963.

[11] J. J. Zayhowski and C. D. III, "Diode-pumped passively Q-switched picosecond microchip lasers", *Optics letters*, vol. 19, pp. 1427–1429, 1994.

[12] D. A. Kleinman, A. Ashkin, and G. D. Boyd, "Second-Harmonic Generation of Light by Focused Laser Beams", *Phys. Rev.*, vol. 145, pp. 338–379, 1 May 1966.

[13] F. Pirzio, J. Rubens Negri, S. Pizzurro, E. Piccinini, and A. Agnesi, "Assessment of broad usability of a simple analytic model for passively Q-switched lasers with Cr: YAG saturable absorbers", *Journal of the Optical Society of America B*, vol. 37, no. 6, pp. 1659–1663, 2020.

[14] T. Sasaki, T. Kojima, A. Yokotani, O. Oguri, and S. Nakai, "Single-longitudinal-mode operation and second-harmonic generation of Nd: YVO_4 microchip lasers", *Optics letters*, vol. 16, no. 21, pp. 1665–1667, 1991.

[15] R. Conroy, "Microchip lasers", Ph.D. dissertation, University of St Andrews, 1998.

[16] W. Koechner, *Solid-State Laser Engineering*. Springer Science, 2006.

[17] J. Kratochvíl et al., "2 μm microchip laser based on Tm: YAG composite under 0.8 μm and 1.7 μm pumping", in *Solid State Lasers XXXI: Technology and Devices*, SPIE, vol. 11980, 2022, pp. 90–100.

[18] J. J. Zayhowski, "Passively Q-switched Nd: YAG microchip lasers and applications", *Journal of alloys and compounds*, vol. 303, pp. 393–400, 2000.

[19] J. Saikawa, S. Kurimura, I. Shoji, and T. Taira, "Tunable frequency-doubled Yb: YAG microchip lasers", *Optical Materials*, vol. 19, no. 1, pp. 169–174, 2002.

[20] G. Spühler et al., "A passively Q-switched microchip laser with high pulse energy and sub-nanosecond pulse duration", *Applied Physics B*, vol. 72, pp. 285–287, 2001.

[21] A. Steinmetz, D. Nodop, J. Limpert, R. Hohmuth, W. Richter, and A. Tünnermann, "2 MHz repetition rate, 200 ps pulse duration from a monolithic, passively Q-switched microchip laser", *Applied Physics B*, vol. 97, no. 2, pp. 317–320, 2009.

[22] T. Chen, X. Chen, C. Zhou, M. Li, and R. Shu, "Single-longitudinal-mode-operated, passively Q-switched Nd: YAG/Cr^{4+}: YAG microchip laser with$>$ 100 kHz repetition rate and$<$ 400 ps pulse width", *Applied Optics*, vol. 59, no. 13, pp. 4191–4197, 2020.

[23] R. Häring, R. Paschotta, R. Fluck, E. Gini, H. Melchior, and U. Keller, "Passively Q-switched microchip laser at 1.5 μ m", *Journal of the Optical Society of America B*, vol. 18, no. 12, pp. 1805–1812, 2001.

[24] S. Han et al., "Sub-nanosecond Nd: YAG/Cr^{4+}: YAG crystal laser operating at 0.9 μm", *Optics & Laser Technology*, vol. 181, p. 111 642, 2025.

[25] Y. Jiang, M. Nie, R. Guo, X. Fu, and Q. Liu, "Pushing the limit of pulse duration in Q-switched solid-state lasers with high gain", *Optics & Laser Technology*, vol. 129, p. 106 276, 2020.

[26] X. Guo, K. Hamamoto, S. Tokita, and J. Kawanaka, "160 ps Yb: YAG/Cr: YAG microchip laser", *Laser Physics Letters*, vol. 15, no. 10, p. 105 001, 2018.

[27] J. Nikkinen, V.-M. Korpijärvi, I. Leino, A. Härkönen, and M. Guina, "Microchip laser Q-switched with GaInNAs/GaAs SESAM emitting 204 ps pulses at 1342 nm", *Electronics Letters*, vol. 51, no. 11, pp. 850–852, 2015.

[28] E. Mehner, B. Bernard, H. Giessen, D. Kopf, and B. Braun, "Sub-20-ps pulses from a passively Q-switched microchip laser at 1 MHz repetition rate", *Opt. Lett.*, vol. 39, no. 10, pp. 2940–2943, May 2014.

[29] B. Braun, F. X. Kärtner, G. Zhang, M. Moser, and U. Keller, "56-ps passively Q-switched diode-pumped microchip laser", *Opt. Lett.*, vol. 22, no. 6, pp. 381–383, Mar. 1997.

[30] D. Nodop, J. Limpert, R. Hohmuth, W. Richter, M. Guina, and A. Tünnermann, "High-pulse-energy passively Q-switched quasi-monolithic microchip lasers operating in the sub-100-ps pulse regime", *Opt. Lett.*, vol. 32, no. 15, pp. 2115–2117, Aug. 2007.

[31] A. Giese et al., "Passively Q-switched sub-100 ps Yb^{3+}: YAG/Cr^{4+}: YAG microchip laser: experimental results and numerical analysis", in *Solid State Lasers XXXII: Technology and Devices*, SPIE, vol. 12399, 2023, pp. 187–197.

[32] J. J. Zayhowski and C. Dill, "Diode-pumped passively Q-switched picosecond microchip lasers", *Opt. Lett.*, vol. 19, no. 18, pp. 1427–1429, Sep. 1994.

[33] K. Nejezchleb, J. Šulc, H. Jelínková, and V. Škoda, "Microchip laser based on Yb:YAG/V:YAG monolith crystal", in *Solid State Lasers XXV: Technology and Devices*, W. A. Clarkson and R. K. Shori, Eds., International Society for Optics and Photonics, vol. 9726, SPIE, 2016, 97261H.

[34] H. H. Lim and T. Taira, ">50 MW peak power, high-brightness Nd:YAG/Cr^{4+}:YAG microchip laser with unstable resonator", *Opt. Express*, vol. 30, no. 4, pp. 5151–5158, Feb. 2022.

[35] K. Kadlec, J. Šulc, M. Němec, H. Jelínková, and K. Nejezchleb, "Pumping beam shaping for optimized performance of Q-Switched Nd:YAG/V:YAG microchip laser emitting at 1.44 μm", *Applied Physics B*, vol. 131, no. 3, p. 51, 2025, ISSN: 1432-0649.

[36] G. Spuhler et al., "Experimentally confirmed design guidelines for passively Q-switched microchip lasers using semiconductor saturable absorbers", *Journal of the Optical Society of America B*, vol. 16, pp. 376–388, 1999.

[37] J. J. Degnan, "Optimization of passively Q-switched lasers", *IEEE journal of quantum electronics*, vol. 31, no. 11, pp. 1890–1901, 1995.

[38] J. Zayhowski and P. Kelley, "Optimization of Q-switched lasers", *IEEE journal of quantum electronics*, vol. 27, no. 9, pp. 2220–2225, 2002.

[39] B. Cole, L. Goldberg, C. Ward Trussell, A. Hays, B. W. Schilling, and C. McIntosh, "Reduction of timing jitter in a Q-Switched Nd: YAG laser by direct bleaching of a Cr^{4+}: YAG saturable absorber", *Optics express*, vol. 17, no. 3, pp. 1766–1771, 2009.

[40] J. B. Khurgin, F. Jin, G. Solyar, C.-C. Wang, and S. Trivedi, "Cost-effective low timing jitter passively Q-switched diode-pumped solid-state laser with composite pumping pulses", *Appl. Opt.*, vol. 41, no. 6, pp. 1095–1097, 2002.

[41] S. Wang, Y.-b. Wang, G. Feng, and S.-h. Zhou, "A low timing jitter picosecond microchip laser pumped by pulsed LD", *Optics Communications*, vol. 371, pp. 72–75, 2016.

[42] T.-L. Huang, H.-C. Liang, K.-W. Su, and Y.-F. Chen, "Exploring the emergence of the self-Q-switching in diode-pumped Yb: KGW monolithic lasers", *IEEE Journal of Selected Topics in Quantum Electronics*, vol. 24, no. 5, pp. 1–6, 2018.

[43] R. Conroy, T. Lake, G. Friel, A. Kemp, and B. Sinclair, "Self-Q-switched Nd: YVO_4 microchip lasers", *Optics letters*, vol. 23, no. 6, pp. 457–459, 1998.

[44] B. Zhang et al., "Compact self-Q-switched Tm: YLF laser at 1.91 μm", *Optics & Laser Technology*, vol. 100, pp. 103–108, 2018.

[45] P. Kang, S. Zhang, X. Zhang, and J. Huang, "High power self-Q-switched Tm: YAP solid state laser based on the ground state reabsorption", *Infrared Physics & Technology*, vol. 123, p. 104 117, 2022.

[46] Y. Chen, J. Huang, Y. Lin, X. Gong, Z. Luo, and Y. Huang, "Eye-safe 1.55 μm high-repetition-frequency self-Q-switched Er:

Yb: Lu2Si2O7 pulse laser", *Optics & Laser Technology*, vol. 133, p. 106 554, 2021.

[47] J. Šulc, K. Kadlec, H. Jelínková, K. Nejezchleb, and L. Beran, "Output peak-power optimization of Nd:YAG/Cr:YAG microchip laser", in *High-power, High-energy Lasers, and Ultrafast Optical Technologies II*, P. Bakule, P. Baer, J. Hein, and T. J. Butcher, Eds., International Society for Optics and Photonics, vol. 13532, SPIE, 2025, p. 135320I.

[48] F. M. Prado, T. J. Franco, and N. U. Wetter, "Sub-nanosecond, 41 mJ pulse energy, passively Q-switched Nd:YLF laser", *Optics & Laser Technology*, vol. 162, p. 109 257, 2023.

[49] J. Šulc, J. Eisenschreiber, H. Jelínková, K. Nejezchleb, and V. Škoda, "Yb:YAG/Cr:YAG microchip laser output energy optimization", in *High-Power, High-Energy, and High-Intensity Laser Technology IV*, J. Hein and T. J. Butcher, Eds., International Society for Optics and Photonics, vol. 11033, SPIE, 2019, p. 1 103 310.

[50] J. Šulc, H. Jelínková, K. Nejezchleb, and V. Škoda, "Generation of 1.6 ns Q-switched pulses based on Yb:YAG/Cr:YAG microchip laser", in *High-Power, High-Energy, and High-Intensity Laser Technology II*, J. Hein, Ed., International Society for Optics and Photonics, vol. 9513, SPIE, 2015, p. 951 317.

[51] J. Dong, A. Shirakawa, K.-i. Ueda, H. Yagi, T. Yanagitani, and A. A. Kaminskii, "Efficient $Yb^{3+} : Y_3Al_5O_{12}$ ceramic microchip lasers", *Applied Physics Letters*, vol. 89, no. 9, p. 091 114, 2006.

[52] C. McIntosh, A. Hays, S. R. Chinn, L. Goldberg, and J. Leach, "High average power passively Q-switched Yb: YAG micro-laser", in *Solid State Lasers XXIX: Technology and Devices*, SPIE, vol. 11259, 2020, pp. 169–175.

[53] H. Maestre, M. Cuenca, and A. E. Ortega, "Tunability of a microchip Yb: KGW solid-state laser self-injected with different wavelength-selective external cavities", *Applied Physics B*, vol. 131, no. 3, pp. 1–9, 2025.

[54] M. Fibrich, H. Jelínková, J. Šulc, K. Nejezchleb, and V. Škoda, "Pr:$YAlO_3$ microchip laser", *Opt. Lett.*, vol. 35, no. 15, pp. 2556–2557, 2010.

[55] M. Gaponenko, N. Kuleshov, and T. Südmeyer, "Passively Q-Switched Thulium Microchip Laser", *IEEE Photonics Technology Letters*, vol. 28, no. 2, pp. 147–150, 2015.

[56] J. Šulc, H. Jelínková, K. Nejezchleb, and V. Škoda, "High-efficient room-temperature CW operating Tm:YAP laser with microchip resonator", in *Solid State Lasers XVIII: Technology and Devices*, W. A. Clarkson, N. Hodgson, and R. K. Shori, Eds., International Society for Optics and Photonics, vol. 7193, SPIE, 2009, 71932H.

[57] J. Kratochvíl, J. Šulc, H. Jelínková, K. Nejezchleb, and J. Polák, "Tm: YAP microchip laser under 1700 nm and 790 nm diode pumping", in *Solid State Lasers XXX: Technology and Devices*, SPIE, vol. 11664, 2021, pp. 116–127.

[58] J. Kratochvíl et al., "2 μm microchip laser based on Tm: YAG composite under 0.8 μm and 1.7 μm pumping", in *Solid State Lasers XXXI: Technology and Devices*, SPIE, vol. 11980, 2022, pp. 90–100.

[59] A. E. Siegman, *Lasers*. University Science Books, 1986.

[60] E. Kanchanavaleerat et al., "Crystal growth of high doped Nd: YAG", *Optical Materials*, vol. 26, no. 4, pp. 337–341, 2004.

[61] J.-f. Lu et al., "Optical properties and highly efficient laser oscillation of Nd: YAG ceramics", *Applied Physics B*, vol. 71, no. 4, pp. 469–473, 2000.

[62] G. Kumar et al., "Spectroscopic and stimulated emission Characteristics of Nd^{3+}in transparent YAG ceramics", *IEEE journal of quantum electronics*, vol. 40, no. 6, pp. 747–758, 2004.

[63] O. Puncken, L. Winkelmann, M. Frede, P. Weßels, J. Neumann, and D. Kracht, "Heat generation in Nd: YAG at different doping levels", *Applied Optics*, vol. 51, no. 31, pp. 7586–7590, 2012.

[64] J. J. Zayhowski, "Q-switched operation of microchip lasers", *Opt. Lett.*, vol. 16, no. 8, pp. 575–577, Apr. 1991.

[65] T. Taira, A. Mukai, Y. Nozawa, and T. Kobayashi, "Single-mode oscillation of laser-diode-pumped Nd:YVO4 microchip lasers", *Opt. Lett.*, vol. 16, no. 24, pp. 1955–1957, Dec. 1991.

[66] J. J. Zayhowski, "Pulsed Operation of Microchip Lasers", in *Advanced Solid State Lasers*, Optica Publishing Group, 1991, p. DL7.

[67] J. J. Zayhowski and A. Mooradian, "Frequency-modulated Nd:YAG microchip lasers", *Opt. Lett.*, vol. 14, no. 12, pp. 618–620, Jun. 1989.

[68] P. Laporta, S. Taccheo, S. Longhi, O. Svelto, and G. Sacchi, "Diode-pumped microchip Er–Yb:glass laser", *Opt. Lett.*, vol. 18, no. 15, pp. 1232–1234, Aug. 1993.

[69] H. H. Lim and T. Taira, ">50 MW peak power, high brightness Nd:YAG/Cr^{4+}:YAG microchip laser with unstable resonator", *Optics Express*, vol. 30, pp. 5151–5158, 2022.

[70] H. H. Lim and T. Taira, ">High peak power Nd:YAG/Cr:YAG ceramic microchip laser with unstable resonator", *Optics Express*, vol. 27, pp. 31 307–31 315, 2019.

[71] M. Tsunekane and T. Taira, "300 W continuous-wave operation of a diode edge-pumped, hybrid composite Yb:YAG microchip laser", *Optics letters*, vol. 31, pp. 2003–2005, 2006.

[72] M. Tsunekane and T. Taira, "High-power operation of diode edge-pumped, composite all-ceramic Yb : $Y_3Al_5O_{12}$ microchip laser", *Applied Physics Letters*, vol. 90, pp. 1–3, 2007.

[73] S. C. Tidwell, J. F. Seamans, M. S. Bowers, and A. K. Cousins, "Scaling CW diode-end-pumped Nd: YAG lasers to high average powers", *IEEE Journal of Quantum Electronics*, vol. 28, no. 4, pp. 997–1009, 1992.

[74] D.-L. Kim and B.-T. Kim, "Crack formation process in ceramic Nd: YAG", *OSA Continuum*, vol. 3, no. 6, pp. 1633–1637, 2020.

[75] L. Cini and J. I. Mackenzie, "Analytical thermal model for end-pumped solid-state lasers", *Applied Physics B*, vol. 123, no. 273, 2017.

[76] D.-L. Kim and B.-T. Kim, "Fracture characteristics of ceramic Nd: YAG", *Optics Express*, vol. 22, no. 9, pp. 11 331–11 339, 2014.

[77] G. XIAOYANG and K. JUNJI, "High beam quality and high peak power Yb:YAG/Cr:YAG microchip laser", *Optics Express*, vol. 27, pp. 45–54, 2019.

[78] L. Rosenkrantz, "GaAs diode-pumped Nd: YAG laser", *Journal of Applied Physics*, vol. 43, no. 11, pp. 4603–4605, 1972.

[79] U. Keller et al., "Semiconductor saturable absorber mirrors (SESAM's) for femtosecond to nanosecond pulse generation in solid-state lasers", *IEEE Journal of selected topics in Quantum Electronics*, vol. 2, no. 3, pp. 435–453, 1996.

[80] R. Fluck, R. Häring, R. Paschotta, E. Gini, H. Melchior, and U. Keller, "Eyesafe pulsed microchip laser using semiconductor saturable absorber mirrors", *Applied physics letters*, vol. 72, no. 25, pp. 3273–3275, 1998.

[81] M. Haiml, R. Grange, and U. Keller, "Optical characterization of semiconductor saturable absorbers", *Applied Physics B*, vol. 79, no. 3, pp. 331–339, 2004.

[82] A. Yasukevich et al., "Modelling of graphene Q-switched Tm lasers", *Optics Communications*, vol. 389, pp. 15–22, 2017.

[83] J. M. Serres et al., "Graphene Q-switched compact Yb: YAG laser", *IEEE Photonics Journal*, vol. 7, no. 5, pp. 1–7, 2015.

[84] M. Fibrich, H. Jelínková, J. Šulc, K. Nejezchleb, and V. Škoda, "Pr: $YAlO_3$ microchip laser at 662 nm", *Laser Physics Letters*, vol. 8, no. 2, pp. 116–119, 2011.

[85] F. Song et al., "Determination of the thermal loading in laser-diode-pumped erbium-ytterbium-codoped phosphate glass microchip laser", *Journal of the Optical Society of America B*, vol. 24, no. 9, pp. 2327–2332, 2007.

[86] S. Liu et al., "Effect of thermal lens on beam quality and mode matching in LD pumped Er–Yb-codoped phosphate glass microchip laser", *Journal of Physics D: Applied Physics*, vol. 41, no. 3, p. 035 104, 2008.

[87] J. A. Hutchinson and T. H. Allik, "Diode array-pumped Er, Yb: Phosphate glass laser", *Applied physics letters*, vol. 60, no. 12, pp. 1424–1426, 1992.

[88] D. Jiang et al., "A Co^{2+}-doped alumina-rich $Mg_{0.4}Al_{2.4}O_4$ spinel crystal as saturable absorber for a LD pumped Er: glass microchip laser at 1535 nm", *Laser Physics Letters*, vol. 8, no. 5, p. 343, 2011.

[89] P. Seidl, J. Koelbl, B. Schloder, and J. Ebbecke, "Development of a passively Q-switched eye-safe microchip laser for pulsed laser range-finding", in *Fiber Lasers and Glass Photonics: Materials through Applications IV*, SPIE, vol. 13003, 2024, p. 1 300 302.

[90] J. Serres et al., "Q-switching of a Tm, Ho: $KLu(WO_4)_2$ microchip laser by a graphene-based saturable absorber", *Laser Physics Letters*, vol. 13, no. 2, p. 025 801, 2015.

[91] H. Chen, W. Yao, H. Uehara, and R. Yasuhara, "Graphene Q-switched Tb: $LiYF_4$ green laser", *Optics Letters*, vol. 45, no. 9, pp. 2596–2599, 2020.

[92] P. Wang, S.-H. Zhou, K. Lee, and Y. Chen, "Picosecond laser pulse generation in a monolithic self-Q-switched solid-state laser", *Optics Communications*, vol. 114, no. 5-6, pp. 439–441, 1995.

[93] Y. Cheng, J. Dong, and Y. Ren, "Enhanced performance of Cr, Yb: YAG microchip laser by bonding Yb: YAG crystal", *Optics Express*, vol. 20, no. 22, pp. 24 803–24 812, 2012.

[94] J. Dong, K. Ueda, and A. Kaminski, "Laser-diode pumped self-Q-switched microchip lasers", *Optical Review*, vol. 15, pp. 57–74, 2008.

[95] K. Zhu, H. Chen, S. Zhang, Z. Shi, Y. Wang, and Y. Tan, "Frequency-Shifted Optical Feedback Measurement Technologies

Using a Solid-State Microchip Laser", *Applied Sciences*, vol. 9, no. 1, 2019, ISSN: 2076-3417.

[96] E. Lacot and O. Hugon, "Frequency-shifted optical feedback in a pumping laser diode dynamically amplified by a microchip laser", *Appl. Opt.*, vol. 43, no. 25, pp. 4915–4921, Sep. 2004.

[97] Y. Tan, S. Zhang, S. Zhang, Y. Zhang, and N. Liu, "Response of microchip solid-state laser to external frequency-shifted feedback and its applications", *Scientific reports*, vol. 3, no. 1, p. 2912, 2013.

[98] H. Chen and S. Zhang, "Microchip Nd: YAG dual-frequency laser interferometer for displacement measurement", *Optics Express*, vol. 29, no. 4, pp. 6248–6256, 2021.

[99] S. Zhang, "Precision Measurement Instrument with Microchip Solid Dual-Frequency Lasers", in *Advances in Laser Performance and New Principles of Precision Measuring Instruments*, Springer, 2025, pp. 193–305.

[100] U. N. Singh et al., "Diode-pumped 2-um solid state lidar transmitter for wind measurements", in *Lidar Atmospheric Monitoring*, SPIE, vol. 3104, 1997, pp. 173–178.

[101] M. Nägele, K. Stoppel, and T. Dekorsy, "Passively Q-switched 914 nm microchip laser for lidar systems", *Optics Express*, vol. 29, no. 15, pp. 23 799–23 809, 2021.

[102] E. Kolmakov, D. Redka, A. Grishkanich, I. Kudashev, and K. Tsvetkov, "Solid-state microchip based scanning laser 3D system", in *Laser 3D Manufacturing V*, SPIE, vol. 10523, 2018, pp. 185–195.

[103] N.-T. Vasile and N. Pavel, "Multi-point laser-induced ignition of air-methane mixtures by a high peak-power passively Q-switched Nd:YAG/Cr^{4+}:YAG laser", *Optics Laser Technology*, vol. 141, p. 107 169, 2021.

[104] I. Gornushkin, K. Amponsah-Manager, B. Smith, N. Omenetto, and J. Winefordner, "Microchip Laser-Induced Breakdown Spec-

troscopy: A Preliminary Feasibility Investigation", *Appl. Spectrosc.*, vol. 58, no. 7, pp. 762–769, Jul. 2004.

[105] A. Freedman, F. J. Iannarilli, and J. C. Wormhoudt, "Aluminum alloy analysis using microchip-laser induced breakdown spectroscopy", *Spectrochimica Acta Part B: Atomic Spectroscopy*, vol. 60, no. 7, pp. 1076–1082, 2005, Laser Induced Plasma Spectroscopy and Applications (LIBS 2004) Third International Conference, ISSN: 0584-8547.

[106] M. Neuland et al., "Quantitative measurement of the chemical composition of geological standards with a miniature laser ablation/ionization mass spectrometer designed for in situ application in space research", *Measurement Science and Technology*, vol. 27, no. 3, p. 035 904, 2016.

[107] J. Blacksberg, E. Alerstam, C. J. Cochrane, Y. Maruyama, and J. D. Farmer, "Miniature high-speed, low-pulse-energy picosecond Raman spectrometer for identification of minerals and organics in planetary science", *Applied Optics*, vol. 59, no. 2, pp. 433–444, 2020.

[108] M. Tsunekane, T. Inohara, A. Ando, N. Kido, K. Kanehara, and T. Taira, "High Peak Power, Passively -switched Microlaser for Ignition of Engine", *Journal of quantum electronics*, vol. 46, pp. 277–284, 2010.

[109] R. Bhandari, N. Tsuji, T. Suzuki, M. Nishifuji, and T. Taira, "Efficient second to ninth harmonic generation using megawatt peak power microchip laser", *Optics Express*, vol. 21, no. 23, pp. 28 849–28 855, 2013.

[110] J. J. Zayhowski, "Microchip optical parametric oscillators", *IEEE Photonics Technology Letters*, vol. 9, no. 7, pp. 925–927, 2002.

[111] J. Banys, S. Armalytė, J. Pimpė, O. Balachninaitė, V. Jarutis, and J. Vengelis, "Subnanosecond microlaser pumped fan-out grating design MgO: PPLN optical parametric generator continuously

tunable from near-to mid-infrared", *Optics & Laser Technology*, vol. 171, p. 110 433, 2024.

[112] A. Demidovich et al., "Sub-nanosecond microchip laser with intracavity Raman conversion", *Applied Physics B*, vol. 76, no. 5, pp. 509–514, 2003.

[113] J. M. Stone and J. C. Knight, "Visibly "white" light generation in uniform photonic crystal fiber using a microchip laser", *Optics express*, vol. 16, no. 4, pp. 2670–2675, 2008.

[114] N. Omenetto, B. Smith, I. Gornushkin, J. Winefordner, et al., "Microchip laser ablation of metals: investigation of the ablation process in view of its application to laser-induced breakdown spectroscopy", *Journal of Analytical Atomic Spectrometry*, vol. 20, no. 6, pp. 544–551, 2005.

[115] T. Kato, Y. Sakino, and Y. Sano, "Effect of laser peening with a microchip laser on fatigue life in butt-welded high-strength steel", *Applied Mechanics*, vol. 2, no. 4, pp. 878–890, 2021.

[116] J. Yuan, J. Chen, F. Liu, and C. Huang, "Investigation on Microwelding of Microchip by Laser without Solder", *Materials Transactions*, vol. 54, no. 6, pp. 922–925, 2013.

[117] A. Ancona, D. Nodop, J. Limpert, S. Nolte, and A. Tünnermann, "Microdrilling of metals with an inexpensive and compact ultrashort-pulse fiber amplified microchip laser", *Applied Physics A*, vol. 94, no. 1, pp. 19–24, 2009.

[118] M. Rajan et al., "A new method of marking dentures using microchips", *The Journal of Forensic Odonto-Stomatology-JFOS*, vol. 20, no. 1, pp. 1–5, 2002.

[119] C. Hönninger et al., "Ultrafast ytterbium-doped bulk lasers and laser amplifiers", *Applied Physics B*, vol. 69, no. 1, pp. 3–17, 1999.

[120] X. Délen, F. Balembois, and P. Georges, "Design of a high gain single stage and single pass Nd: YVO_4 passive picosecond amplifier", *Journal of the Optical Society of America B*, vol. 29, no. 9, pp. 2339–2346, 2012.

[121] E. Türkyilmaz et al., "Simple ps microchip Nd: YVO_4 laser with 3.3-ps pulses at 0.2 to 1.4 MHz and single-stage amplification to the microjoule level", *Optical Engineering*, vol. 55, no. 6, pp. 066 126–066 126, 2016.

[122] C. Wang, C. Liu, L. Shen, Z. Zhao, B. Liu, and H. Jiang, "1.6 MW peak power, 90 ps all-solid-state laser from an aberration self-compensated double-passing end-pumped Nd: YVO_4 rod amplifier", *Applied Optics*, vol. 55, no. 9, pp. 2399–2403, 2016.

[123] V. Koval, R. Balmashnov, V. Pokrovskiy, E. Viktorov, and A. Kornev, "10 W-level sub-100 ps 1 MHz MOPA laser with a microchip master oscillator", *Applied Optics*, vol. 60, no. 30, pp. 9342–9346, 2021.

[124] R. Lehneis, A. Steinmetz, J. Limpert, and A. Tünnermann, "All-fiber pulse shortening of passively Q-switched microchip laser pulses down to sub-200 fs", *Optics letters*, vol. 39, no. 20, pp. 5806–5809, 2014.

[125] H. Kohl, G. Kulcsar, D. Kopf, and B. Braun, "12-ps megawatt peak power pulses out of a single laser oscillator with nonlinear pulse compression", in *Solid State Lasers XXVIII: Technology and Devices*, SPIE, vol. 10896, 2019, pp. 80–86.

[126] R. Diao, Z. Liu, F. Niu, A. Wang, T. Taira, and Z. Zhang, "Compressed 6 ps pulse in nonlinear amplification of a Q-switched microchip laser", *Laser Physics*, vol. 27, no. 2, p. 025 102, 2016.

[127] H. Kogelnik and T. Li, "Laser Beams and Resonators", *Appl. Opt.*, vol. 5, pp. 1550–1567, 1966.

[128] A. G. Fox and T. Li, "Resonant modes in a maser interferometer", *Bell System Technical Journal*, vol. 40, no. 2, pp. 453–488, 1961.

[129] A. E. Siegman, "Laser beams and resonators: beyond the 1960s", *IEEE Journal of selected topics in quantum electronics*, vol. 6, no. 6, pp. 1389–1399, 2002.

[130] L. Casperson and A. Yariv, "The Gaussian mode in optical resonators with a radial gain profile", *Applied Physics Letters*, vol. 12, no. 10, pp. 355–357, 1968.

[131] A. E. Siegman, "Hermite–gaussian functions of complex argument as optical-beam eigenfunctions", *J. Opt. Soc. Am.*, vol. 63, pp. 1093–1094, 1973.

[132] G. K. Harkness and W. J. Firth, "Transverse Modes of Microchip Solid State Lasers", *Journal of Modern Optics*, vol. 39, pp. 2023–2037, 1992.

[133] S. Longhi, "Theory of transverse modes in end-pumped microchip lasers", *J. Opt. Soc. Am.*, vol. 11, pp. 2716–718, 1994.

[134] S. Longhi and P. Laporta, "Longitudinal–transverse mode interplay and conical emission in microchip lasers", *J. Opt. Soc. Am.*, vol. 12, pp. 1511–1515, 1995.

[135] F. Sanchez and A. Chardon, "Transverse modes in microchip lasers", *J. Opt. Soc. Am. B*, vol. 13, pp. 2869–2871, 1996.

[136] F. Sanchez and A. Chardon, "Pump size optimization in microchip lasers", *Optics Communications*, vol. 136, pp. 405–409, 1997.

[137] C. Serrat, M. P. van Exter, N. J. van Druten, and J. P. Woerdman, "Transverse mode formation in microlasers by combined gain- and index-guiding", *IEEE Journal of Quantum Electronics*, vol. 35, pp. 1314–1321, 1999.

[138] N. J. van Druten, "Observation of transverse modes in a microchip laser with combined gain and index guiding", *J. Opt. Soc. Am. B*, vol. 13, pp. 2869–2871, 2001.

[139] M. Achtenhagen, A. A. Hardy, and E. Kapon, "Threshold Analysis of Vertical-Cavity Surface-Emitting Lasers With Intracavity Contacts", *IEEE Journal of Quantum Electronics*, vol. 42, pp. 891–897, 2006.

[140] O. Conradi, S. Helfert, and R. Pregla, "Comprehensive Modeling of Vertical-Cavity Laser-Diodes by the Method of Lines", *IEEE Journal of Quantum Electronics*, vol. 37, pp. 928–935, 2001.

[141] G. R. Hadley, M. E. Warren, K. D. Choquette, J. W. Scott, and S. W. Corzine, "Comprehensive Numerical Modeling of Vertical-Cavity Surface-Emitting Lasers", *IEEE Journal of Quantum Electronics*, vol. 32, no. 4, 1996.

[142] K. Staliunas and V. J. Sanchez-Morcillo, *Transverse Patterns in Nonlinear Optical Resonators*. Springer, 2002.

[143] H. Haken, *Laser Light Dynamics, Volume 2*. North-Holland Physics Publishing, 1985.

[144] L. A. Lugiato, F. Prati, and M. Brambilla, *Nonlinear Optical Systems*. Cambridge University Press, 2015.

[145] A. Bassi, F. Prati, and L. A. Lugiato, "Optical instabilities in Fabry-Perot resonators", *Physical review A*, vol. 103, no. 053519, 2021.

[146] F. Prati et al., "Global and localised temporal structures in driven ring quantum cascade lasers", *Chaos, Solitons and Fractals*, vol. 153, no. 11, 2021.

[147] A. E. Siegman, "New developments in laser resonators", in *Optical Resonators*, vol. 1224, SPIE, 1990.

[148] T. Sean Ross, *Laser beam quality metrics*. SPIE Press, 2013.

[149] H. Yoda, P. Polynkin, and M. Mansuripur, "Beam Quality Factor of Higher Order Modes in a Step-Index Fiber", *Journal of Lightwave Technology*, vol. 24, pp. 1350–1355, 2006.

[150] P.-A. Belanger, "Beam quality factor of the LP_{01} mode of the step-index fiber", *Optical Engineering*, vol. 32, no. 9, pp. 2107–2109, 1993.

[151] A. E. Siegman, "Defining the effective radius of curvature for a nonideal optical beam", *IEEE Journal of Quantum Electronics*, vol. 27, no. 5, pp. 1146–1148, 2002.

[152] M. Tsunekane and T. Taira, "High Peak Power, Passively Q-Switched Yb:YAG/Cr:YAG Micro-Lasers", *Journal of Quantum electronics*, vol. 49, pp. 454–461, 2013.

[153] J.-F. Bisson, O. Parriaux, J.-C. Pommier, S. Tonchev, and K. Ueda, "A polarization-stabilized microchip laser using a resonant grating mirror", *Applied Physics B*, vol. 85, no. 4, pp. 519–524, 2006.

[154] M. Fibrich, J. Sulc, and H. Jelinkova, "Alexandrite microchip lasers", *Optics Express*, vol. 27, No.12, 2019.

[155] R. Zhou, E. Li, H. Li, P. Wang, and J. Yao, "Continuous-wave, 15.2 W diode-end-pumped Nd:YAG laser operating at 946 nm", *Optics letterss*, vol. 31, pp. 1869–1871, 2006.

[156] Y. T. Chang, Y. P. Huang, K. W. Su, and Y. F. Chen, "Comparison of thermal lensing effects between single-end and double-end diffusion-bonded Nd : YVO_4 crystals for $^4F_{3/2} \rightarrow ^4 I_{11/2}$ and $^4F_{3/2} \rightarrow ^4 I_{13/2}$ transitions", *Optics Express*, vol. 16, p. 21 155, 2008.

[157] R. Wilhelm, M. Frede, and D. Kracht, "Power Scaling of End-Pumped Solid-State Rod Lasers by Longitudinal Dopant Concentration Gradients", *IEEE Journal of quantum electronics*, vol. 44, pp. 232–244, 2008.

[158] X. Guo, S. Tokita, and J. Kawanaka, "High beam quality and high peak power Yb:YAG/Cr:YAG microchip laser", *Optics Express*, vol. 27, pp. 45–54, 2019.

[159] D. Gailevicius, V. Koliadenko, V. Purlys, M. Peckus, V. Taranenko, and K. Staliunas, "Photonic Crystal Microchip Laser", *Scientific Reports*, vol. 6, p. 34 173, 2016.

[160] S. Takimoto, T. Tachikawa, R. Shogenji, and J. Ohtsubo, "Control of spatio-temporal dynamics of broad-area semiconductor lasers by strong optical injection", *IEEE Photonics Technology Letters*, vol. 21, pp. 1051–1053, 2009.

[161] S. Mandre, I. Fischer, and W. Elsässer, "Control of the spatiotemporal emission of a broad-area semiconductor laser by spatially filtered feedback", *Optics letters*, vol. 28, pp. 1135–1137, 2003.

[162] J. Martín-Regalado, G. H. M. van Tartwijk, S. Balle, and S. M. M., "Mode control and pattern stabilization in broad-area lasers by optical feedback", *Phys. Rev. A*, vol. 54, p. 5386, 1996.

[163] J. Li, K. Ueda, L. Zhong, M. Musha, A. Shirakawa, and T. Sato, "Efficient excitations of radially and azimuthally polarized Nd^{3+}:YAG ceramic microchip laser by use of subwavelength multilayer concentric gratings composed of Nb_2O_5/SiO_2", *Optics express*, vol. 16, pp. 10 841–10 848, 2008.

[164] J. Saikawa, S. Kurimura, I. Shoji, and T. Taira, "Tunable frequency-doubled Yb: YAG microchip lasers", *Optical Materials*, vol. 19, pp. 169–174, 2002.

[165] K. Staliunas and V. J. Sánchez-Morcillo, "Spatial filtering of light by chirped photonic crystals", *Physical Review A*, vol. 79, p. 053 807, 2009.

[166] L. Maigyte et al., "Signatures of light-beam spatial filtering in a three-dimensional photonic crystal", *Physical Review A*, vol. 82, p. 043 819, 2010.

[167] L. Maigyte and K. Staliunas, "Spatial filtering with photonic crystals", *Applied physics reviews*, vol. 2, p. 1, 2015.

[168] Q. Qian, S. Ti, and C. Wang, "All-dielectric ultra-thin metasurface angular filter", *Optics letters*, vol. 44, pp. 3984–3987, 2019.

[169] J.-F. Bisson, N. Lyndin, K.-i. Ueda, and O. Parriaux, "Enhancement of the Mode Area and Modal Discrimination of Microchip Lasers Using Angularly Selective Mirrors", *IEEE Journal of quantum electronics*, vol. 44, pp. 628–637, 2008.

[170] N. Lyndin, T. Kämpfe, S. Tonchev, S. Reynaud, and O. Parriaux, "Transverse-mode selective resonant grating-mirrors for high power and high brightness emission", *Optics Express*, vol. 23, pp. 17 275–17 289, 2015.

[171] H. Wang, R. Herrero, M. Botey, Y. Cheng, and K. Staliunas, "Translationally invariant metamirrors for spatial filtering of light beams", *Phys. Rev. A*, vol. 102, p. 013 517, 2020.

[172] R. Lymarenko et al., "Super-collimation by axisymmetric diffractive metamirror", *Optics Letters*, vol. 46, pp. 3845–3848, 2021.

[173] L. Grineviciute, J. Nikitina, C. Babayigit, and K. Staliunas, "Fano-like resonances in nanostructured thin films for spatial filtering", *Applied Physics Letters*, vol. 118, no. 13, p. 131 114, Mar. 2021, ISSN: 0003-6951.

[174] G. Bouwmans, B. Segard, P. Glorieux, P. Khandokhin, N. Milovsky, and E. Y. Shirokov, "Polarization Dynamics of Longitudinally Monomode Bipolarized Microchip Solid-State Lasers", *Radiophysics and Quantum Electronics*, vol. 47, pp. 10–11, 2004.

[175] I. Ievlev, P. Khandokhin, and E. Shirokov, "Polarisation dynamics of single-longitudinal-mode Nd:YAG lasers with a weakly anisotropic cavity", *Quantum Electronics*, vol. 36, pp. 228–231, 2006.

[176] G. Verschaffelt, G. Sande, and J. Danckaert, "Delayed polarization dynamics in Nd^{3+}-doped yttrium-aluminum-garnet lasers", *Physical Review A*, vol. 77, p. 063 801, 2008.

[177] J. Dong, A. Shirakawa, and K.-i. Ueda, "A crystalline-orientation self-selected linearly polarized $Yb : Y_3Al_5O_{12}$ microchip laser", *Applied Physics Letters*, vol. 93, p. 101 105, 2008.

[178] J. Dong, J. Ma, and Y. Ren, "Polarization Manipulated Solid State Lasers with Crystalline Orientations", *Laser Physics*, vol. 21, pp. 2053–2058, 2011.

[179] H. Chen, S. Zhang, and Y. Tan, "Effect of pump polarization direction on power characteristics in monolithic microchip Nd:YAG dual-frequency laser", *Applied Optics*, vol. 55, pp. 2858–2862, 2016.

[180] N. Milovskii and P. Khandokhin, "Simulation of gain anisotropy induced by linearly polarised pump radiation in a bipolar Nd : YAG laser", *Quantum Electronics*, vol. 49, pp. 497–504, 2019.

[181] H. Akagla, N. Chapron, G. Loas, M. Vallet, and M. Brunel, "Control of the bipolarization emission of an Yb:YAG laser by

the orientation of the pump polarization", *Optics Letters*, vol. 78, pp. 700–703, 2023.

[182] F. Pigeon et al., "Microchip-laser polarization control by destructive-interference resonant-grating mirror", *Optics Express*, vol. 15, pp. 2573–2584, 2007.

[183] O. Parriaux et al., "Polarization control of a Yb:YAG ceramic microchip laserby constructive-interference resonant grating mirror", *Journal of Modern Optics*, vol. 55, pp. 1899–1912, 2008.

[184] A. Doucet, G. Beydaghyan, P. V. Ashirt, and J.-F. Bisson, "Compact linearly polarized ceramic laser made with anisotropic nanostructured thin films", *Applied Optics*, vol. 54, pp. 8326–8331, 2015.

[185] A. Doucet, G. Beydaghyan, P. V. Ashirt, and J.-F. Bisson, "Linearly Polarizing Laser Mirror for Q-switched Operation", *Optical Interference Coatings 2016*, 2016.

[186] F. Li et al., "A chiral microchip laser using anisotropic grating mirrors for single mode emission", *Nanophotonics*, vol. 12, pp. 1741–1752, 2023.

[187] S. Longhi, "Airy beams from a microchip laser", *Opt. Lett.*, vol. 36, pp. 716–718, 2011.

[188] S. Liu et al., "Effect of thermal lens on beam quality and mode matching in LD pumped Er–Yb-codoped phosphate glass microchip laser", *Journal Of Physucs D: Applied Physics*, vol. 41, no. 035104, 2008.

[189] M. Tsunekane and T. Taira, "300 W continuous-wave operation of a diode edge-pumped, hybrid composite Yb:YAG microchip laser", *Optics Letters*, vol. 31, no. 13, 2006.

[190] M. Abramowitz and I. A. Stegun, *Handbook of Mathematical Functions with Formulas, Graphs, and Mathematical Tables*. National Bureau of Standards, 1972.

[191] I. Lukosiunas, L. Grineviciute, J. Nikitina, D. Gailevicius, and K. Staliunas, "Extremely narrow sharply peaked resonances at

the edge of the continuum", *Phys. Rev. A*, vol. 107, p. L061501, 2023.

[192] L. Grineviciute, "Nanostructured optical coatings for the manipulation of laser radiation", PhD thesis, Vilnius University, Vilnius, Lithuania, 2021.

[193] ISO, *Lasers and Laser- Related Equipment: Test methods for laser beam widths, divergence angles and beam propagation ratios, ISO 11146-1:2021 (International Standards Organization, Geneva).* 2021.

[194] L. Lugiato, G. Oppo, J. Tredicce, L. Narducci, and M. Pernigo, "Instabilities and spatial complexity in a laser", *Journal of the Optical Society of America B*, vol. 7, no. 6, pp. 1019–1033, 1990.

[195] I. Shoji, Y. Sato, S. Kurimura, V. Lupei, and T. Taira, "Thermal-birefringence-induced depolarization in Nd:YAG ceramics", *Optics Letters*, vol. 27, pp. 234–236, 2002.

[196] P. Shukla, J. Lawrence, and Y. Zhang, "Understanding laser beam brightness: A review and new prospective in material processing", *Optics Laser Technology*, vol. 75, pp. 40–51, 2015.

[197] G. Grimmett and D. Stirzaker, *Probability and random processes.* Oxford university press, 2020.

[198] P. R. Bevington and D. K. Robinson, *Data reduction and error analysis for the physical sciences.* McGraw Hill, New York, 2003.

[199] D. Findlay and R. Clay, "The measurement of internal losses in 4-level lasers", *Physics Letters*, vol. 20, no. 3, pp. 277–278, 1966.

[200] D. Meschede, *Optics, Light and Lasers.* WILEY-VCH Verlag GmbH Co. KGaA, 2007.

[201] W. R. Inc., *Mathematica, Version 9.0.* [Online]. Available: `https://www.wolfram.com/mathematica`.

[202] A. E. Siegman, "Defining the Effective Radius of Curvature for a Nonideal Optical Beam", *Journal of Quantum Electronics*, vol. 27, pp. 1146–1148, 1991.

[203] A. E. Siegman, "New developments in laser resonators", in *Optical Resonators*, D. A. Holmes, Ed., International Society for Optics and Photonics, vol. 1224, SPIE, 1990, pp. 2–14.

[204] T.-C. Poon and T. Kim, *Egnineering optics with Matlab*. World Scientific Publishing Co. Pte. Ltd, 2006.

[205] Wolfram Research, Inc., *NIntegrate: Get a numerical approximation to an integral*, Wolfram Language & System Documentation Center, Wolfram Research, Inc., Champaign, Illinois, USA, 2025. [Online]. Available: `https://reference.wolfram.com/language/ref/NIntegrate.html`.

Santrauka

Disertacijos tikslas

Išplėsti mikrolustinių lazerių išorinių parametrų galimybes ir taikymo sritis, integruojant pažangius fotoninių kristalų dizainus į mikrolustinio lazerio rezonatorių. Šio metodo tikslas – pagerinti pagrindinius išvadinius parametrus, įskaitant šviesį, pluošto kokybės faktorių (M^2) ir poliarizacinį kontrastą. Taip pat, sukurti praktinį teorinį modelį, skirtą išvadinio pluošto kokybės faktoriui (M^2) įvertinti ir jo modalinei sudėčiai analizuoti.

Disertacijos mokslinės užduotys

1. Eksperimentiškai pademonstruoti, kad padidėja mikrolustinio lazerio išvadinio pluošto erdvinė kokybė ir šviesis, į lazerio rezonatorių įterpiant fotoninį kristalą.

2. Eksperimentiškai pademonstruoti poliarizacinio kontrasto padidinimą mikrolustiniame lazeryje, integruojant fotoninį kristalą lazerio rezonatoriuje.

3. Sukurti praktinį teorinį modelį, skirtą mikrolustinių lazerių pluošto kokybės faktoriui (M^2) ir modalinei sudėčiai įvertinti, ir patvirtinti modelį eksperimentiniais matavimais.

Mokslinis naujumas ir praktinė nauda

Šioje disertacijoje pristatomas nauja mikrolustinio lazerio rezonatoriaus su fotoniniais kristalais koncepcija, kuri pagerina lazerio pluošto erdvines ir poliarizacines savybes. Šis patobulinimas gali būti tiesiogiai panaudotas mikrolustiniuose lazeriuose, kurie naudojami labai svarbiose srityse, tokiose kaip karyba, medicina, pramoninis medžiagų apdirbimas, kosmosas ir kt. Naujas lazerio dizainas pasižymi nauja fizikine dinamika, kuri tiriama eksperimentiškai ir teoriškai šioje disertacijoje. Mokslinį naujumą ir praktinę vertę galima apibendrinti šiais teiginiais:

- Pirmą kartą eksperimentiškai ištirtas mikrolustinis lazeris su erdviškai filtruojančiu fotoniniu kristalu, kuris pakeičia išvadinį rezonatoriaus veidrodį. Tokiu būdu pagerinama lazerio pluošto erdvinė kokybė ir šviesis.

- Pirmą kartą eksperimentiškai ištirtas mikrolustinis lazeris su fotoniniu kristalu, veikiančiu kaip išvadinis veidrodis ir filtruojančiu poliarizaciją esant didelei kaupinimo galiai. Tokiu būdu pagerinamas poliarizacinis kontrastas, pluošto erdvinė kokybė ir šviesis, lyginant su poliarizacijos filtravimo technika, naudojant tiesiškai poliarizuotą kaupinimo spinduliuotę.

- Sukurtas naujas teorinis praktinis metodas, skirtas įvertinti mikrolustinio lazerio erdvinės pluošto kokybės faktorių M^2 ir modalinį turinį.

Ginamieji teiginiai

1. Teigiu, kad įprastą izotropinį išvadinį veidrodį pakeitus kampinio filtravimo veidrodžiu (AFM) 2,1 mm ilgio Nd:YAG mikrolustinio lazerio rezonatoriuje, veikiančiame nuolatinės bangos (CW) režimu, pagerėja pluošto kokybė ir šviesis tirtame 1,5–11,7 W kaupinimo galios intervale. Šie pokyčiai yra naudingi mikrolustiniame lazeryje.

2. Teigiu, kad įprastą izotropinį išvadinį veidrodį pakeitus poliarizuojančiu meta-veidrodžiu (MM) 5 mm ilgio Nd:YAG mikrolustinio lazerio rezonatoriuje, veikiančiame CW režimu, padidėja poliarizacijos kontrastas tirtame 1–3,5 W sugertos kaupinimo galios intervale. Šie pokyčiai yra naudingi mikrolustiniame lazeryje.

3. Teigiu, kad sukurtas dvimatis tiesinio lauko modelis leidžia kiekybiškai prognozuoti pluošto kokybės faktorių M^2 eksperimentiškai tirtuose Nd:YAG mikrolustiniuose lazeriuose su 5 mm ir 15 mm ilgio rezonatoriais, veikiančiais CW režimu. Tai patvirtina teorijos ir eksperimento atitikimas.

Skersinės modos ir pluošto kokybės faktorius M^2 mikrolustiniame lazeryje

Šiame skyriuje nagrinėjamas skersinių modų susidarymas mikrolustiniuose lazeriuose (McL). Analizuojama lazerinio pluošto kokybės faktoriaus M^2 priklausomybė nuo kaupinimo galios išilgai kaupinamame rezonatoriuje su dviem plokščiais veidrodžiais. Skersinės modos susiformuoja dėl kaupinimo ir terminio lęšio įtakos.

Skersinių modų analizei naudojama dvimatė tiesinė elektrinio lauko lygtis:

$$\frac{\partial A}{\partial t} = -\rho A + id\nabla A + i\sigma(r)A + \gamma(r)A, \tag{4.114}$$

kuri paremta vidutinio lauko (mean-field) aproksimacija. Lygtyje figuruoja stiprinimo $\gamma(r)$ ir lūžio rodiklio $\sigma(r)$ pasiskirstymo funkcijos, pasižyminčios ašine simetrija. Modelyje taip pat figuruoja difrakcijos koeficientas d ir rezonatoriaus nuostoliai ρ. Darant prielaidą, kad stiprinimo ir lūžio rodiklio skirstiniai yra cilindrinės simetrijos ir vienodo diametro, tolesnis nagrinėjimas tampa tikrinių verčių sprendinių suradimu.

Stiprinimo ir lūžio rodiklio pasiskirstymo funkcijos aproksimuojamos

cilindrinės simetrijos funkcijomis:

$$\sigma(r) = \begin{cases} S_0 & \text{if } r < R; \\ 0 & \text{if } r > R; \end{cases}, \ \gamma(r) = \begin{cases} G_0 & \text{if } r < R; \\ 0 & \text{if } r > R. \end{cases} \tag{4.115a,b}$$

Toks supaprastinimas leidžia gauti pusiau analitinius sprendinius. Skersinių modų tikrinių verčių nustatymo uždavinys tampa matematiškai analogiškas Šrėdingerio lygties atvejui, tačiau, skirtingai nei klasikiniame variante, potencialo barjeras čia yra kompleksinis.

Šį barjerą aprašo kompleksinis parametras

$$\zeta^2 = R^2 \frac{iS_0 + G_0}{id}, \tag{4.116}$$

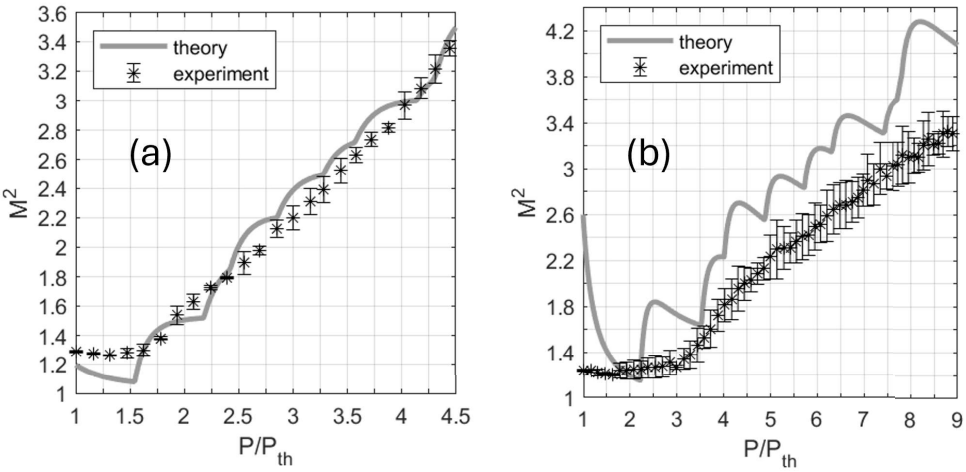
kuris priklauso nuo stiprinimo koeficiento ir lūžio rodiklio moduliacijos amplitudžių (S_0, G_0). Abu šie dydžiai yra tiesiogiai susiję su sugerta kaupinimo galia, todėl kaupinimo galia tampa fiziniu parametru, lemiančiu skersinių modų atsiradimą ir pluošto kokybės faktoriaus M^2 kitimą.

Sprendžiant tikrinių verčių uždavinį, surandamas kiekvienos modos stiprinimo koeficientas nesant įsotinimo. Kiekvieną modą atitinka kompleksinis skaičius λ_{lm}, kurio realioji dalis $(\lambda_{re})_{lm}$ nusako modos stiprinimą ir generacijos slenkstį, o menamoji dalis $(\lambda_{im})_{lm}$ – dažnio poslinkį. Skaičiavimai rodo, kad didėjant kaupinimo galiai, modos atsiranda nuosekliai viena po kitos: pirmiausia fundamentinė moda, vėliau – aukštesnės eilės modos.

Fokusuojantis (teigiamas) šiluminis lęšis sumažina modų generacijos slenkstį, tuo tarpu sklaidantis (neigiamas) šiluminis lęšis slenkstį padidina.

Apskaičiuotos skersinių modų analitinės funkcijos ir kiekvienos modos pluošto kokybės faktoriai M^2. Esant mažoms kaupinimo galioms, fundamentinės modos diametras yra didesnis ir moda pasižymi didesniu M^2. Didėjant kaupinimo galiai, modos diametras vis mažėja, o modos pluošto kokybė gerėja. Aukštesnės eilės modos pasižymi analogiška dinamika.

Siekiant aprašyti realiomis sąlygomis stebimą daugiamodį rėžimą, pasiūlytas supaprastintas pluošto kokybės faktoriaus M^2 įvertinimo modelis.



4.20 pav.: Pluošto kokybės faktoriaus M^2 priklausomybė nuo į slenkstį normuotos kaupinimo galios P/P_{th}, kai rezonatoriaus ilgis yra $L = 5mm$ (a) ir $L = 15mm$ (b). Pilkos vientisos kreivės vaizduoja teoriškai įvertintas M^2 reikšmes, o juodos žvaigždutės su paklaidų juostomis – eksperimentiškai išmatuotas vertes.

Daroma prielaida, kad mikrolustinis lazeris veikia kaip B klasės lazeris, kuriame režimų tarpusavio konkurencija yra silpna. Tokiu atveju pluošto M^2 gali būti įvertintas kaip atskirų modų M^2_{lm} vidurkis, kiekvienos modos svorį parenkant pagal pagal modos stiprinimo koeficientą $(\lambda_{re})_{lm}$:

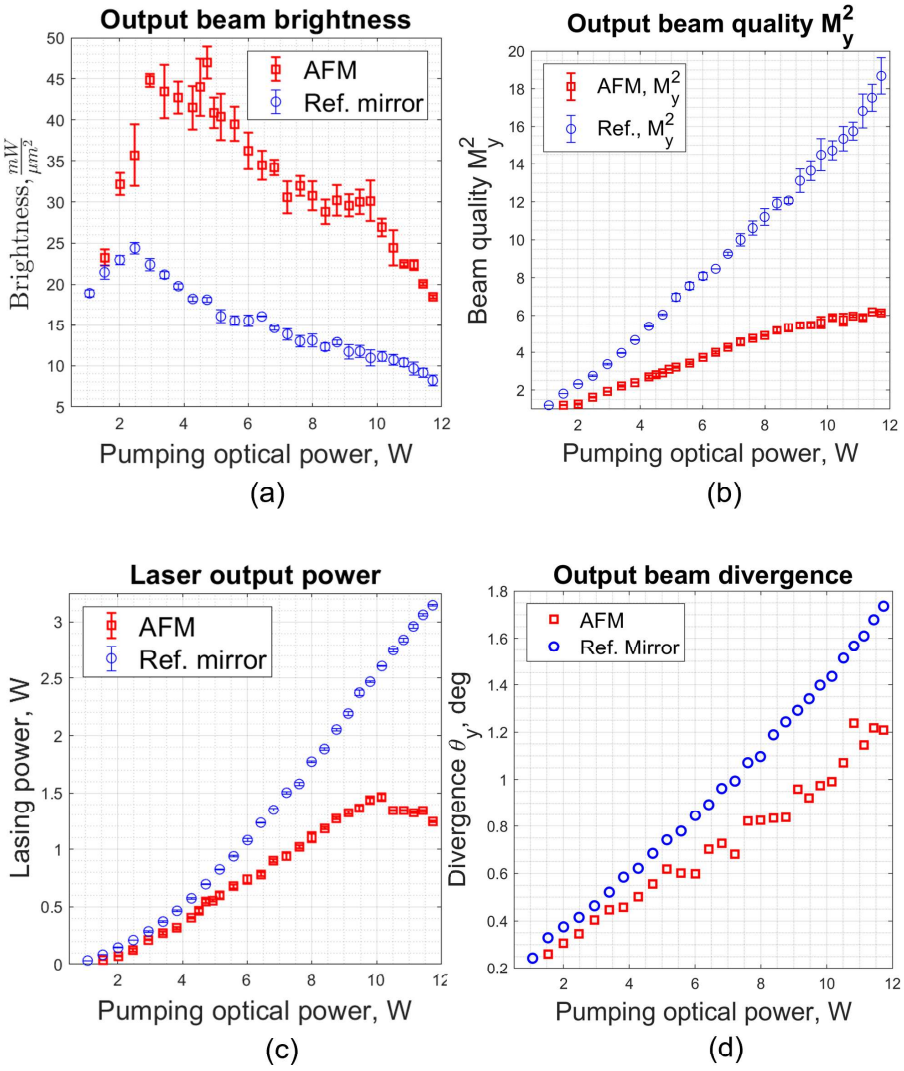
$$M^2 = \frac{\sum_{l,m}^{\infty} M^2_{lm} \, (\lambda_{re})_{lm}}{\sum_{l,m}^{\infty} (\lambda_{re})_{lm}}. \tag{4.117}$$

Teoriniai rezultatai palyginti su eksperimentiniais matavimais, atliktais Nd:YAG mikrolustiniuose lazeriuose su skirtingo ilgio rezonatoriais (pav. 4.20). Teoriniai ir eksperimentiniai rezultatai gerai atitinka, ypač trumpame rezonatoriuje. Ilgesnių rezonatorių atveju stebimi nuokrypiai, siejami su vidutinio lauko (mean-field) aproksimacija, kuri buvo panaudota modelyje. Parodyta, kad pasiūlytas metodas leidžia apytiksliai įvertinti pluošto kokybės faktoriaus M^2 kitimą priklausomai nuo kaupinimo galios.

Apibendrinant, šiame skyriuje pateikta nuosekli teorinė ir eksperimentinė skersinių modų analizė mikrolustinių lazerių atveju bei pasiūlytas praktiškai taikomas metodas pluošto kokybės faktoriui M^2 įvertinti.

Erdvinis filtravimas fotoninių kristalų mikrolustiniame lazeryje

Mikrolustiniai lazeriai yra kompaktiški ir plačiai taikomi koherentinės spinduliuotės šaltiniai. Tačiau jų praktinį pritaikymą, ypač esant didesnėms kaupinimo galioms, riboja spinduliuotės erdvinė kokybė ir šviesis. Didėjant kaupinimo galiai, rezonatoriuje sužadinamos aukštesnės eilės skersinės modos, dėl kurių auga pluošto kokybės faktorius M^2 ir mažėja spinduliuotės šviesis.



4.21 pav.: Eksperimentiškai išmatuotos lazerio spinduliuotės šviesio (a), pluošto kokybės faktoriaus (b), išėjimo galios (c) ir divergencijos (d) priklausomybės nuo kaupinimo galios, kai naudojamas AFM ir etaloninis veidrodis.

Šiame darbe pasiūlytas ir eksperimentiškai realizuotas metodas, lei-

džiantis sumažinti mikrolustinio lazerio pluošto kokybės faktorių M^2 ir padidinti spinduliuotės šviesį, vieną iš plokščių rezonatoriaus veidrodžių pakeičiant kampinio filtravimo veidrodžiu (angl. *Angular Filtering Mirror*, AFM). AFM atspindžio koeficientas yra itin jautrus mažiems kritimo kampo pokyčiams, todėl veidrodis selektyviai atspindi mažo kampo erdvinius dažnius, o didesnio kampo komponentės rezonatoriuje patiria padidintus nuostolius.

Kampinis filtravimas leidžia efektyviai slopinti aukštesnės eilės skersines modas ir sudaro palankesnes sąlygas žemesnės eilės modų generacijai, neįvedant papildomų elementų į rezonatorių. Skirtingai nei tradiciniai erdvinio filtravimo metodai, AFM veikia atspindžio režimu erdvinių dažnių srityje. Dėl itin mažo, kelių mikrometrų siekiančio storio AFM yra ypač tinkamas itin kompaktiškoms lazerinėms sistemoms. Be to, ši technologija yra perspektyvi masinei gamybai, nes struktūros gali būti formuojamos ant didelio ploto padėklų ir vėliau supjaustomos į mažesnes dalis.

Eksperimentiniuose tyrimuose buvo naudotas 2 mm ilgio Nd:YAG mikrolustinis lazeris, išilgai kaupinamas 808 nm daugiamodžiu diodiniu lazeriu. Kampinio filtravimo veidrodis (AFM) buvo naudojamas kaip išėjimo veidrodis. Rezultatai buvo lyginami su įprastu dielektriniu veidrodžiu, kurio atspindžio koeficientas esant nuliniam kritimo kampui buvo artimas AFM atspindžiui. Tyrimų metu buvo išmatuota lazerio išėjimo galia, pluošto kokybės faktorius M^2 ir sklidimo kampas, taip pat apskaičiuotas spinduliuotės šviesis.

Gauti rezultatai (pav. 4.21) parodė, kad naudojant AFM pasiekiamas reikšmingas spinduliuotės erdvinės kokybės pagerėjimas vienoje skersinėje kryptyje. Nors dėl papildomų nuostolių lazerio išėjimo galia sumažėja, bendras spinduliuotės šviesis padidėja maždaug du kartus, palyginti su lazeriu, naudojančiu įprastą išėjimo veidrodį. Didžiausias šviesis pasiekiamas esant vidutinėms kaupinimo galioms, kur kompromisas tarp galios ir pluošto kokybės yra optimalus.

Eksperimentiniai stebėjimai buvo pagrįsti skaitmeniniais modeliavimais, atliktais integruojant Maksvelo–Blocho lygčių sistemą B klasės

mikrolustiniam lazeriui. Modelyje kampinis filtravimas buvo įtrauktas fenomenologiškai, atsižvelgiant į eksperimentiškai išmatuotą AFM kampinę perdavimo charakteristiką. Skaitmeniniai rezultatai kokybiškai sutapo su eksperimentiniais duomenimis, parodydami M^2 sumažėjimą, išėjimo galios kritimą ir šviesio padidėjimą, naudojant AFM.

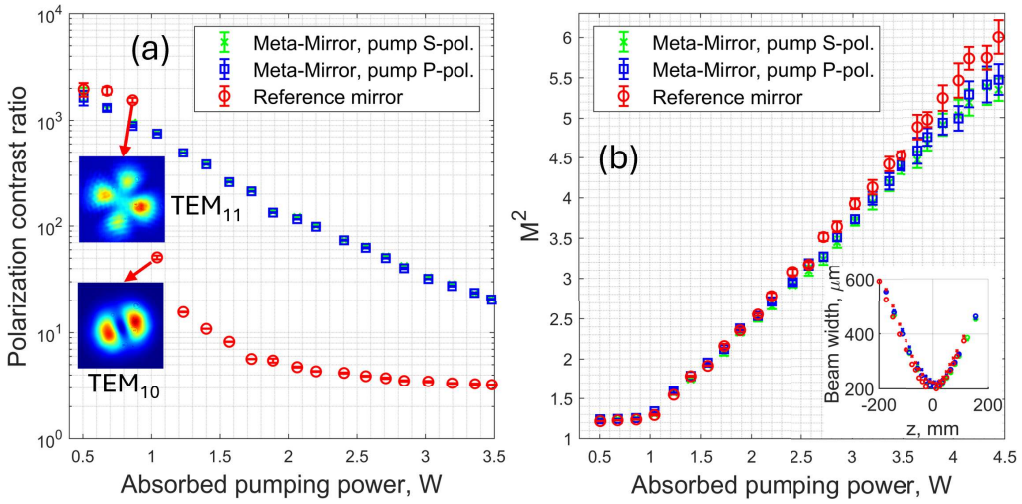
Apibendrinant galima teigti, kad kampinio filtravimo veidrodis yra efektyvus sprendimas mikrolustinių lazerių spinduliuotės erdvinei kokybei ir šviesiui gerinti. Pasiūlytas metodas yra tinkamas itin kompaktiškoms lazerinėms sistemoms. Be to, dvimatės kampinio filtravimo struktūros ateityje gali suteikti galimybę pasiekti dar didesnį šviesio padidinimą, viršijant šiame darbe demonstruotą dvigubą padidėjimą.

Poliarizacinis filtravimas fotoninių kristalų mikrolustiniame lazeryje

Šiame darbe pristatytas inovatyvus poliarizuojantis meta-veidrodis (angl. *Meta-Mirror*) ir jo pritaikymas Nd:YAG mikrolustiniame lazeryje, siekiant padidinti išvadinės lazerio spinduliuotės poliarizacinį kontrastą. Kartu su meta-veidrodžiu buvo panaudotas poliarizuotas kaupinimas, o jų pavienis ir kombinuotas poveikis buvo sistemiškai ištirtas skirtinguose kaupinimo galios režimuose. Tokia analizė leido atskirti meta-veidrodžio ir poliarizuoto kaupinimo indėlį į poliarizacijos kontrasto didėjimą bei nustatyti ribinę kaupinimo galią, nuo kurios vien poliarizuotas kaupinimas tampa neefektyvus.

Nd:YAG kristalas pasižymi silpnu dvejopalūžiškumu, atsirandančiu dėl mechaninio poveikio. Dėl skirtingų optinių kelių susidaro dvi išilginių modų grupės, kurių poliarizacijos kryptys yra tarpusavyje ortogonalios. Nd:YAG stiprinimas yra anizotropinis ir priklauso nuo kaupinimo spinduliuotės poliarizacijos krypties. Kai kaupinimo poliarizacija sutampa su viena iš išilginių modų poliarizacijos krypčių, šiai išilginei modai sudaromos palankesnės stiprinimo sąlygos, todėl lazerio generacija tampa tiesiškai poliarizuota. Tačiau didėjant kaupinimo galiai, aktyviojoje terpėje stiprėjantys šiluminiai efektai lemia depoliarizacijos augimą.

Meta-veidrodis veikia kaip poliarizuojantis išėjimo veidrodis ir pasižymi itin didele atspindžio asimetrija skirtingoms poliarizacijoms: S-poliarizuota spinduliuotė yra stipriai atspindima, o ortogonali P-poliarizacija – gerokai silpniau. Pasiektas atspindžių skirtumas $\Delta R \approx 85\%$ reikšmingai viršija anksčiau literatūroje demonstruotas vertes rezonansinėse gardelėse. Svarbu pabrėžti, kad meta-veidrodis neįneša papildomų sugerties nuostolių ir pasižymi silpna atspindžio priklausomybe nuo kritimo kampo.



4.22 pav.: Poliarizacijos kontrasto (a) ir pluošto kokybės faktoriaus M^2 (b) priklausomybės nuo sugertos kaupinimo galios P_{abs}. Kaupinimo poliarizacijos kryptis sutampa su meta-veidrodžio S- arba P-poliarizacijomis. Isotropiniam veidrodžiui kaupinimo poliarizacija buvo optimizuota maksimaliam poliarizacijos kontrastui pasiekti.

Eksperimentiniai tyrimai buvo atlikti naudojant 2 mm ilgio Nd:YAG mikrolustinį lazerį, išilgai kaupinamą 808 nm daugiamodžiu diodiniu lazeriu. Buvo tirta lazerio poliarizacijos kontrasto, išėjimo galios, pluošto kokybės faktoriaus M^2 ir spinduliuotės šviesio priklausomybė nuo sugertos kaupinimo galios. Palyginti trys kraštiniai atvejai: meta-veidrodis su S-poliarizuotu kaupinimu, meta-veidrodis su P-poliarizuotu kaupinimu ir įprastas izotropinis išėjimo veidrodis su optimizuotu poliarizuotu kaupinimu.

Rezultatai (pav. 4.22) parodė, kad tiek poliarizuotas kaupinimas, tiek meta-veidrodis, veikdami atskirai leidžia pasiekti didelį poliarizacinį kontrasto santykį (> 1000) tik iki maždaug 1 W sugertos kaupinimo

galios. Viršijus šią ribą, izotropinio veidrodžio atveju stebimas staigus poliarizacijos kontrasto kritimas, susijęs su depoliarizuotos skersinės modos sužadinimu. Priešingai, meta-veidrodis leidžia išlaikyti didelį poliarizacijos kontrastą ir virš šios ribos, nors didėjant galiai jis palaipsniui mažėja. Nustatyta aiški kaupinimo galios riba, nuo kurios meta-veidrodis tampa dominuojančiu ir praktiškai vieninteliu efektyviu poliarizacijos stabilizavimo faktorium.

Be poliarizacijos kontrasto didinimo, meta-veidrodžio naudojimas taip pat lemia nedidelį, bet nuoseklų pluošto kokybės faktoriaus M^2, išėjimo galios ir spinduliuotės šviesio pagerėjimą. Didžiausias šviesis pasiekiamas tada, kai kaupinimo poliarizacijos kryptis sutampa su meta-veidrodžio palaikoma S-poliarizacija. Be to, meta-veidrodžio konfigūracija pasižymi žymiai mažesniu jautrumu kaupinimo poliarizacijos krypčiai nei tradicinė sistema su izotropiniu veidrodžiu, kur poliarizacijos kontrastas priklauso nuo mechaninių įtempimų ir šiluminių reiškinių kristale.

Apibendrinant galima teigti, kad poliarizuojantis meta-veidrodis yra efektyvus sprendimas mikrolustinių lazerių poliarizacijos kontrastui didinti, ypač didelių kaupinimo galių režimuose. Skirtingai nei poliarizuotas kaupinimas, šis metodas nereikalauja papildomų optinių elementų ir leidžia naudoti nepoliarizuotus daugiamodžius kaupinimo šaltinius. Darbe identifikuota ribinė kaupinimo galia, nuo kurios poliarizuotas kaupinimas tampa nebeefektyvus.

Aprobacija

Mokslinės publikacijos tiesiogiai susijusios su disertacijos tema:

1. **Matas Plukys**, Eugenijus Gaizauskas, Darius Gailevicius, and Kestutis Staliunas, "Transverse modes and beam spatial quality in microchip lasers," *Physical Review A*, vol.107, p. 043505, 2023, https://link.aps.org/doi/10.1103/PhysRevA.107.043505

2. **Matas Plukys**, Lina Grineviciute, Julianija Nikitina, Darius Gailevicius, and Kestutis Staliunas, "Enhancement of brightness in

microchip laser with angular filtering mirrors," *Optics & Laser Technology*, vol.181, Part C, p. 111904, 2025,

https://doi.org/10.1016/j.optlastec.2024.111904

3. **Matas Plukys**, Lina Grineviciute, Julianija Nikitina, Darius Gailevicius, and Kestutis Staliunas, "Polarization enhancement in Nd:YAG microchip laser with Meta-Mirror output coupler," *Optics Letters*, vol. 50, p. 4666-4669, 2025,

   https://doi.org/10.1364/OL.566958,

   Publication has been highlighted as an Editor's Pick.

Pranešimai konferencijose:

1. **Matas Plukys**, Darius Gailevicius, Lina Grineviciute, Julianija Nikitina, and Kestutis Staliunas, *"Fano-structure as output coupling mirror of microchip laser doubles its brightness,"* SPIE Photonics Europe, Strasbourg, France, 2024 (žodinis),

   https://doi.org/10.1117/12.3016701

2. **Matas Plukys**, Eugenijus Gaizauskas, Darius Gailevicius, and Kestutis Staliunas, *"Modes in microchip lasers,"* SPIE Photonics Europe, Strasbourg, France, 2022 (žodinis),

   https://doi.org/10.1117/12.2621111

3. **Matas Plukys**, Eugenijus Gaizauskas, Darius Gailevicius, and Kestutis Staliunas, *"Modos mikrolustiniame lazeryje,"* Nacionalinė fizikos konferencija, Vilnius, Lietuva, 2021 (žodinis)

4. **Matas Plukys**, Eugenijus Gaizauskas, Darius Gailevicius, and Kestutis Staliunas, *"Transverse Modes and Beam Spatial Quality in Microchip Lasers,"* Humboldt Kolleg on Synthetic Quantum Matter, Vilnius, Lithuania, 2023 (stendinis)

Pagrindiniai rezultatai

Šios disertacijos pasiekti rezultatai:

1. Šiame darbe buvo suprojektuotas ir pagamintas plonasluoksnis kampinio filtravimo veidrodis (AFM), kurio atspindys yra labai jautrus kritimo kampui. Šis veidrodis buvo panaudotas mikrolustinio lazerio rezonatoriuje kaip išvadinis veidrodis.

   (a) **Eksperimentiškai pademonstruotas pluošto kokybės faktoriaus M^2 pagerėjimas, lyginant su įprastu plokščiu išėjimo veidrodžiu.**

   (b) **Eksperimentiškai pademonstruotas maždaug du kartus padidėjęs šviesis (brightness), lyginant su įprastu plokščiu išėjimo veidrodžiu.**

   (c) **Skaitmeniniai modeliavimai vienos išilginės modos aproksimacijoje patvirtino eksperimentinius rezultatus ir parodė, kad dvimatis kampinis filtravimas nėra apribotas dvigubu šviesio padidėjimu ir gali jį padidinti dar labiau.**

2. Šiame darbe buvo suprojektuotas ir pagamintas poliarizuojantis meta-veidrodis. Meta-veidrodis buvo panaudotas Nd:YAG mikrolustinio lazerio rezonatoriuje kaip išvadinis veidrodis, lazerį kaupinant poliarizuota spinduliuote.

   (a) **Eksperimentiškai pademonstruota, kad poliarizacinio kontrasto santykis viršija 1000, kai sugerta kaupinimo galia kristale yra mažesnė nei 1 W.**

   (b) **Viršijus šią ribą, aukštą poliarizacinį kontrastą užtikrino tik meta-veidrodžio konfigūracija, o taikant vien poliarizuotą kaupinimą kontrastas reikšmingai sumažėjo.**

   (c) **Meta-veidrodžio konfigūracija pasižymėjo ženkliai mažesniu jautrumu kaupinimo poliarizacijos krypties**

pokyčiams, palyginti su įprastu izotropiniu išėjimo veidrodžiu.

(d) **Lazerinio pluošto poliarizacijos kryptį tiesiogiai nulėmė meta-veidrodžio orientacija.**

(e) **Naudojant meta-veidrodį, eksperimentiškai nustatytas nedidelis pluošto kokybės faktoriaus M^2, išėjimo galios ir bendro šviesumo pagerėjimas.**

3. Sukurtas teorinis modelis, orientuotas į praktinį pritaikymą ir paremtas dvimate tiesine lygtim, leidžiančia aprašyti skersines modas ir įvertinti pluošto kokybės faktorių M^2 mikrolustiniuose lazeriuose, kai stiprinimo ir lūžio rodiklio pasiskirstymai yra aproksimuojami cilindro forma.

(a) **Apskaičiuota skersinių modų struktūra ir atitinkamos tikrinės vertės, kai stiprinimo ir termiškai indukuoto lūžio rodiklio pasiskirstymai yra aproksimuojami cilindro forma.**

(b) **Suformuluotas ir išspręstas skersinių modų tikrinių verčių uždavinys, analogiškas Šrėdingerio tipo lygčiai, tačiau su kompleksiniu potencialu.**

(c) **Pluošto kokybės faktorius M^2 įvertintas tiesiogiai iš apskaičiuotų elektrinio lauko pasiskirstymų.**

(d) **Teoriškai apskaičiuotos M^2 reikšmės patvirtintos eksperimentiškai.**

Išvados

1. Kampinis filtravimas atspindžio būdu, naudojant kampinio filtravimo veidrodį (AFM) mikrolustinio lazerio rezonatoriuje, yra efektyvus būdas gerinti lazerio spinduliuotės erdvinę kokybę.

(a) **Šviesio padidėjimas pasiekiamas naudojant itin ploną (šimtų nanometrų storio) struktūrą, todėl ji gali būti**

taikoma ypač trumpuose lazerio rezonatoriuose.

(b) **AFM nesukelia papildomų sugerties nuostolių, ką patvirtina nepakitusi generacijos slenkstinė galia.**

(c) **AFM realizuoja erdvinį filtravimą kampinėje srityje, todėl nesukelia difrakcinių nuostolių, galinčių atsirasti dėl ribotos apertūros.**

(d) **Dvimatis kampinis filtravimas leistų dar labiau padidinti šviesį.**

2. Poliarizacinis filtravimas atspindžio būdu, naudojant poliarizuojantį meta-veidrodį, yra efektyvus metodas Nd:YAG pagrindu veikiančio mikrolustinio lazerio poliarizacinėms savybėms gerinti:

(a) **Meta-veidrodis nesukelia papildomų sugerties nuostolių, ką patvirtina nepakitusi generacijos slenkstinė galia.**

(b) **Poliarizacijos filtravimas, realizuotas meta-veidrodžiu, yra nejautrus kaupinimo poliarizacijos krypčiai, todėl toks lazeris gali būti efektyviai kaupinamas daugiamodžiais, nepoliarizuotais šaltiniais.**

(c) **Vien poliarizuotas kaupinimas nėra pakankamas išlaikyti aukštą poliarizacinį kontrastą esant aukštesnėms kaupinimo galioms, tuo tarpu meta-veidrodis užtikrina aukštą poliarizacinį kontrastą.**

(d) **Meta-veidrodis ženkliai sumažina jautrumą kaupinimo poliarizacijos krypties pokyčiams.**

(e) **Poliarizacijos filtravimas atspindžio būdu nedaro neigiamo poveikio erdviniams pluošto parametrams ir netgi lemia jų pagerėjimą.**

3. Sukurtas teorinis modelis leidžia patikimai įvertinti pluošto kokybės faktorių M^2 praktiškai realizuotuose mikrolustiniuose lazeriuose.

(a) **Skersinių modų uždavinys mikrolustiniuose lazeriuose gali būti sprendžiamas taikant aproksimaciją, paremtą pusiau analitinu metodu.**

(b) **Pluošto kokybės faktorius M^2 gali būti įvertintas susiejant teorinę modų analizę su eksperimentiškai išmatuojamais rezonatoriaus parametrais.**

(c) **Teorijos ir eksperimento atitikimas patvirtina modelio tinkamumą praktiniam pluošto kokybės vertinimui mikrolustiniuose lazeriuose.**

Cirriculum Vitae

Name:	Matas
Surname:	Plukys
Birth place:	Akmenė, Lithuania
Education:	
2015-2019	Master in Laser Physics and Optical Technologies
2007-2011	Bachalor in Telecummunication Physics and Electronics
Professional experience:	
2015-2016	Research and Development Engineer, "UAB Ekspla" company, Vilnius
2016-2018	Product Specialist, "UAB Diagnostinės Sistemos" company, Vilnius
2018-2023	Sales Engineer, "UAB Optogama" company, Vilnius
2023-2025	Senior Sales Engineer, "UAB Optogama" company, Vilnius
Scientific activity:	Coauthor of 3 scientific publications

Publication List

Scientific publications directly related to Dissertation subject:

1. **Matas Plukys**, Eugenijus Gaizauskas, Darius Gailevicius, and Kestutis Staliunas, "Transverse modes and beam spatial quality in microchip lasers," *Physical Review A*, vol.107, p. 043505, 2023,

   https://link.aps.org/doi/10.1103/PhysRevA.107.043505

2. **Matas Plukys**, Lina Grineviciute, Julianija Nikitina, Darius Gailevicius, and Kestutis Staliunas, "Enhancement of brightness in microchip laser with angular filtering mirrors," *Optics & Laser Technology*, vol.181, Part C, p. 111904, 2025,

   https://doi.org/10.1016/j.optlastec.2024.111904

3. **Matas Plukys**, Lina Grineviciute, Julianija Nikitina, Darius Gailevicius, and Kestutis Staliunas, “Polarization enhancement in Nd:YAG microchip laser with Meta-Mirror output coupler,” *Optics Letters*, vol. 50, pp. 4666–4669, 2025.
   https://doi.org/10.1364/OL.566958
   *(Selected as an **Editor’s Pick**)*

Vilniaus universiteto leidykla
Saulėtekio al. 9, III rūmai, LT–10222 Vilnius
El. p. info@leidykla.vu.lt, www.leidykla.vu.lt
bookshop.vu.lt, journals.vu.lt

Tiražas 15 egz.